5-5-2017 12:00 AM

Automotive Inductive Position Sensor

Lingmin Shao, *The University of Western Ontario*

Abstract

Inductive angular position sensors (IAPS) are widely used for high accuracy and low cost angular position sensing in harsh automotive environments, such as suspension height sensor and throttle body position sensor. These sensors ensure high resolution and long lifetime due to their contactless sensing mode and their simple structure. Furthermore, they are suitable for wider application areas. For instance, they can be miniaturized to fit into a compact packaging space, or be adopted to measure the relative angle of multiple rotating targets for the purposes of torque sensing.

In this work, a detailed SIMULINK model of an IAPS is first proposed in order to study and characterize the sensor performance. The model is validated by finite element analysis and circuit simulation, which provides a powerful design tool for sensor performance analysis. The sensor error introduced by geometry imperfection is thoroughly investigated for two-phase and three-phase configurations, and a corresponding correction method to improve the accuracy is proposed. A design optimization method based on the response surface methodology is also developed and used in the sensor development.

Three types of sensors are developed to demonstrate the inductive sensor technology. The first type is the miniaturized inductive sensor. To compensate for the weak signal strength and the reduced quality (Q) factor due to the scaling down effect, a resonant rotor is developed for this type of sensor. This sensor is fabricated by using the electrodeposition technique. The prototype shows an 8mm diameter sensor can function well at 1.5mm air gap. The second type is a steering torque sensor, which is designed to detect the relative torsional angle of a rotating torsional shaft. It demonstrates the mutual coupling of multiple inductive sensors. By selecting a proper layout and compensation algorithm, the torque sensor can achieve 0.1 degree accuracy. The third type is a passive inductive sensor, which is designed to reduce power consumption and electromagnetic emissions.

The realization and excellent performance of these three types of sensors have shown the robustness of the inductive sensor technology and its potential applications. The research conducted in this dissertation is expected to improve understanding of the performance

analysis of IAPS and provide useful guidelines for the design and performance optimization of inductive sensors.

Keyword

Acknowledgments

This thesis is the result of a chronicle academic journey full of challenges and excitement. I would like to thank my supervisor, Dr. Jun Yang, who gave me the opportunity to join the team and carry on an exciting research project and has closely followed my progression.

Professor Liying Jiang has been helpful tutors and a friendly guide over these past years. With her help, I understood how to shape a good research project.

My special thanks go to Mr. Larry Willemsen from KSR international, whose continuous support makes all this happen.

Through good and bad times, I could always count on the endless support and unconditional love from my wife Yan Xia and my extended family, who always encouraged me to work hard and never had a single doubt on my potential.

My colleagues Naibo Zhang, Xueguang Han, Eric Zhang, and Dongxin Zhang were very supportive throughout my research, to which I owe them tremendous gratitude.

Table of Contents

List of Tables

List of Figures

Chapter 1

1 Introduction

1.1 Automotive position sensor

A sensor is generally defined as an input device that provides a usable output in response to a specific physical measurand[1]. The measurand might be mechanical, electrical, magnetic, optical, chemical, acoustic, or a combination of any two or more of them [2], which affects the sensor in a certain way that causes a response represented by the sensor's output. The output of many modern sensors is typically an electrical signal, but alternatively, could be a motion, deformation, or other usable type of output. Some examples of sensors include a thermocouple pair, which converts a temperature difference into an electrical output; a pressure sensor, which converts a fluid pressure into the deformation of a diaphragm [3]; a linear variable differential transformer (LVDT), which converts a position into an electrical output; and etc.

Vehicle safety, fuel economy and comfort are benefited substantially from the increasing usage of sensor technology, which allows interaction between the external environment and the vehicle's electronic control unit (ECU). Another driving force behind the sensor market growth is the shift towards self-driving cars, which requires more intelligent data processing devices to make autonomous decisions. For each new generation of a car model, a growing number of sensors are incorporated into the design. Among those automotive sensors, position/displacement sensors are the most widely used devices. The application of position/displacement sensors continues to expand, and these sensors are becoming key components in every functional unit, ranging from headlight positioning to air conditioning, electronic stability control, and anti-lock braking systems, to name a few[4].

A position sensor measures the distance between a constant reference datum and the present location of the target. Conversely, a displacement sensor measures the distance between the present position of the target and the position recorded previously. In other words, position refers to an absolute measurement, while displacement is a relative measurement indicating only the changes in the measurand as they occur.

The application areas of automotive position sensors are mainly the powertrain, chassis and body systems [5]. Powertrain systems include the engine, transmission and all onboard diagnostics elements. Chassis systems include the suspension, braking, lightning, steering and stability systems. Body systems include the safety of occupants, comfort, information services, and in general the rest of systems aimed to fulfill the needs of the vehicle occupants [5, 6]. In the powertrain system, crankshaft and camshaft position sensors are used for the control of fuel injection and ignition timing, while the gear position sensor is applied in electronically controlled gear shifting to detect transmission gear position. In the antilock brake system (ABS) and the electronic stability program (ESP), wheel position sensor plays a major role in detecting wheel speed [7]. The position sensor is also a key element in "drive by wire" systems, active suspension, automatic headlight leveling, as well as in wiper, mirror and seat positioning. Another important application of position sensors is the detection of steering wheel position for autonomous driving systems. The main applications of automotive position sensors are summarized in table 1-1.

Table 1-1 Main Automotive Application of Position Sensors

Powertrain	Engine	Crankshaft Rotational Motion
		Cam Rotational Motion
		Exhaust Gas Recirculation (EGR)
		Throttle Angle Position
	Transmission	Gearshift position
		Input/ Output Shaft Speeds
		Transmission Oil Level
		Clutch Pedal Position
		Booster Cylinder Position
Chassis	Braking	Wheel Speed
		Pedal Angle
	Steering	Steering Wheel Angle for EPS
		Steering Torque (Torsion Angle) for EPS
	Vehicle	Suspension Height
		Sensor for Headlamp Leveling Control

		Wiper Position
		Mirror Position
Body	Safety	Seat Position
	Security	Vehicle Tile for Anti-Theft System

With the advent of vehicle electrification, electric motors are gradually replacing the conventional mechanical and hydraulic systems [8]. The motor position sensor is another major application of position sensors. In brushless DC motors, field orientation control (FOC) regulates the commutation of the three phase current based on the rotor position. Minimizing the motor torque ripples depends on a smooth phase current commutation, which further depends on accurate rotor position information. The motor position sensor is essentially a high-speed angular sensor that can operate above 400 rpm with better than 0.5° accuracy and better than 0.1° resolution. Optical encoders or inductive resolvers are typically used for this application. The less expensive magnetic and inductive sensing technologies are gradually adopted while still generally meeting the technical requirements with lower performance margin [9].

1.1.1   Automotive position sensor requirements

The automotive sensors must satisfy some requirements according to standards and regulations in automotive industries. The accuracy demanded is typically better than 1% over the entire measurement and temperature ranges. The temperature range is very wide, and the vibration experienced may be large. The environmental conditions are also very adverse with regards to electronic interference, humidity, liquids, dust and pollution[10]. Table 1-2 summarizes the typical automotive environments of position sensors based on OEM's technical specification. Moreover, due to the high-volume production and strong competition among companies, cost is also a major concern. As a result, automotive sensors must face a difficult tradeoff among accuracy, robustness, manufacturability, interchangeability, and low cost[6]. Those requirements guide us to reach an overall optimal sensor solution for the vehicle.

Table 1-2 Automotive Application Environment

Temperature:	*-40 °C to 150 °C*
Mechanical Shock:	*Up to 50 g*
Mechanical Vibration:	*Up to 15g*
Exposure to:	*Fuels, Brake Fluid Oil, Transmission Fluid, Salt Spray, Water, Dirt, Dust.*
EMI:	*200 Volts/Meter*
Life Cycle:	*18 years*

1.2   Automotive position sensor technology

Based on the sensing technology, position sensors are classified in six major categories in the automotive applications sector, including resistive contacting sensor, Hall effect sensor, anisotropic magnetoresistive (AMR) Sensor, Optical Encoder, Integrated Magnetic Concentrator (IMC) Hall-Effect Sensor, and Inductive Position Sensor (IPS).

1.2.1   Resistive contacting sensor

The resistive contacting sensor is also known as the potentiometric sensor, which consists of a conductor and a wiper. The working principle is to utilize the property that the resistance of a conductor varies linearly with its length. The conductor is usually a film or a screen-printed track. The wiper can be either linearly or angularly displaced by the part whose position is to be measured. The use of multiple and redundant wipers and tracks provides improved sensor reliability [5]. The resistive contacting sensor is the first position sensor introduced to automotive applications due to its simple design and low cost. However, it has been gradually replaced by non-contacting sensors due to wearing and reliability issues.

1.2.2 Hall effect sensor

In an appropriate magnetic circuit, Hall sensor voltage varies with the angle between the flux density acting on the sensor and the bias current applied to the sensor. Typically, two Hall sensing elements are mounted in quadrature. The two Hall elements provide output signals, with one varying as a sine wave and the other as a cosine wave. The output signal is derived from the inverse tangent of the ratio of the quadrature element signals. This provides a linear indication of the angular position of the excitation field of the magnet, thereby determining the angular position of the shaft [22]. Hall sensors are also used for linear position measurements, where magnet "head-on" and "slide-by" movements detect linear position [13].

1.2.3 Anisotropic Magnetoresistive (AMR) Sensor

The sensor exhibits changes of resistance as an external magnetic field rotates with respect to its sensing-elements. Two sets of four sensing elements are typically used. One set is physically offset from the other by a 45 degrees of angle. This angular offset again produces a quadrature 90 degree electrical phase angle difference. The two sets of sensing elements are connected in Wheatstone bridge signal-detection IC circuits. Both bridge circuits respond to the orientation of the external magnetic field and yield output signals. From these signals, the inverse tangent of their ratio gives a linear measurement of the angular position of the magnet target. The electrical angle goes through two cycles as the angular position of the magnet rotates one revolution. Further detailed information on AMR position sensors can be found in [23].

1.2.4 Optical Encoder

For a steering-wheel angle sensor application, a slotted-aperture optical-encoder sensor is combined with a gear-reduction-driven potentiometric sensor [24]. The potentiometric sensor provides a continuous measurement of the steering-wheel angle over a four-turn lock-to-lock turn range with less accuracy than the optical encoder. The encoder, with two offset bands of 90 aperture slots each, can measure within 1-degree accuracy, but it cannot determine the absolute position of the steering wheel. With the combination of these two sensors, the encoder "learns" the true center (or zero) absolute position of the steering

wheel by starting with the position indicated by the potentiometer and then refining the calibration based on a period of straight-road driving.

1.2.5   Integrated Magnetic Concentrator (IMC) Hall-Effect Sensor

This sensor measures angular position using a single bar magnet attached to the rotating part whose angle is to be determined. The sensor is mounted on a fixed surface underneath the magnet. The sensor combines standard planar Hall effect technology with a unique Integrated Magnetic Concentrator(IMC) consists of the following components as shown in Figure1-1, this is done by with a detailed description provided for each.
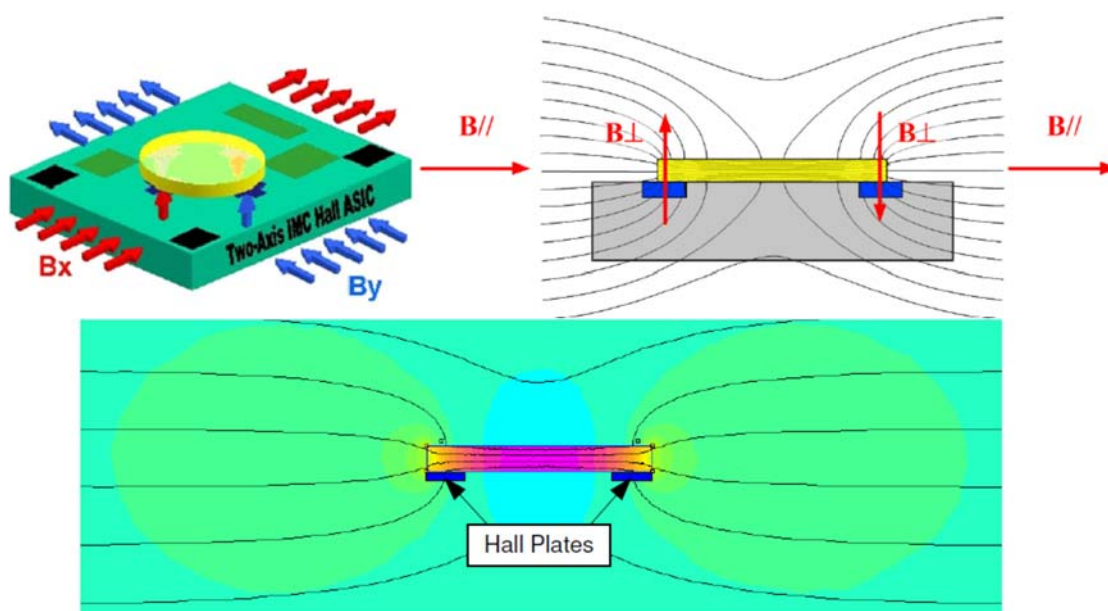
Figure 1-1 IMC Hall-Effect Sensor

a) A planar high-permeability ferromagnetic layer: IMC is a flat ferromagnetic part integrated on the surface of a magnetic sensor in a wafer post-processing step. The IMC changes the parallel field directions to perpendicular field directions as the result of a boundary condition transition between the air and the high-permeability IMC layer. The use of an IMC layer to redirect the magnetic field into a perpendicular direction largely eliminates direction variability [13], [14]. Meanwhile, the magnetic flux density "seen" by a Hall element placed near an edge of an IMC can be up to 10 times higher than the flux density far away from the IMC. The effective magnetic

resolution of a combination of IMC-Hall element can be 10 times higher than that of the Hall element alone.

b) Hall-effect sensing elements: Hall-effect sensing elements are mounted on the silicon substrate, in four quadrant positions, below the IMC layer. Hall sensing elements detect the X and Y components of the magnetic field. As the magnet target rotates, pairs of Hall-effect sensing elements detect and generate quadrature and signal voltage waveforms [14].

c) Embedded digital signal processors (DSPs): The signals are in phase quadrature and are processed to determine a resolved angle with the inverse tangent function. DSPs are embedded on the silicon substrate along with the Hall effect sensing elements. Dual-DSP isolated dies are used for redundancy to ensure reliability [15].

The IMC rotary position sensor provides the following features:

—Noncontact, easy-to-install, end-of-shaft mounting.

—Compact size, small outline package (excluding the magnet).

—Insensitivity to variations of magnetic field strength, temperature, and air gap.

—Absolute 360 degree angular position measurement.

1.2.6   Inductive Position Sensor

Inductive Position sensor measures angular position using a multi-lobed conductor coil on a rotor attached to parts like the throttle plate, accelerator pedal, or chassis-height link bar. The multi-lobed coil on the rotor is connected to the throttle plate and is suspended next to the receive coils which consist of three or more planar coils intertwined together. The receive coils are mounted on a fixed housing. A single-loop excitation coil, also mounted on the fixed housing, encircles the receive coils and provides ac-excitation. The excitation coil generates a MHz-frequency RF field. The excitation coil's RF field inductively couples (like a transformer) to circumferential portions of the rotor multi-lobed coil, and induces current in the rotor's conductor.

Current flowing in the radial portions of the rotor conductor lobes generates a secondary magnetic field pattern that rotates with the rotor and inductively couples to the underlying receiving coils. Each of the receiving coils couples with the rotor magnetic field and inductively generates its own (phase-shifted) voltage waveform as a function of the rotor angle. The angle of the measured part (e.g., a throttle plate) is determined via signal processing of the magnitudes, signs, and gradients of the individually phase-shifted receiving-coil voltages [11], [12].

Inductive position sensors offer the following features:

—Noncontact operation;

—No magnets are required;

—Low cost due to printed circuit board (PCB) structure;

—Allow relaxed assembly alignment tolerances;

—Design flexibility allows the sensor to be customized into various packaging space.

Due to their mature state of development and low cost, potentiometric sensors are extensively used to measure fuel-float level, accelerator pedal angle, and transmission gear position. Due to the harsh environment of the engine and the high number of lifetime dither cycles, noncontact Hall sensors are used to measure throttle angle, EGR valve position, and suspension height. AMR position sensors are used in the same applications as potentiometric and Hall sensors. Hall sensors are also used in seat belt buckles for high-reliability detection of proper buckle engagement i.e., proper linear positions of latch and tongue parts inside the buckle [26]. Since optical sensors are susceptible to contamination by dirt/oil, they are often used in applications that can provide environmentally protected mounting locations. A good example is the optical-encoder steering-wheel angle sensor used in vehicle stability enhancement systems, which is mounted on the steering column near the instrument panel. In active suspension systems, the stroke/position of a strut is accurately measured over an extended-length by using magnetostrictive-pulse transit-time sensors. Inductive position sensors are used on many different places in a modern car, e.g.

accelerator pedal sensors, steering angle position sensors, head lamp position sensors, etc. due to their mechanical variability (linear, rotational...), high temperature range, simplicity and robustness[11].

1.3   Objectives

Due to their outstanding merits, inductive sensors are most suitable for automotive applications where cost and flexibility are critical factors. They have been playing an important role in the automotive sensor family, and more and more automotive applications are switching to inductive sensing technology recently [12-14]. However, inductive position sensors are still not used as widely as magnetic position sensor in the automotive sector. One reason for the relative scarcity of inductive sensors is that their winding pattern makes them relatively big, especially for high accuracy devices that require precise winding. Another technical challenge is the designing of the optimal winding pattern and the rotor shape. Besides, the analysis of the inductive sensor performance heavily relay on Finite element analysis (FEA), which is very time-consuming.

To tackle these technical challenges, a design methodology for a robust and cost-effective inductive position sensor is developed in this work. A mathematic model for the sensor system is essential to understand the dominating factors of the sensor performance. Meanwhile the relation between the sensor raw signal quality and the sensor error need to be understood systematically to improve sensor accuracy. Since the design optimization of the inductive position sensor involves numerous design variables and optimization goals, an efficient optimization method specific for the inductive position sensor needs to be developed.

The objectives of the present work are multifold:

(1) the development of lumped mathematic model of inductive position sensor, which will be used as analytical tool for inductive sensor design and optimization;

(2) miniaturizing the sensor design and the development of its fabrication process to investigate the potential of scaling-down;

(3) the developments of steering torque sensor and its experimental verification to demonstrate the inductive position sensor fusion;

(4) study of a passive inductive position sensor.

The underlying common theme of these objectives is the use of inductive sensing technology.

1.4 Thesis Outline

The reminder of this work is organized as follows.

In section 2 we present the theoretical modeling of inductive position system including the electromagnetic structure, the oscillator circuit and the signal processing. The result is further verified by FEA and SPICE numerical simulation. A sensor system SIMULINK model is developed to present the transient behavior.

In section 3 we analyze the sensor error introduced by the imperfection of sensor raw signals for both two-phase and three-phase configurations. The corresponding correction method is also proposed.

In section 4 we optimize the sensor performance based on the response surface methodology. The method allows us to get an optimal design efficiently.

We develop a miniaturized inductive angular position sensor in section 5, which includes the modeling, numerical simulation, microfabrication process development and experiment validation.

We propose a steering torque sensor in section 6, the challenge and the potential the fusion of multiple inductive sensors are discussed.

In section 7 we demonstrate the development of a passive inductive sensor to meet the low emission and low power consumption requirement.

Chapter 2

2 Theory and Modeling of Inductive Sensor

2.1 Background

An inductive angular position sensor (IAPS) typically comprises an electromagnetic structure and a support circuit[15, 16], which is commonly used to detect the angular position of the target relative to the reference. The electromagnetic structure consists of a transmitting coil, a certain number of receiving coils and a conductive rotor, which interact with each other through inductive coupling. The circuit provides power to sustain an alternating magnetic field, and it also conditions the receiving signal for Analog/Digital (A/D) conversion. The digitized signals are then used to calculate the angle, which is mapped into the desired output type. The output could be analog, Pulse Width Modulation (PWM) or digital format such as Inter-Integrated Circuit (I^2C), Single Edge Nibble Transmission (SENT) or Serial Peripheral Interface (SPI).

To optimize the sensor performance for a specific application, it is critical to model the sensor system that includes both the electromagnetic structure and circuit. Numerical modeling is a popular method to model the IAPS system. The electromagnetic structure can be modeled by FEA, and the impedance matrix of the structure is derived after solving the electromagnetic field with a proper excitation at the coil terminal. The derived impedance matrix is then used in SPICE for circuit simulation. Such method provides good insight of the sensor performance from the perspective of both the electromagnetic field and the circuit. However, both FEA and SPICE circuity simulations are very time-consuming, and therefore, they are not practical when a large variation of design parameters needs to be investigated for sensor performance optimization.

In order to minimize the computation effort, a behavior system model of the IAPS sensor is developed in this work based on the electromagnetic structure and the circuit. This model is first validated by the FEA and the SPICE simulation, and is further used for the sensor's performance analysis and optimization.

2.2 Sensor electromagnetic structure configuration

The minimal configuration of the electromagnetic structure of an IAPS, as shown in Figure 2-1, consists of a transmitting coil (TX), a conductive rotor indicating the target position, and at least two set of receiving coils (RXs). In the two-receiving-coil setup, the RXC coil receives a cosine signal of the rotor position and the RXS coil receives a sine signal of the rotor position. The rotor position can thus be calculated from the arctangent function of these two receiving signals. In some other configurations, three receiving coils are used to achieve better sensor performance. The benefit and signal processing of using three receiving coils will be discussed later in chapter 3.
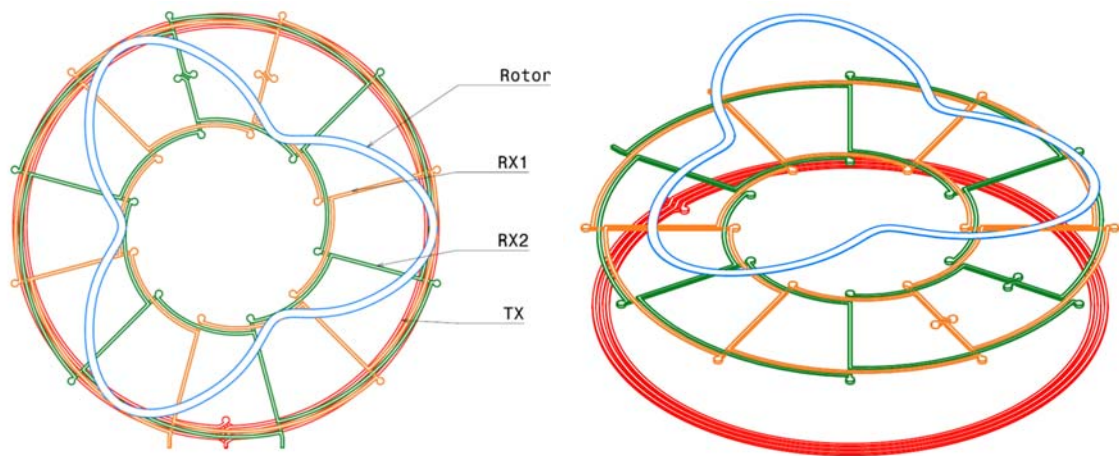
Figure 2-1: IAPS electromagnetic structure top view and isotropic view

2.3 Sensor Working Principle

The excitation coil of the IAPS consists of a few concentric circular loops. Figure 2-2 (a) and (b) shows the FEM results by ANSYS/HFSS. When the excitation coil is energized by an alternating current, an axial symmetric alternating magnetic field is generated at the vicinity. Since the receiving coil is interlaced by a clockwise loop and counterclockwise loop, as shown in figure 2-2(c), no signal will be induced by such an axial symmetric magnetic field as shown in figure 2-2(a). When a conductive rotor (or coupler) is positioned at the adjacent position, an eddy current is induced on this target. The eddy current generates a secondary magnetic field, which makes the resultant magnetic field no longer

axially symmetric as shown in figure 2-2(b). Thus, the receiving coils can pick up signals that represent the coupler position.

(a)   (b)   (c)
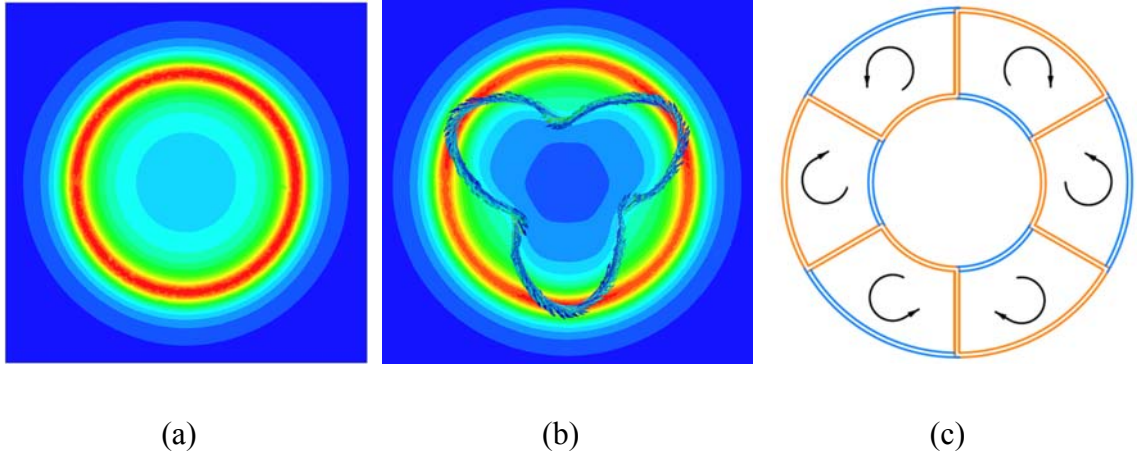
Figure 2-2: (a) Excitation magnetic field; (b) Magnetic field modulated by eddy current; (c) Receiving coil winding.

Since the cross section of the excitation coil is much smaller than the coil's length, the coil can be treated as filamentary wire. The magnitude of the resultant magnetic field generated at location $\vec{r}$ by current I passing through the excitation coil can be computed by using the Bio-Savart law[17], as

$$B_p(\vec{r}) = \frac{\mu_0}{4\pi} \oint_{C_{TX}} \frac{I d\bar{x} \times (\vec{r} - \bar{x})}{|\vec{r} - \bar{x}|^3} \tag{2-1}$$

where path C_{TX} is the center line of the transmitting coil, $d\bar{x}$ is the differential element of the wire in the direction of the current. Since path C_{TX} is axially symmetric, the primary magnetic field induced by the transmitting coil $B_p(\vec{r})$ is also axially symmetric, as demonstrated in Figure 2-2 (a).

When a conductive rotor loop is exposed to the excitation magnetic field, the induced voltage on the loop can be expressed by using Faraday's law of induction,

$$V = -\frac{d}{dt} \iint_{\Sigma_{RT}} B_p \cdot dS \tag{2-2}$$

where Σ_{RT} is the area enclosed by the rotor profile. Consequently, an eddy current is induced on the rotor loop, i.e.,

$$I = \frac{V}{R} \tag{2-3}$$

where R is the rotor loop resistance. The eddy current of the rotor can further generate a secondary magnetic field, which could be expressed as,

$$B_S(\bar{r}) = \frac{\mu_0}{4\pi} \oint_{C_{RT}} \frac{I d\bar{x} \times (\bar{r} - \bar{x})}{|\bar{r} - \bar{x}|^3} \tag{2-4}$$

where c_{RT} is the rotor profile path. Since the rotor profile is not axially symmetric, the secondary magnetic field induced by the eddy current is not axial symmetric either. The total magnetic field is the superimposition of the primary and the secondary magnetic fields, i.e.,

$$B_t(\bar{r}) = B_p(\bar{r}) + B_S(\bar{r}) \tag{2-5}$$

Consequently, the receiving coil picks up a voltage of

$$V_{RX} = -\frac{d}{dt} \iint_{\Sigma_{RX}} B_t dS \tag{2-6}$$

where Σ_{RX} is the area enclosed by the receiving coil.

Although FEA can be used to calculate the sensor signal and performance, it is generally very time-consuming. In the design stage, a wide design variation including different design parameters at different geometrical positions needs to be assessed. An accurate equivalent circuit will help us gain more insight on the critical factors of design and speed up the optimization procedure.

Therefore, we propose a new methodology where the IAPS can be modeled as a two-stage transformer, as shown in Figure 2-3. The first stage is from the transmitting coil to the rotor, while the second one is from the rotor to the receiving coil. The transmitting coil TX

can be modeled as an inductor L_1 and a resistor R_1 connected in series, and the rotor can also be modeled as an inductor L_2 and a resistor R_2 connected in series. The TX and the rotor are inductively coupled through the mutual inductance M_{12}.
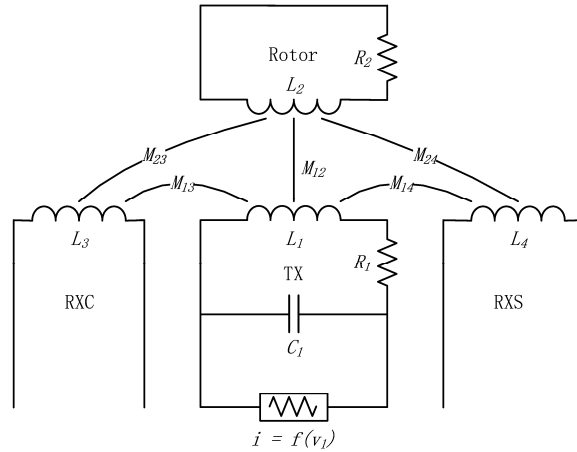
Figure 2-3 Inductive torque sensor equivalent circuit

The TX is energized by an oscillator, which is modeled as a nonlinear resistor, as shown in Figure 2-3. When an alternating current passes through the TX, an eddy current is induced in the rotor through the inductive coupling. The mutual inductive coupling between the TX and the rotor can be modeled from the transformer equation and Kirchhoff's voltage law (KVL) as,

$$\begin{cases} L_1 \dfrac{d}{dt} i_1(t) + M_{12} \dfrac{d}{dt} i_2(t) + i_1(t) R_1 = v_1(t) \\ L_2 \dfrac{d}{dt} i_2(t) + M_{12} \dfrac{d}{dt} i_1(t) + i_2(t) R_2 = 0 \end{cases} \tag{2-7}$$

where $i_1(t)$ and $i_2(t)$ are the branch current through the TX and the rotor, respectively; $v_1(t)$ is the voltage across the TX.

The second stage of the transformer is from the rotor to the receiving coils RXC and RXS, with the receiving signals being expressed as,

$$\begin{cases} v_3(\theta,t) = M_{13}\dfrac{d}{dt}i_1(t) + M_{23}(\theta)\dfrac{d}{dt}i_2(t) \\ v_4(\theta,t) = M_{14}\dfrac{d}{dt}i_1(t) + M_{24}(\theta)\dfrac{d}{dt}i_2(t) \end{cases} \qquad (2\text{-}8)$$

where M_{13} and M_{14} are the mutual inductances between the receiving coils and the TX coil, which are independent of the rotor angle since the TX is axially symmetric; $M_{23}(\theta)$ and $M_{24}(\theta)$ are the mutual inductances between the receiving coils and the rotor, and both are depend on the rotor angle position.

When the TX coil is axial symmetrically wound, and the RX coil consists of clockwise and counter-clockwise segment interlaced alternatively, the mutual inductance between the TX and the RX disappears, i.e., $M_{13} = M_{14} = 0$, due to the geometrical symmetricity. Equation (2.8) is thus reduced to,

$$\begin{cases} v_3(\theta,t) = M_{23}(\theta)\dfrac{d}{dt}i_2(t) \\ v_4(\theta,t) = M_{24}(\theta)\dfrac{d}{dt}i_2(t) \end{cases} \qquad (2\text{-}9)$$

Therefore, the rotor angle position can be derived from signals $v_3(\theta,t)$ and $v_4(\theta,t)$. In practice, since the geometric relation between the RX coils and the rotor repeats after a maximum angle of 2π, the mutual inductance is a periodic function of the angle. It is convenient to design the geometry of the RX coils and the rotor so that their mutual inductance is a sinusoidal function of the angle, i.e.,

$$\begin{cases} M_{23}(\theta) = k\sin(N_p\theta) \\ M_{24}(\theta) = k\cos(N_p\theta) \end{cases} \qquad (2\text{-}10)$$

where the pole number N_p is defined as the number of the periodic features of the RX and the rotor. From equations (2-6) and (2-10), the rotor angle can be derived as,

$$\theta = \frac{1}{N_p}a\tan 2\big(v_3(\theta,t), v_4(\theta,t)\big) \qquad (2\text{-}11)$$

Equation (2-10) shows that the two RX coils have identical geometry, with $\pi/2N_p$ angle offset from each other. The advantage of such a configuration is that the sensor accuracy only depends on the mutual inductance between the RX and the rotor, which will greatly reduce the design complexity.

2.4   Electrical property

Equations (2-7) and (2-9) define the sensor signal. In order to solve the system of equations, the electrical properties used in the equations need to be solved first. This section provides an analytical solution for the electrical properties based on the geometry. Meanwhile, the excitation signal strength can be found by solving the governing equations of the oscillator circuit.

2.4.1 Mutual Inductance

The sensor output relies on the mutual inductances between the rotor and RX coils, which is further determined by the geometry of the rotor and the RX coils. It should be noted that the RXC is a quadrature electrical degree offset of the RXS; therefore, only one set of RX coil needs to be studied.

(a)   (b)   (c)
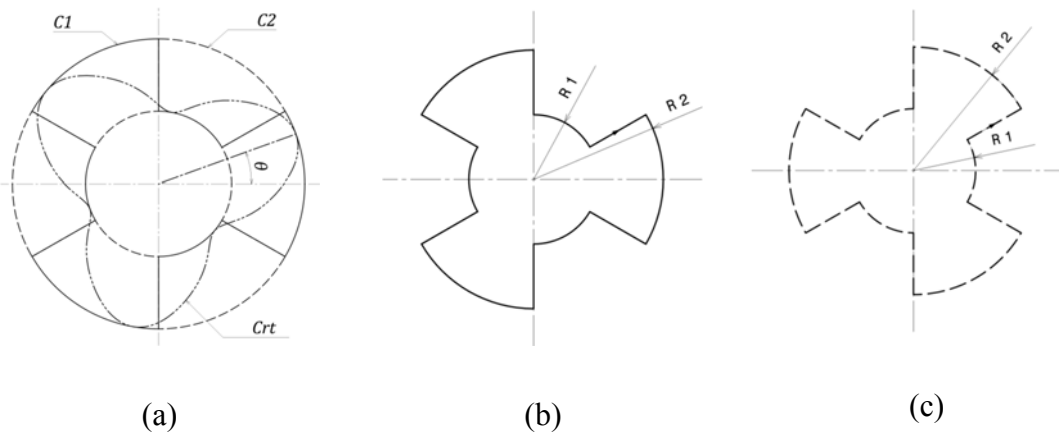
Figure 2-4 (a) Rotor at position (b) and (c) clockwise and counter-clockwise winding of RX coil respectively.

Figure 2-4 shows that the receiving coil can be further decomposed into a clockwise winding C_1 and a counterclockwise winding C_2. Winding C_2 offsets winding C_1 by $\frac{\pi}{N_p}$ for

N_p pole design. Therefore the mutual inductance at position θ between the rotor and the RXC can be computed by using the Neumann formula:

$$M(\theta) = \frac{\mu_0}{4\pi} \oint_{C_{rt}(\theta)} \oint_{C_1 - C_2} \frac{d\vec{r}_1 \cdot d\vec{r}_2}{|\vec{r}_1 - \vec{r}_2|}$$

(2-12)

where $C_{rt}(\theta)$ is the rotor profile path at position θ.

Because of the geometrical relation between C_1 and C_2 as interpreted above, equation (2-12) can be further simplified as:

$$\begin{cases} M(\theta) = M'(\theta) - M'(\theta + \frac{\pi}{N_p}) \\ M'(\theta) = \frac{\mu_0}{4\pi} \oint_{C_{rt}(\theta)} \oint_{C_1} \frac{d\vec{r}_1 \cdot d\vec{r}_2}{|\vec{r}_1 - \vec{r}_2|} \end{cases}$$

(2-13)

Equation (2-13) shows that the sensor output can be fully determined by the double line integral between a receiving coil path C_1 and the path of rotor $C_{rt}(\theta)$.

Due to the geometrical periodicity and symmetry, the mutual inductance $M'(\theta)$ is an even function with a period of $\frac{2\pi}{N_p}$. It can be expressed in Fourier series as:

$$M'(\theta) = \sum_{i=0}^{\infty} C_i \cos(iN_p\theta)$$

(2-14)

When the clockwise winding C_1 and the counterclockwise winding C_2 are combined together, all even terms of the Fourier series are canceled out, and the mutual inductance between the rotor and the receiving coil is reduced to:

$$M(\theta) = \sum_{i=0}^{\infty} 2C_{2i+1} \cos((2i+1)N_p\theta)$$

(2-15)

Equation (2-15) shows that the mutual inductance $M(\theta)$ is not guaranteed to be a sinusoidal function of the angular position, which means that the higher order harmonics

will introduce error to the sensor output. The RX coil shown in Figure 2-4 is optimal since it uses the area most efficiently. The rotor geometry should match with the RX coil to get high signal strength and low high order harmonics. There is no analytical solution of the corresponding rotor geometry for a given RX geometry, which will be optimized using the trial-error method. In the following study three simplest rotor geometries, including eccentric circular, sinusoidal and star shape, are investigated. All those three geometries can be described by two parameters. In the case study, R_1 and R_2 for both the RX and the rotor are set to 7.5 mm and 15 mm, respectively, while the air gap between the RX and the rotor is set to 2 mm. Figure 2-5 shows that the star shape has the highest mutual inductance and the highest harmonics, while the eccentric circle shape has the lowest mutual inductance and harmonics. The sinusoidal rotor shape has a good balance on both the mutual inductance and the high order harmonics; therefore, this shape is chosen for the rotor design. The profile of the sinusoidal shape rotor can be described by:

$$R(\alpha) = \tfrac{1}{2}(R_1 + R_2) + \tfrac{1}{2}(R_2 - R_1)\cos(N_p\alpha), 0 \leq \alpha \leq 2\pi \tag{2-16}$$

where R_1 and R_2 are the max and the min radius of the rotor profile, respectively.
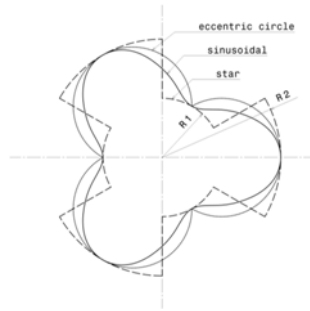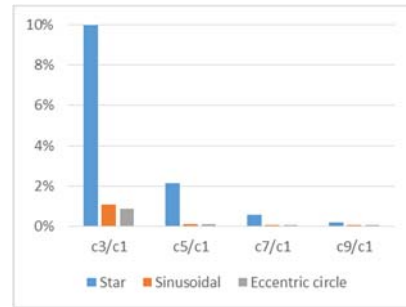
(a)   (b)
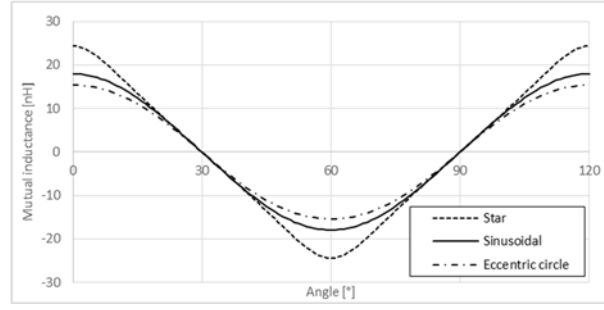
(c)

Figure 2-5 (a) Rotor geometry. (b) Normalized harmonics. (c) Mutual inductance.

2.4.2 Self-inductance

The self-inductance of a filamentary current loop can be approximated by the mutual-inductance of two loops that are spatially separated by the geometrical mean distance (GMD) of its cross section [18].

$$L = \frac{\mu_0}{4\pi} \oint_C \oint_{C+d} \frac{d\vec{x}_1 \cdot d\vec{x}_2}{\sqrt{\vec{x}_1 - \vec{x}_2}} \tag{2-17}$$

where d is the self GMD. The GMD between two areas s_1 and s_2 is defined as:

$$\ln(d) = \frac{1}{S_1 S_2} \int_{S_1} \int_{S_2} \ln(x) ds_2 ds_1 \tag{2-18}$$

The self GMD of a rectangle of width a and height b is [19]:

$$\ln(d) = \ln\sqrt{a^2 + b^2} - \frac{a^2}{6b^2}\ln\sqrt{1 + \frac{b^2}{a^2}} - \frac{b^2}{6a^2}\ln\sqrt{1 + \frac{a^2}{b^2}} + \frac{2a}{3b}\tan^{-1}\frac{b}{a} + \frac{2b}{3a}\tan^{-1}\frac{a}{b} - \frac{25}{12} \tag{2-19}$$

It can be evaluated by a simplified equation (2.20) within 0.2% accuracy for any a and b [19].

$$d = 0.2235(a + b) \tag{2-20}$$

2.4.3 Resistance

At high frequency, the skin effect concentrates the current at the surface of the metallic wire, which reduces its effective cross section and increases the AC resistance. Figure 2-6 demonstrates the current density distribution of an 18 mm diameter circular copper wire with rectangle cross section of 800 μm by 35 μm at 4 MHz frequency in Maxwell 2D. The skin effect makes the current density at the edge of the wire 4 times higher than at the center of the wire.
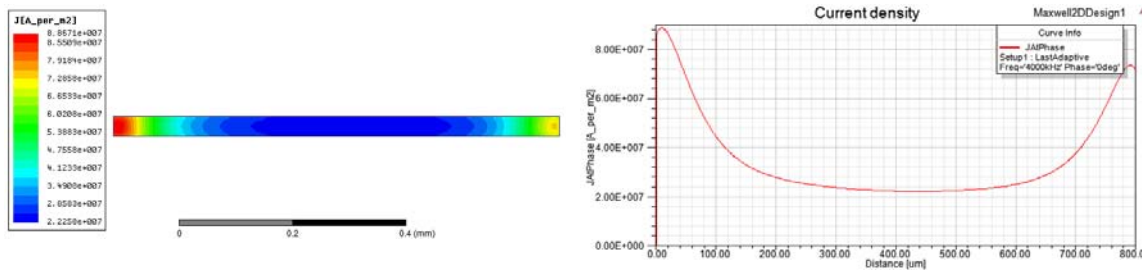
Figure 2-6 Current distribution by skin effect

The resistance caused by the skin depth can be approximated as [20]

$$R_{skin} = R_{DC} \frac{t_0}{\delta \cdot \left(1 - e^{\frac{-t_0}{\delta}}\right)} \cdot \frac{1}{1 + \dfrac{t_0}{w}} \qquad (2\text{-}21)$$

where t_0 and w are the coil thickness and width, respectively, and δ is the skin depth expressed by

$$\delta = \sqrt{\frac{\rho}{\pi f \mu}} \qquad (2\text{-}22)$$

with ρ and μ being the material resistivity and permeability, respectively, and f being the operating frequency.

The presence of the magnetic fields generated by the nearby conductors can alter the current distribution and change the resistance, especially when the space between the

conductors is smaller than the conductor width. This phenomenon is called the proximity effect [21]. Figure 2-7 demonstrates the current distribution of 4 adjacent copper wires simulated by Maxwell 2D, where the current tends to distribute at the most outside.
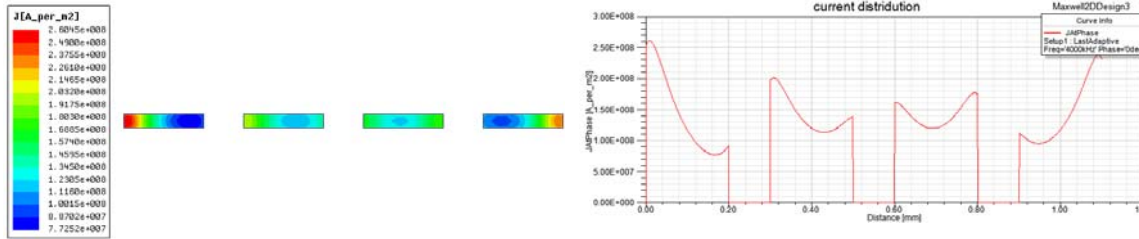
Figure 2-7 Current distribution influenced by proximity effect.

The additional resistance caused by the proximity effect can be evaluated by [22]

$$R_{prox} = R_{DC}\left[1 + \frac{1}{10}\left(\frac{\varpi}{\varpi_{crit}}\right)^2\right]$$

(2-23)

With

$$\varpi_{crit} = \frac{3.1}{\mu_0} \cdot \frac{P}{W^2} R_{sheet}$$

(2-24)

where ϖ_{crit} is the frequency at which the current crowding become significant and R_{sheet} is the metal trace sheet resistance. Therefore, the total AC resistance of the coil by the skin effect and the proximity effect can be evaluated by

$$R_{AC} = R_{DC}\left[1 + \frac{t_0}{\delta \cdot \left(1 - e^{\frac{-t_0}{\delta}}\right)} \cdot \frac{1}{1 + \frac{t_0}{w}} + \frac{1}{10}\left(\frac{\varpi}{\varpi_{crit}}\right)^2\right]$$

(2-25)

2.4.4 Stray Capacitance

The IAPS coils have stray capacitance between the turns and the layers. The stray capacitance of the coil reduces the Q factor of the inductor and also causes self-resonance,

which limits the operating frequency of the sensor. The stray capacitance of a single layer air-core coil is numerically modeled in [23]. For a multilayer coil with N_a layers and N_t turns per layer, the stray capacitance can be approximated as [24],

$$C = \frac{1}{N_t^2} \left[C_b (l-1)m + C_m \sum_{i=1}^{l} (2i-1)^2 (m-1) \right] \tag{2-26}$$

where C_b is the parasitic capacitance between two adjacent turns in the same layer, and C_m is the parasitic capacitance between the two different layers. The parasitic capacitances of the tightly wounded coil can be determined as [24],

$$\begin{cases} C_b = & \varepsilon_0 \varepsilon_r \int_0^{\frac{\pi}{4}} \frac{\pi D_i r_0}{\varsigma + \varepsilon_r r_0 (1-\cos\theta)} d\theta \\ C_m = & \varepsilon_0 \varepsilon_r \int_0^{\frac{\pi}{4}} \frac{\pi D_i r_0}{\varsigma + \varepsilon_r r_0 (1-\cos\theta) + 0.5\varepsilon_r h} \end{cases} \tag{2-27}$$

where D_i, r_0, ε_r, h are the average diameter of coil, wire radius, thickness, and relative permittivity of strand insulation and the separation distance between the two layers, respectively.

FEA or an impedance analyzer can be used to find the impedance characteristic and the resonance frequency of the structure, from which the parasitic capacitance can be derived. However, the simulation results indicate that when the resonance frequency is much higher than the sensor operating frequency, the coil behaves as a pure inductor. Therefore, the parasitic capacitance can be neglected without introducing much error.

2.4.5 Validation

The model proposed is validated by the FEM simulation by using ANSYS Q3D. The FEM model is shown in Figure 2-7(a), its converge criteria is set to 0.1% accuracy. In this model, the thickness of all coils is 35 μm, and the width of the transmitting coil and receiving coil is 0.2 mm. The outer diameter of the transmitting coil and the receiving coil is 24 mm, and the inner diameter of the and receiving coil is 12mm. The result of the model agrees very well with the FEM result as demonstrated by Figure 2-7(b & c) and Table 1. It should

be noted that our model takes less than 5% computing time of the FEM. Therefore, this model will be used in the later analysis of this research.

(a)   (b)   (c)
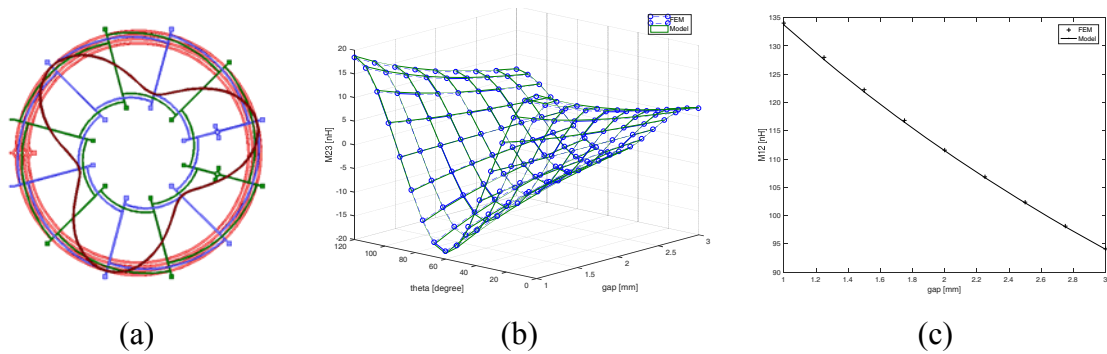
Figure 2-8 (a) FEA model. (b) Mutual inductance between rotor and RX1 coil. (c) Mutual inductance between rotor and TX coil.

Table 2-1 Coil self-inductance and resistance comparison between FEM and model.

	FEA	Model	difference
L1 [µH]	3.163	3.162	-0.06%
R1 [Ohm]	1.415	1.411	-0.27%
L2 [nH]	68.921	68.835	-0.12%
R2 [Ohm]	0.1698	0.170	0.09%

2.5 Sensor Oscillator Driving Circuit

The transmitting coil needs to be energized by a resonant oscillator circuit to compensate for the Ohmic loss. The resonant oscillator typically consists of a frequency selective network or a resonator and a nonlinear amplifier. In an IAPS, the resonator is an LC tank circuit, where the TX coil inherently acts as the inductor and capacitor [11, 25]. Due to their relatively good phase noise performance, ease of implementation in integrated system, and differential operation, cross-coupled inductance–capacitance (LC) oscillators play an important role in the high-frequency sensor applications [26-30].

One implementation of the cross-coupled LC oscillator is a single differential-pair oscillator[27] as shown in Figure 2-7(a). The main advantage of this configuration is that the DC level shift enables a large oscillation amplitude [31]; therefore, this implementation is adopted when the oscillation amplitude is critical for an enhanced signal strength. The

other implementation is a complementary LC-tank oscillator, as shown in Figure 2-7(b), which employs both NMOS and PMOS switching transistors. The advantages of the complementary LC-tank oscillator includes [32] twice the tank voltage swing for the same current consumption, a larger loop gain due to the contribution of both NMOS and PMOS trans-conductance, and a controlled voltage swing that is always within the supply rail.

(a)

(b)

(c)
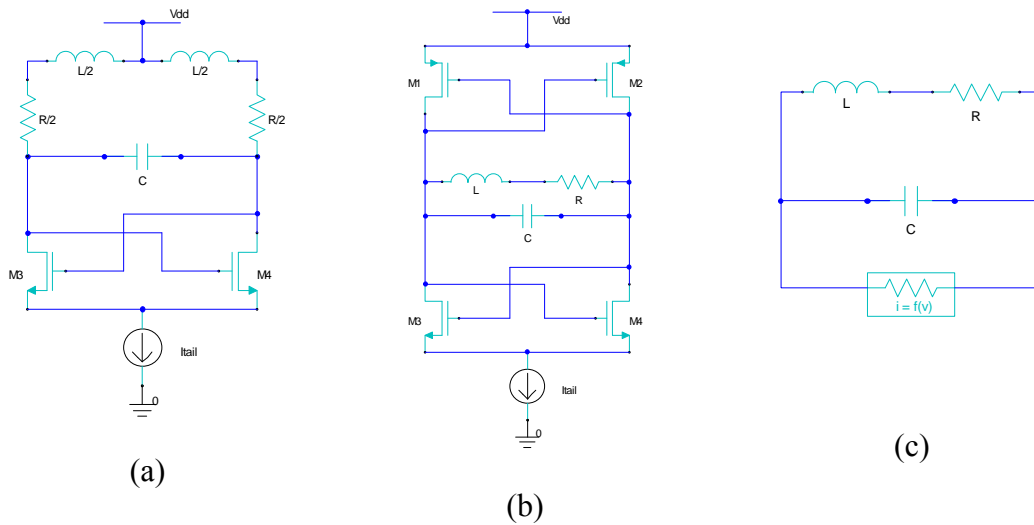
Figure 2-9 (a) Single differential LC oscillator; (b) Complementary LC oscillator; (c) Cross coupled oscillator equivalent circuit.

The free-running oscillator is an autonomous system, which can be modeled as a voltage controlled nonlinear resistor and an LC tank as in Figure 2-7(c). When the oscillator is working in the current-limit regime the voltage amplitude is proportional to the bias current multiplied by the tank parallel losses[33]. The governing equation of the oscillator circuit is given as[34]

$$\begin{cases} L\dfrac{d}{dt}i(t)+i(t)R=v(t) \\ C\dfrac{d}{dt}v(t)+i(t)=S\tanh\left(\dfrac{G_n}{S}v(t)\right) \end{cases}$$ (2-28)

where C, L, R are the tank capacitance, inductance and series resistance, respectively. $v(t)$ is the voltage drop cross the capacitor, $i(t)$ is the branch current of the inductor L, S is the saturation current of the nonlinear resistor, and G_n is the gain of the nonlinear resistor,

which is determined by the transductance of the NMOS and PMOS devices. To understand the circuit oscillation startup condition, linear analysis is conducted. Under small signal condition, the nonlinear resistor can be linearized as,

$$S \tanh\left(\frac{G_n}{S} v(t)\right) = G_n v(t)\big|_{v(t)=0} \tag{2-29}$$

Equation (2-28) is reduced to (2.30) in a matrix form as,

$$\begin{pmatrix} \dfrac{d}{dt} i(t) \\ \dfrac{d}{dt} v(t) \end{pmatrix} = \begin{pmatrix} -\dfrac{R}{L} & \dfrac{1}{L} \\ -\dfrac{1}{C} & \dfrac{G_n}{C} \end{pmatrix} \begin{pmatrix} i(t) \\ v(t) \end{pmatrix} \tag{2-30}$$

To ensure the oscillation starts autonmously, the equation system (2-30) must be unstable. It can be shown that when the following condition is met,

$$G_n > \frac{RC}{L} \tag{2-31}$$

the real part of the eigenvalue of the matrix $\begin{pmatrix} -\dfrac{R}{L} & \dfrac{1}{L} \\ -\dfrac{1}{C} & \dfrac{G_n}{C} \end{pmatrix}$ is positive, and G_n is large enough

to compensate for the Ohmic loss of R. When $\sqrt{\dfrac{L}{C}} \gg R$, a periodic oscillation with the angular frequency given by equation (2-32) will start up.

$$\varpi_0 = \frac{1}{\sqrt{LC}} \tag{2-32}$$

The corresponding SIMULINK model of equation (2-24) is demonstrated in Figure 2-9 (a). The circuit was simulated with the following parameters: $L = 4.2\,\mu H$, $C = 470\,pF$, $R = 3.6\Omega$, $S = 1mA$ and $G_n = -0.0016\Omega^{-1}$. With these selected parameters, the LC tank has a resonant frequency of 3.58MHz, and the oscillator has an operating voltage of 5.99V and an operating current of 63.4mA.

A SPICE simulation with the same parameters is run to validate the model, with the result in comparison with the analytical solution shown in Figure 2-9 (c). The operating voltage of the SPICE simulation is 6.24V. The start-up transient profile of the oscillation voltage also deviates slightly. The error source includes the deviation of the current-voltage relation of the nonlinear resistor and the neglected parasitic conductance and the capacitance of the transistor devices. Based on the comparison, the analytical model is sufficiently accurate to analyze the steady state system behavior.

(a)   (b)   (c)
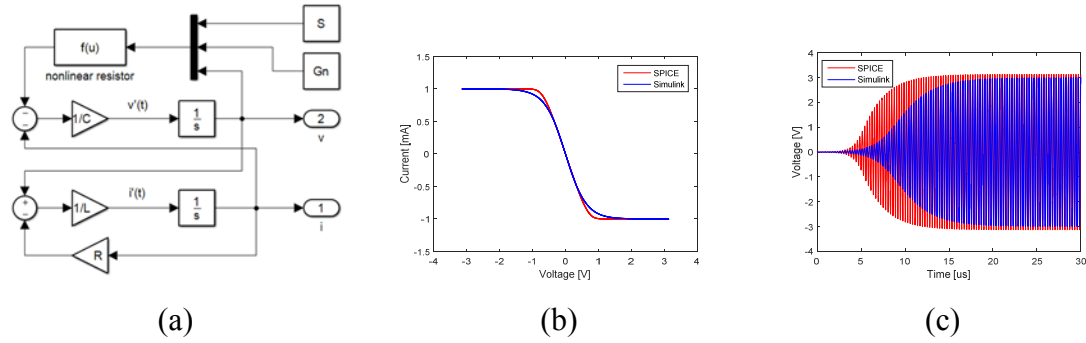
Figure 2-10 (a) Simulink model. (b) I-V curve of the oscillator. (c) Oscillator operating voltage.

2.6   IAPS Electromagnetic Structure Model

Based on the previous discussion, when a rotor is added into the system, the governing equations of the IAPS electromagnetic structure become

$$\begin{cases} L_1 \dfrac{d}{dt} i_1(t) + M_{12} \dfrac{d}{dt} i_2(t) + i_1(t) R_1 = v_1(t) \\ L_2 \dfrac{d}{dt} i_2(t) + M_{12} \dfrac{d}{dt} i_1(t) + i_2(t) R_2 = 0 \\ C_1 \dfrac{d}{dt} v_1(t) + i_1(t) + S \tanh\left(\dfrac{G_n}{S} v_1(t) \right) = 0 \end{cases} \tag{2-33}$$

In the model, the excitation coil L_1 and the rotor L_2 are coupled through the mutual inductance M_{12}, which is a function of air gap z. For small signal analysis, equation (2-33) can be linearized in the matrix form, i.e.,

$$\begin{pmatrix} \dfrac{d}{dt}i_1(t) \\ \dfrac{d}{dt}i_2(t) \\ \dfrac{d}{dt}v_1(t) \end{pmatrix} = \begin{pmatrix} L_1 & M_{12} & 0 \\ M_{12} & L_2 & 0 \\ 0 & 0 & C_1 \end{pmatrix}^{-1} \begin{pmatrix} -R_1 & 0 & 1 \\ 0 & -R_2 & 0 \\ -1 & 0 & G_n \end{pmatrix} \begin{pmatrix} i_1(t) \\ i_2(t) \\ v_1(t) \end{pmatrix} \quad (2\text{-}34)$$

The analytic solution of the oscillation start up condition is quite difficult. However, for any given parameteres, we can check whether the real part of at least one of the eigenvalues

of the matrix $\begin{pmatrix} L_1 & M_{12} & 0 \\ M_{12} & L_2 & 0 \\ 0 & 0 & C_1 \end{pmatrix}^{-1} \begin{pmatrix} -R_1 & 0 & 1 \\ 0 & -R_2 & 0 \\ -1 & 0 & G_n \end{pmatrix}$ is positive. In the design stage, we

can use an approximated formula:

$$G_n > k\frac{R_1 C_1}{L_1} \quad (2\text{-}35)$$

where k is a safety factor greater than 1.

The receiving signal v_3 and v_4 are generated by the current on L_1 and L_2 through the mutual inductance M_{13}, M_{23}, M_{14} and M_{24}. It can be expressed by,

$$\begin{cases} v_3(z,\theta,t) = M_{13}\dfrac{d}{dt}i_1(t) + M_{23}(z,\theta)\dfrac{d}{dt}i_2(t) \\ v_4(z,\theta,t) = M_{14}\dfrac{d}{dt}i_1(t) + M_{24}(z,\theta)\dfrac{d}{dt}i_2(t) \end{cases}$$

M_{13} and M_{14} are all constants independent of the rotor position, while M_{23} and M_{24} are functions of air gap z and rotor angular position θ.

The SIMULINK model of the whole IAPS electromagnetic structure is illustrated in Figure 2-11.
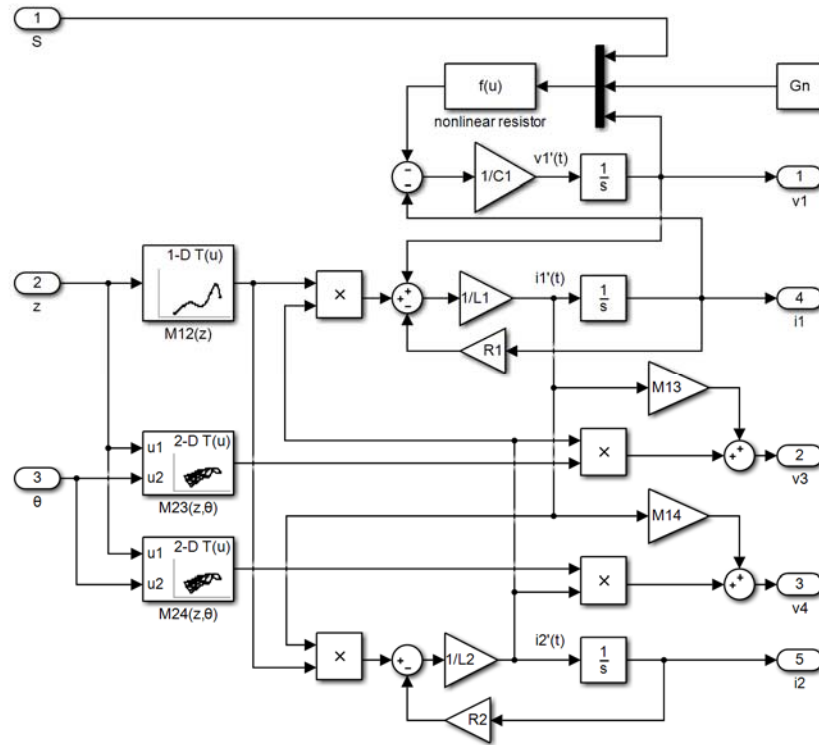
Figure 2-11 IAPS electromagnetic structure model

2.7   Signal Demodulation

The receiving signal is a high frequency signal, which needs to be demodulated and converted to digital format for further signal processing. One demodulation method is the synchronous peak detection, in which signals are sampled at the carrier's peaks. In [35], a pair of quadrature carrier signals were used to demodulate the sensor signals. The signals were sampled using zero crossing detection of the 90 degrees phase shifted carrier signal. This method is attractive since it is simple and can demodulate the signal with no delay. However, the accuracy of this method is prone to the carrier noise.

The demodulation of this sensor uses the excitation signal v_1 as the synchronization reference. Its circuit comprises a comparator, a multiplier and a low pass filter, as shown in Figure 2-12(a). The low pass filter used here is a second order Butterworth filter with the cutoff frequency of 400 KHz, and its Bode plot is demonstrated in Figure 2-11(b). Figure 2-11(c) shows that the demodulation of a 20 KHz signal has negligible phase delay.

(a)   (b)

(c)
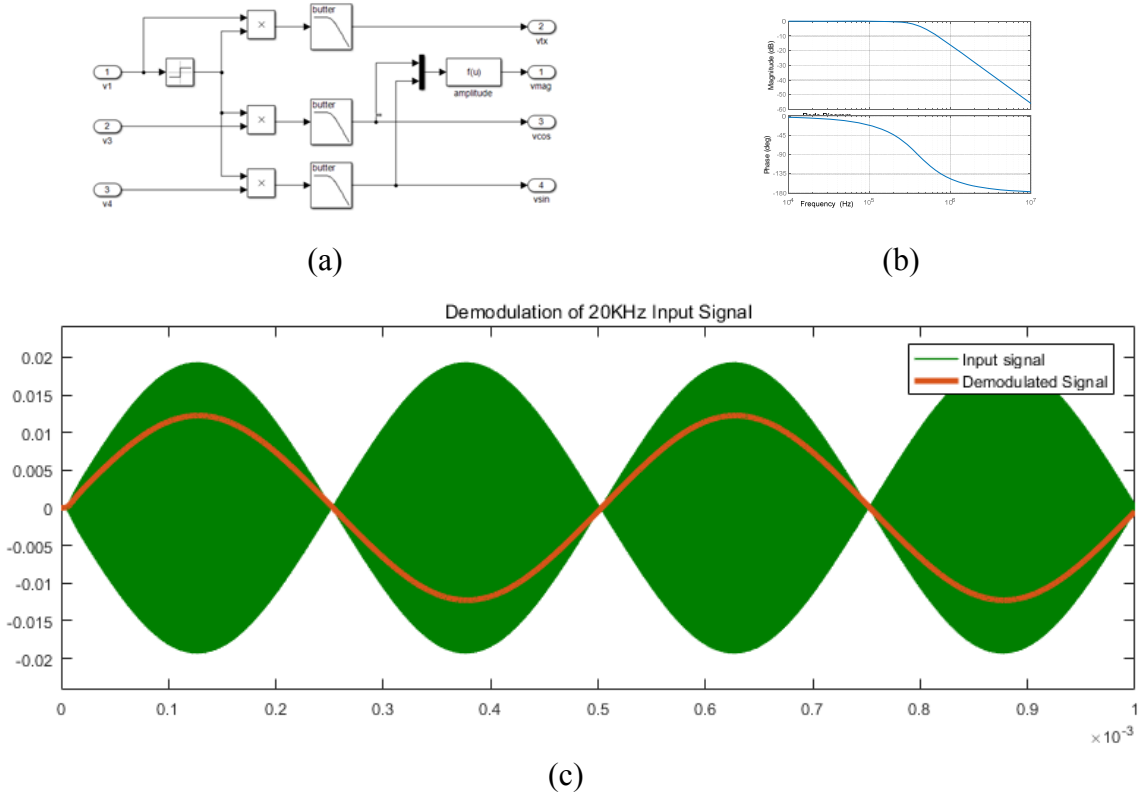
Figure 2-12 (a) Demodulation function block. (b) Bode plot of low pass filter. (c) Reference signal and demodulated signal.

2.8   System Model
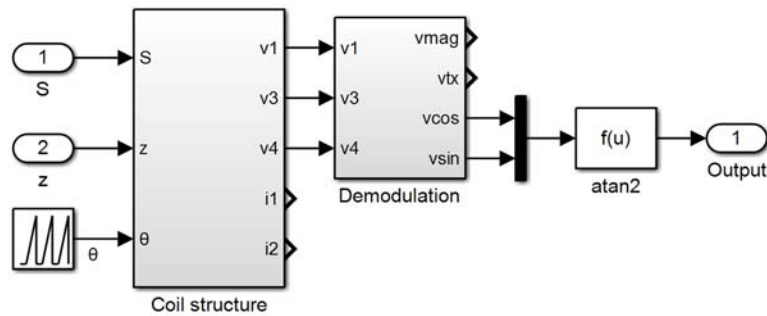
Figure 2-13 IAPS open loop system model

The IAPS system model consists of a magnetic structure block (Figure 2-10), a signal demodulation block (Figure 2-11(a)) and a signal processing block. The signal-processing block calculates the angle from the sine and cosine signals. Figure 2-13 shows the

simulation result at a constant 2 mm air gap. The sensor can detect up to a maximum of 120 degree rotor angle since the output repeats every 120 degrees of the rotor angular position. In the first 30 μs sensor the signal strength gradually builds up. Sensor has low resolution during this transition stage, however sensor still has a correct output since the ratio of two signals remains correct.
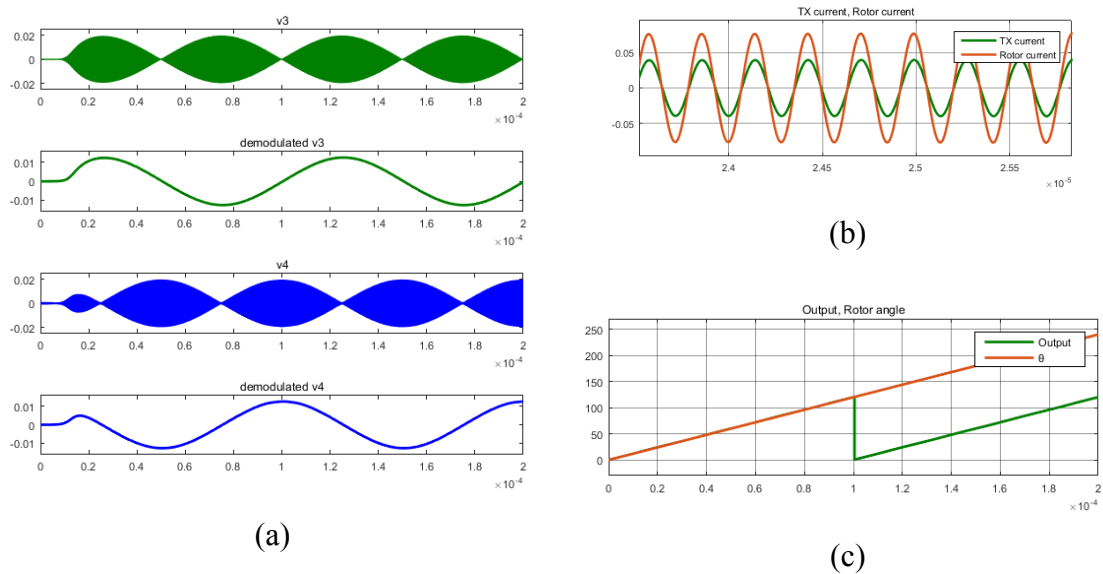
Figure 2-14 (a) Receiving signal and demodulated signal. (b) Excitation current on transmitting coil and eddy current on rotor. (c) Rotor position and sensor output.

2.9   Signal Strength Feedback

In operation condition the sensor might be subjected to geometric variation such as the air gap change. Such variation can cause the output signal change. Figure 2-14 shows the step response of the sensor air gap change. For a constant bias current s and a constant rotor angle, when the air gap changes from 1mm to 2 mm, the excitation current increases due to the reduced load, and the eddy current on the rotor drops because of the reduced mutual inductance M_{12}. The receiving signals v_3 and v_4 drop by half because of the reduced eddy current and reduced mutual inductances M_{23} and M_{24}, however, the sensor output only changes slightly by 0.1 degrees because v_3 and v_4 change by the same scale.
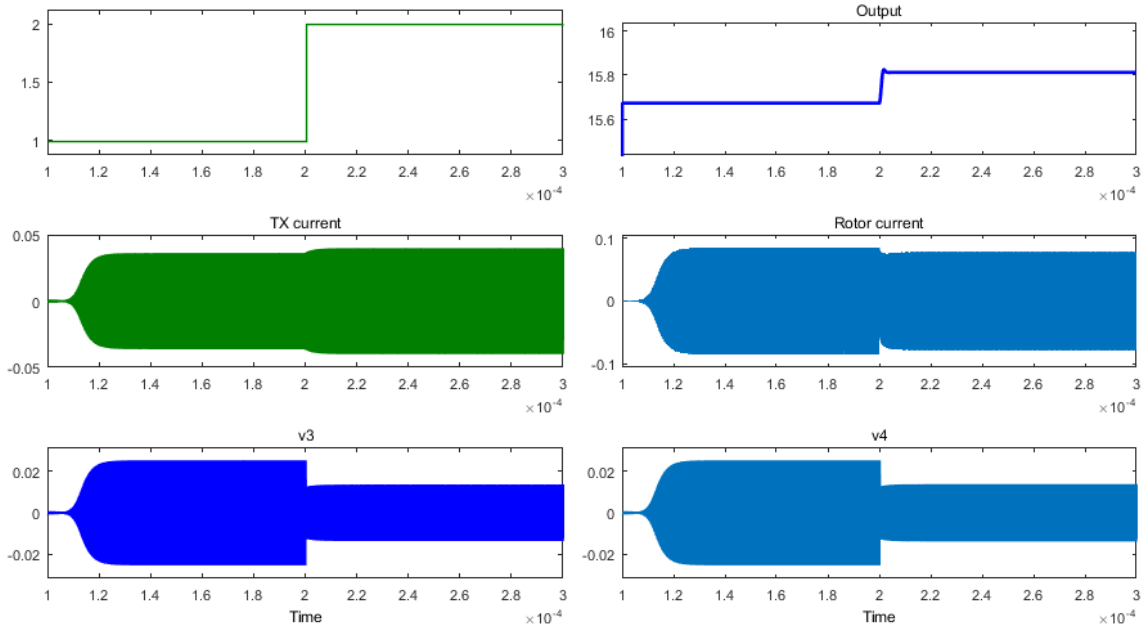
Figure 2-15 Air gap step response

The large variation of signal can cause problems during A/D conversion, i.e., too high signal strength makes the A/D conversion saturated, while too low signal strength leads to a low resolution. To solve this problem, a signal strength feedback close loop is introduced, as shown in Figure 2-15(a). A proportional–integral (PI) controller traces the signal strength to a target value by adjusting the bias current. Figure 2-15(b) shows that when the air gap changes from 1 mm to 2 mm, the bias current is adjusted from 4.4 mA to 8.1 mA so that the signal strength remains at 50 mV. The transient time of 40 µs is acceptable for the sensor with 2 KHz update rate.
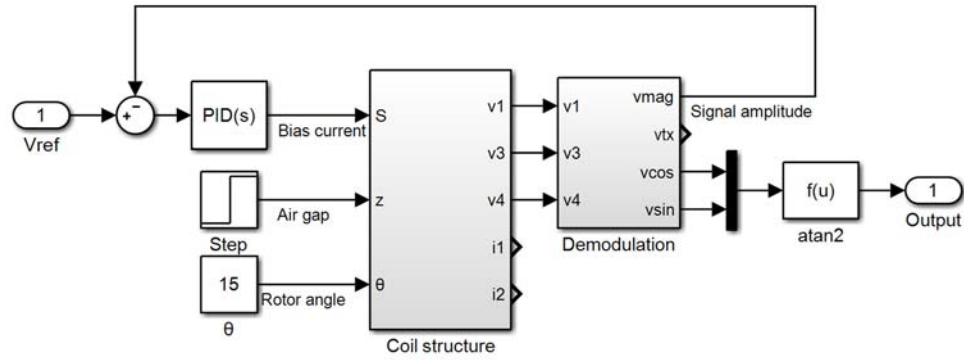
(a)
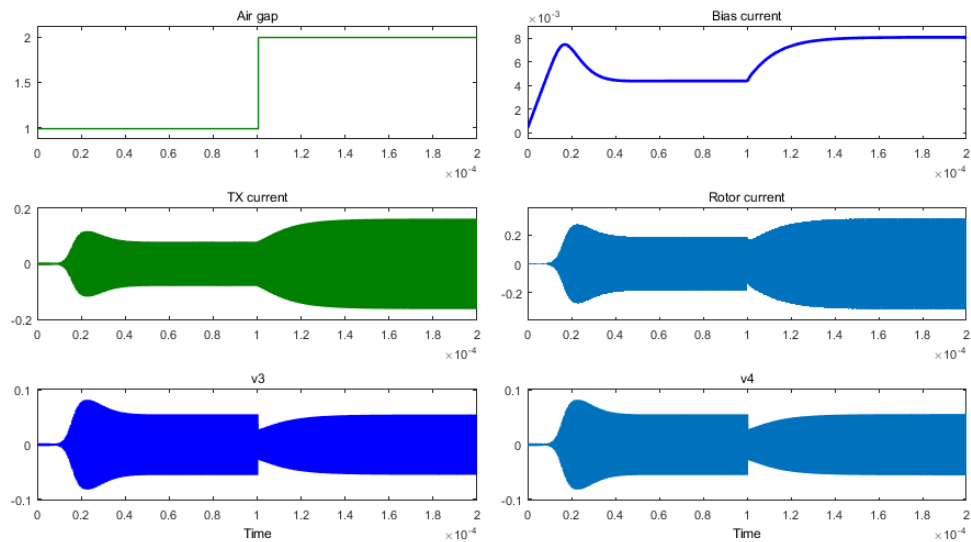
(b)

Figure 2-16 (a) Signal strength feedback loop; (b) Air gap step response.

2.10   Conclusion

A mathematic model of the sensor system is developed in this chapter. The model is first simulated in SIMULINK, then validated by FEM and SPICE simulation. The results of the SIMULINK simulation agree very well with the FEM simulation. The model can be used for design optimization.

To compensate for the signal strength variation due to geometric variation, a PI control close loop is further introduced. The controller can trace the signal strength to a desired level by adjusting the bias current. The simulation also shows that the settle time for an air gap step response is 40 μs, which is sufficient for the 2KHz update rate of the sensor.

Chapter 3

3　IAPS Error Analysis

Accuracy is one of the key performance requirements for sensors. The output error of the IAPS is defined as the difference between the sensor position output and its real position. The allowable output error of the IAPS depends on its specific applications. Improving the accuracy of angular position sensors has received much attention in the literature [36-40].

In order to improve the accuracy of IAPS, it is essential to have a good understanding of its error sources. This chapter first investigates the output error caused by input signal error in two-phase and three-phase sensor configurations. The root causes of input signal error from the sensor implementation and sensor assembly are then studied. The final segment of this chapter discusses possible methods to improve IAPS accuracy.

3.1　Two–phase sensor output error

When the IAPS detects the angle from two input signals, this configuration is defined as a two-phase sensor [38]. In a practical sensor implementation, misalignment of the mechanical placement of the sensor board and the magnet can exist. In addition, there is part-to-part variation between the sensor devices if two discrete devices are used for generating signals with quadrature phase difference. Therefore, the resulting output signal from the sensor will contain undesired harmonics, amplitude variation and phase shift. The various irregularities cause the sensor output to deviate from the ideal case and thereby introduce various errors. In order to analyze the effect of these various signal irregularities on sensor accuracy, the errors are categorized as DC offset mismatch, amplitude mismatch, harmonics content of sine and cosine signals, and quadrature phase shift error. The sensor output error introduced by the signal errors is analyzed in the following part.

The output of the IAPS for an idea signal can be calculated by:

$$\theta = a\tan 2(x, y) \tag{3-1}$$

where x and y are sine and cosine signals with c_l amplitude respectively, i.e.,

$$\begin{cases} x = c_1 \cos(\theta) \\ y = c_1 \sin(\theta) \end{cases} \tag{3-2}$$

When the sensor signal deviates from the ideal signal, the sensor output becomes:

$$\tilde{\theta} = a \tan 2(x + dx, y + dy) \tag{3-3}$$

where dx and dy are the errors of the sine and cosine signals, respectively.

From Taylor's expansion, the sensor output can be expressed as,

$$a \tan 2(x + dx, y + dy) = a \tan 2(x, y) + \frac{xdy - ydx}{x^2 + y^2} + \dots \tag{3-4}$$

Therefore the error of the sensor output can be determined as:

$$\Delta \theta = \tilde{\theta} - \theta \approx \frac{xdy - ydx}{x^2 + y^2} \tag{3-5}$$

3.1.1   DC Offset

The DC offset error in the sine and cosine signals is due to the unbalance between the clockwise and count-clockwise winding. The offset error causes the sine/cosine signal to have unbalanced positive and negative amplitudes and anomalies in the zero crossing. Assuming that the cosine and sine signals have c_{0x} and c_{0y} DC biases, respectively, as illustrated in Fig. 3-1(a), we have,

$$\begin{cases} x = c_1 \cos(\theta) + c_{0x} \\ y = c_1 \sin(\theta) + c_{0y} \end{cases} \tag{3-6}$$

From equation (3-5), the DC offset in the signals induces sensor output error as,

$$\Delta \theta = \frac{c_{0y}}{c_1} \cos(\theta) - \frac{c_{0x}}{c_1} \sin(\theta) \tag{3-7}$$

(a)   (b)
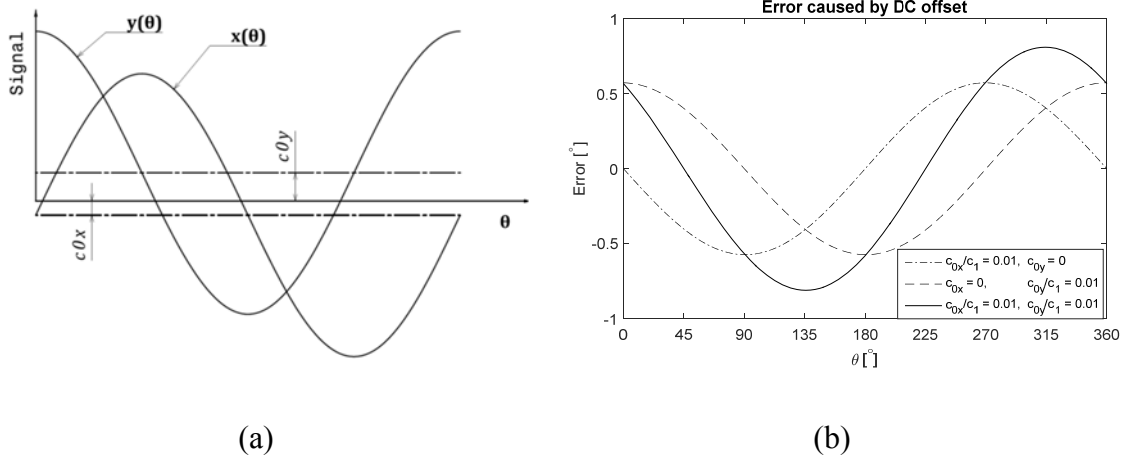
Figure 3-1 (a) Signals with DC offset; (b) Sensor output error caused by DC offset

Fig. 3-1(b) shows the errors caused by the sine and cosine signal DC offset, which have a phase difference of 90 degrees and thus cannot be canceled out. The period of the error caused by the DC offset is 360 degrees.

3.1.2   Amplitude Mismatch

Ideally, both sine and cosine signals should have the same amplitude. Amplitude mismatch occurs when the geometry of the sine and cosine receiving coils are not identical. For instance, if the sine coil and the cosine coil are located at different PCB layers, the coil closer to the rotor will have greater amplitude. If the sine and cosine signals are defined as follows, where the cosine signal has higher amplitude than the sine signal by δ percentage as illustrated in Fig. 3-3(a),

$$\begin{cases} x = c_1 \cos(\theta) \\ y = c_1(1+\delta)\sin(\theta) \end{cases} \tag{3-8}$$

the corresponding sensor error can thus be derived from equation (3-5) as,

$$\Delta\theta = \tfrac{1}{2}\delta\sin(2\theta) \tag{3-9}$$

In most cases, only the 3rd and the 5th harmonics are significant, which dominate the sensor accuracy.

(a)

(b)
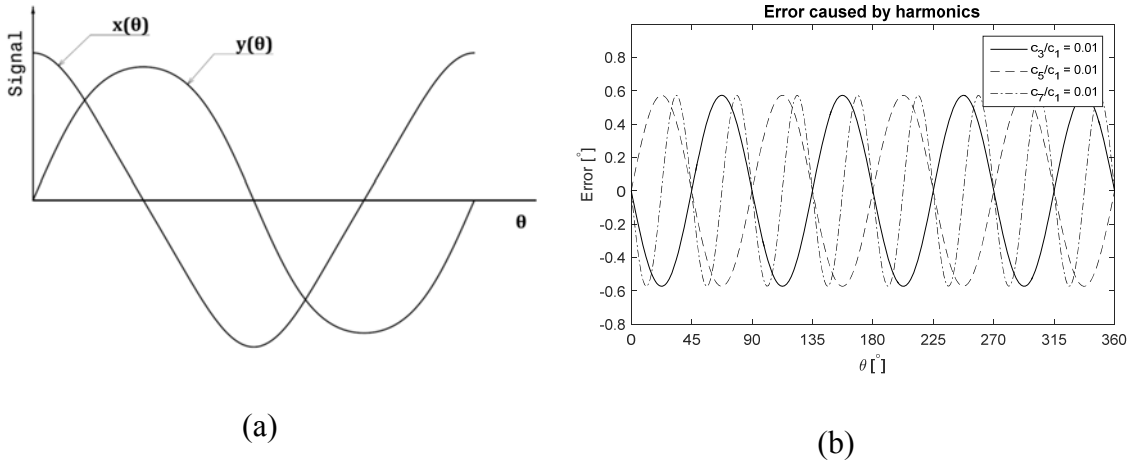
Figure 3-3 (a) Signals with harmonics; (b) Sensor output error caused by harmonics.

Fig. 3-4(b) shows that the errors caused by both 3rd and 5th harmonics have the same period of 90 degrees, and therefore, the error will be canceled out when the harmonics have the same sign. This feature can be utilized to improve sensor accuracy.

3.1.4   Quadrature Phase Shift Error

In ideal cases, the signals should exhibit a quadrature relationship. Due to the imperfect coil implementation, there could be a deviation from quadrature which causes additional error in the sensor output. The quadrature phase shift error ϕ of two signals is defined below, and illustrated in Fig 3-5(a).

$$\begin{cases} x = c_1 \cos(\theta) \\ y = c_1 \sin(\theta + \phi) \end{cases} \tag{3-13}$$

The sine signal can be expressed in Taylor's series:

$$y = c_1 \sin(\theta) + c_1 \cos(\theta)\phi + ... \tag{3-14}$$

The error of the sensor caused by the quadrature phase shift error is thus determined as

$$\Delta\theta = \frac{1+\cos(2\theta)}{2}\phi \qquad\qquad (3\text{-}15)$$

(a)   (b)
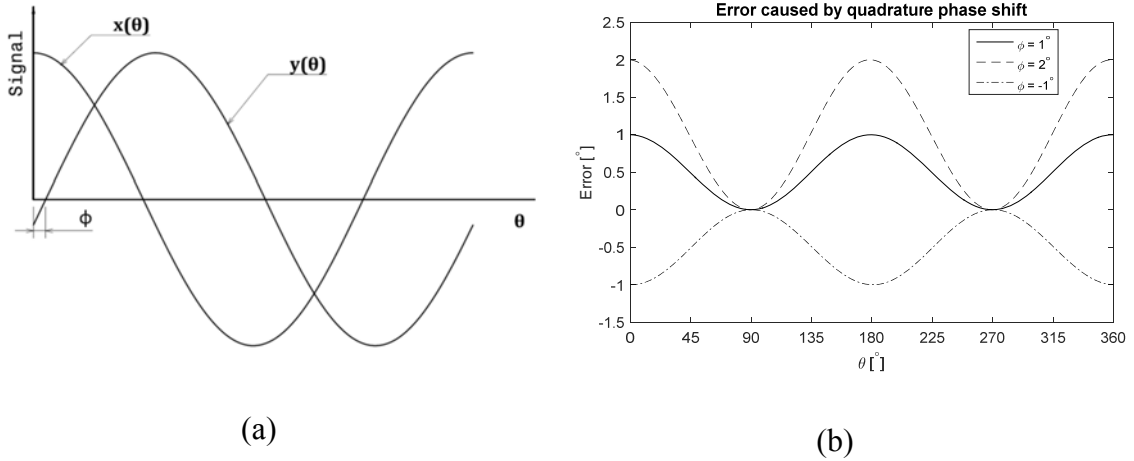
Figure 3-4 (a) Signals with quadrature phase shift; (b) Sensor output error caused by quadrature phase shift

Fig. 3-5(b) shows that the output error caused by the quadrature phase shift has a period of 180 degrees, with the minimal error being zero and maximal error being the same as the phase shift. Therefore, the quadrature phase shift can introduce a mean shift of the output.

3.2   Three–phase Sensor Output Error

An IAPS can also detect the angle from three input signals whose phases are offset by 120 electrical degrees from each other [41]. Such a configuration is defined as a three-phase sensor. Compared to the previous mentioned two-phase sensor, the three-phase sensor is less sensitive to certain input signal errors. However, since the three-phase sensor requires more sophisticated signal processing, its circuitry is more complicated.

In a three-phase IAPS, the three input signals are:

$$\begin{cases} U = c_1\cos(\theta) \\ V = c_1\cos(\theta - \frac{2}{3}\pi) \\ W = c_1\cos(\theta + \frac{2}{3}\pi) \end{cases} \qquad\qquad (3\text{-}16)$$

The sine and cosine signals can be obtained by the following transformation:

$$\begin{pmatrix} x \\ y \end{pmatrix} = \frac{2}{3} \begin{pmatrix} 1 & -\frac{1}{2} & -\frac{1}{2} \\ 0 & \frac{\sqrt{3}}{2} & -\frac{\sqrt{3}}{2} \end{pmatrix} \begin{pmatrix} U \\ V \\ W \end{pmatrix} = \begin{pmatrix} c_1 \cos(\theta) \\ c_1 \sin(\theta) \end{pmatrix} \tag{3-17}$$

After the transformation, the sensor output can be calculated in the same way as the two-phase sensor. Like the two-phase sensor configuration, the input signal irregularities of the three-phase sensor also include the DC offset, the amplitude mismatch, the harmonic error and the phase shift. The following part is the error analysis of the three-phase sensor caused by input signal irregularities.

3.2.1   DC offset

When the three input signals have DC offset c_{0u} , c_{0v} and c_{0w} , respectively, these signals can be expressed as,

$$\begin{cases} U = c_1 \cos(\theta) + c_{0u} \\ V = c_1 \cos(\theta - \frac{2}{3}\pi) + c_{0v} \\ W = c_1 \cos(\theta + \frac{2}{3}\pi) + c_{0w} \end{cases} \tag{3-18}$$

and their corresponding sine and cosine signals are,

$$\begin{cases} x = c_1 \cos(\theta) + \frac{1}{3}(2c_{0u} - c_{0v} - c_{0w}) \\ y = c_1 \sin(\theta) + \frac{\sqrt{3}}{3}(c_{0v} - c_{0w}) \end{cases} \tag{3-19}$$

From equation (3-7), the sensor error can be calculated by:

$$\Delta\theta = \frac{\sqrt{3}}{3} \frac{c_{0v} - c_{0w}}{c_1} \cos(\theta) - \frac{1}{3} \frac{2c_{0u} - c_{0v} - c_{0w}}{c_1} \sin(\theta) \tag{3-20}$$
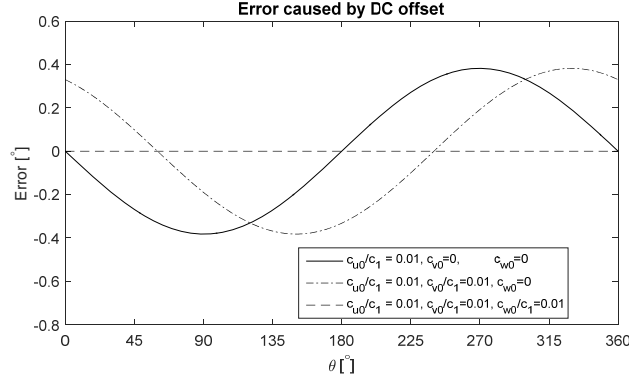
Figure 3-5 Error by signal DC offset in three-phase sensor

The same signal DC offset introduces less sensor error in the three-phase sensor, shown in Fig. 3-6, in comparison to the sensor error of the two-phase sensor, shown in Fig. 3-4(b). Furthermore, in most cases, the DC offsets of the three input signals are identical because of the geometrical symmetry. Therefore, they can be canceled out after the transformation and will not introduce error to the sensor output.

3.2.2   Amplitude mismatch

When the three input signals have different amplitudes, they can be expressed by:

$$\begin{cases} U = c_1 \cos(\theta) \\ V = (1+\delta_v)c_1 \cos(\theta - \frac{2}{3}\pi) \\ W = (1+\delta_w)c_1 \cos(\theta + \frac{2}{3}\pi) \end{cases}$$

(3-21)

where δ_v and δ_w are the mismatch ratio of signal V and W, respectively.

Their corresponding sine and cosine signals are determined as:

$$\begin{cases} x = c_1 \cos(\theta) - \frac{1}{3}c_1\left(\delta_v \cos\left(\theta - \frac{2}{3}\pi\right) + \delta_w \cos\left(\theta + \frac{2}{3}\pi\right)\right) \\ y = c_1 \sin(\theta) + \frac{\sqrt{3}}{3}c_1\left(\delta_v \cos\left(\theta - \frac{2}{3}\pi\right) - \delta_w \cos\left(\theta + \frac{2}{3}\pi\right)\right) \end{cases}$$

(3-22)

From equation (3-7), the sensor error can thus be calculated by:

$$\Delta\theta = \frac{\sqrt{3}}{6}(\delta_w - \delta_v)\cos(2\theta) + \frac{1}{6}(\delta_v + \delta_w)\sin(2\theta)$$

(3-23)

The comparison of Fig. 3-2 and 3-6 shows that the signal amplitude mismatch in the three-phase sensor can introduce comparable error to that of the two-phase sensor.
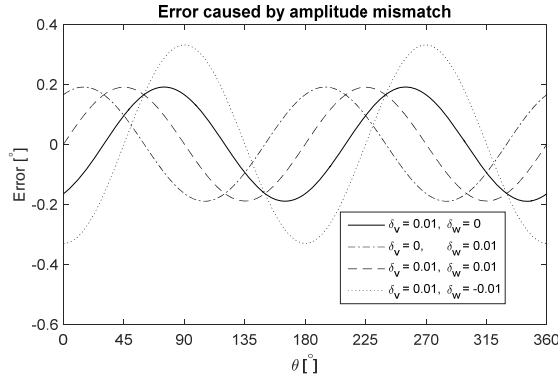
Figure 3-6 Error by signal amplitude mismatch in three-phase sensor

3.2.3   Harmonic error

When the input signals of the three-phase sensor contain higher order odd harmonics, they can be expressed by:

$$\begin{cases} U = \sum_{i=0}^{\infty} c_{2i+1} \cos\big((2i+1)\theta\big) \\ V = \sum_{i=0}^{\infty} c_{2i+1} \cos\big((2i+1)(\theta - \tfrac{2}{3}\pi)\big) \\ W = \sum_{i=0}^{\infty} c_{2i+1} \cos\big((2i+1)(\theta + \tfrac{2}{3}\pi)\big) \end{cases} \tag{3-24}$$

Their corresponding sine and cosine signals are:

$$\begin{pmatrix} x \\ y \end{pmatrix} = \begin{pmatrix} c_1 \cos(\theta) - c_5 \cos(5\theta) + c_7 \cos(7\theta) - c_{11} \cos(11\theta) + ... \\ c_1 \sin(\theta) + c_5 \sin(5\theta) + c_7 \sin(7\theta) + c_{11} \sin(11\theta) + ... \end{pmatrix} \tag{3-25}$$

Equation (3-25) shows the 3rd and the 9th harmonics disappear after the transformation. The sensor output error caused by the input signal harmonics is then determined as:

$$\Delta\theta = \frac{-c_5 + c_7}{c_1} \sin(6\theta) + \frac{c_{11}}{c_1} \sin(10\theta) + ... \tag{3-26}$$
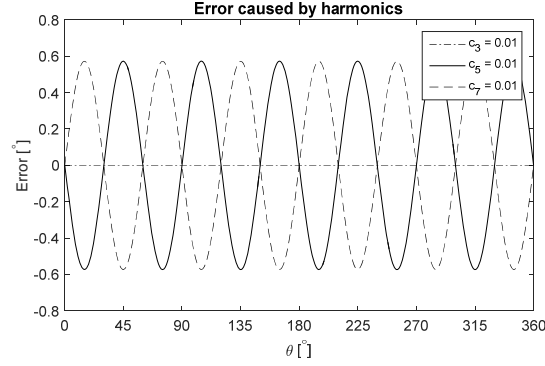
Figure 3-7 Error by signal harmonics in three-phase sensor

Fig. 3-8 shows that for the three-phase sensor, the 3rd harmonic does not introduce sensor error, while both 5th and 7th harmonics can introduce error with a period of 60 degrees.

3.2.4   Phase Shift Error

The input signals of the three-phase sensor with phase shift error can be expressed as:

$$\begin{cases} U = c_1 \cos(\theta) \\ V = c_1 \cos(\theta - \frac{2}{3}\pi + \phi_v) \\ W = c_1 \cos(\theta + \frac{2}{3}\pi + \phi_w) \end{cases} \tag{3-27}$$

Equation (3-27) can be rewritten in the Taylor's series, i.e.,

$$\begin{cases} U = c_1 \cos(\theta) \\ V = c_1 \cos(\theta - \frac{2}{3}\pi) - c_1 \sin(\theta - \frac{2}{3}\pi)\phi_v \\ W = c_1 \cos(\theta + \frac{2}{3}\pi) - c_1 \sin(\theta + \frac{2}{3}\pi)\phi_w \end{cases} \tag{3-28}$$

The corresponding sine and cosine signals are:

$$\begin{cases} x = c_1 \cos(\theta) + \frac{1}{3}c_1\left(\sin(\theta - \frac{2}{3}\pi)\phi_v + \sin(\theta + \frac{2}{3}\pi)\phi_w\right) \\ y = c_1 \sin(\theta) - \frac{\sqrt{3}}{3}c_1\left(\sin(\theta - \frac{2}{3}\pi)\phi_v - \sin(\theta + \frac{2}{3}\pi)\phi_w\right) \end{cases} \tag{3-29}$$

Based on equation (3-7), the sensor error caused by the phase shift is determined as,

$$\Delta\theta = \tfrac{2}{3}\sin^2\!\left(\theta + \tfrac{1}{3}\pi\right)\phi_v - \tfrac{2}{3}\sin^2\!\left(\theta - \tfrac{1}{3}\pi\right)\phi_w \qquad\qquad (3\text{-}30)$$

Figure 3 demonstrates the sensor error caused by different phase shift. It shows that the phase shift can introduce a mean shift of the sensor output, which will be canceled out only if the receiving coils V and W are symmetric about the receiving coil U.
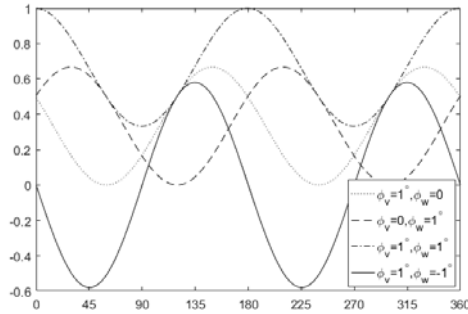
Figure 3-8 Error by signal phase shift in three-phase sensor

3.3   Input signal error analysis

Since only certain specific geometries can generate a perfect sinusoidal signal, the sensor input signals generally include errors. The sensor input signal error can come from a variety of sources. They can be categorized into two main classes. The first class is the imperfect shape of the coil and rotor, and the second class is the deviation of the relative location between the sensor coil and the rotor. In this section, the optimal IAPS geometry, including the number of poles and the shape of the rotor, is investigated. The impact of the assembly tolerance to sensor accuracy is then investigated afterwards.

3.3.1   Number of poles

The number of poles has a strong impact on the high order (mainly 3rd and 5th) harmonics of the receiving signal, as numerically demonstrated in Figure 3-9. Since three-phase configuration can eliminate the 3rd order harmonics, it has significantly better linearity than the corresponding two-phase configuration, as shown in Figure 3-9(e).
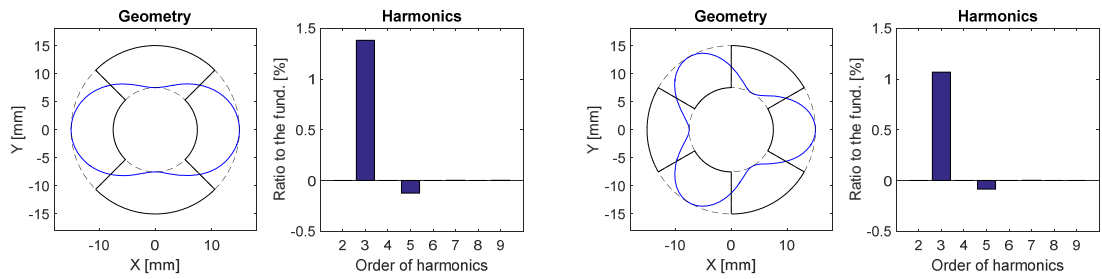
(a)

(b)
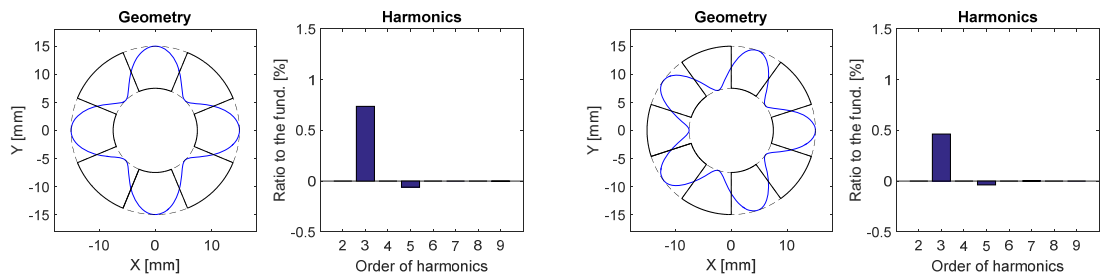
(c)

(d)
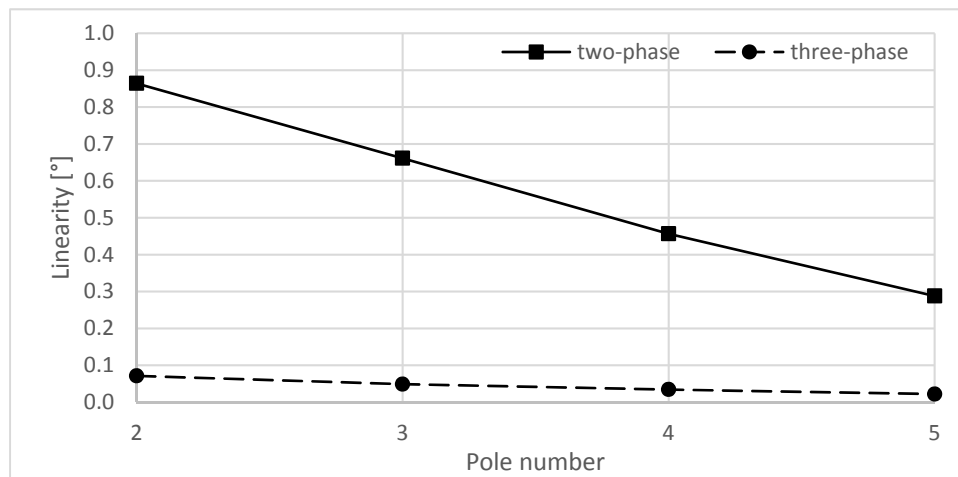
(e)

Figure 3-9 (a-d) the normalized high order harmonics of 2 pole to 5 pole, respectively. (e) linearity of two-phase and three-phase configuration.

3.3.2   Rotor shape
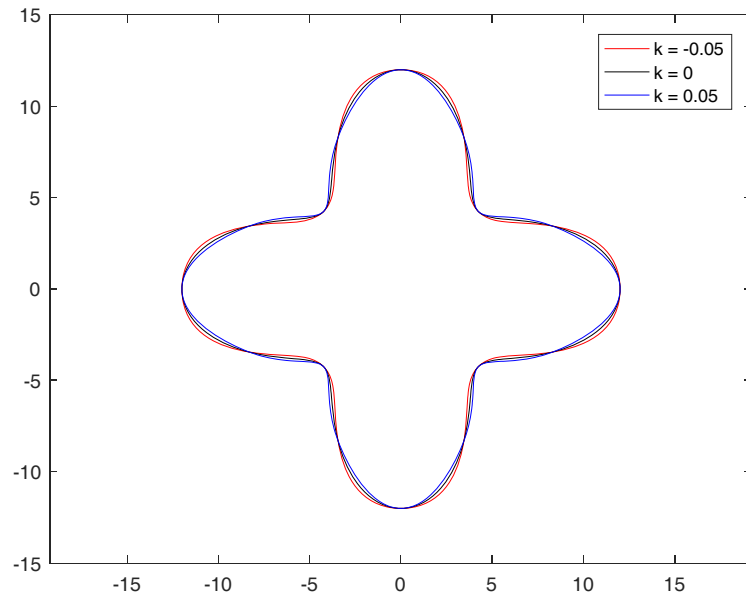
Figure 3-10 Rotor profile with different 3rd harmonics

To improve the sensor linearity, the 3rd harmonic is introduced in the profile. The profile equation then becomes Equation (3-31). Figure 3-10 is a comparison of the profile with different values of the 3rd harmonic coefficient k, in which a positive k makes the tip rounder while a negative k makes the tip sharper.

$$R(\theta) = a + b*(\cos(N_p\theta) + k\cos(3N_p\theta))$$
$$a = \tfrac{1}{2}(R_1 + R_2); b = \tfrac{1}{2(1+k)}(R_2 - R_1) \tag{3-31}$$

Figure 3-11 illustrates the harmonics influenced by rotor geometry. The 3rd harmonics is strongly determined by the rotor geometry harmonic coefficient k, while the 5th harmonics is insensitive to the rotor geometry. When $k = 0.04$, the 3rd and the 5th harmonics are canceled out and the sensor output has the minimum error.
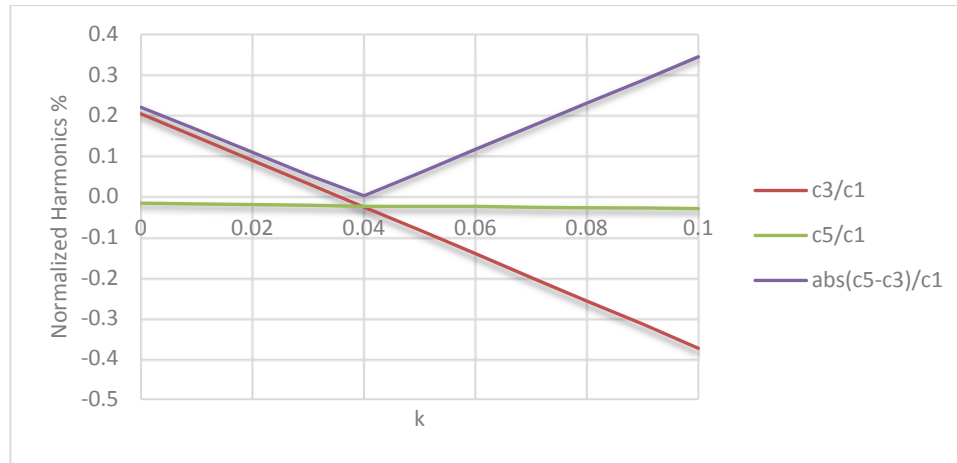
(a)
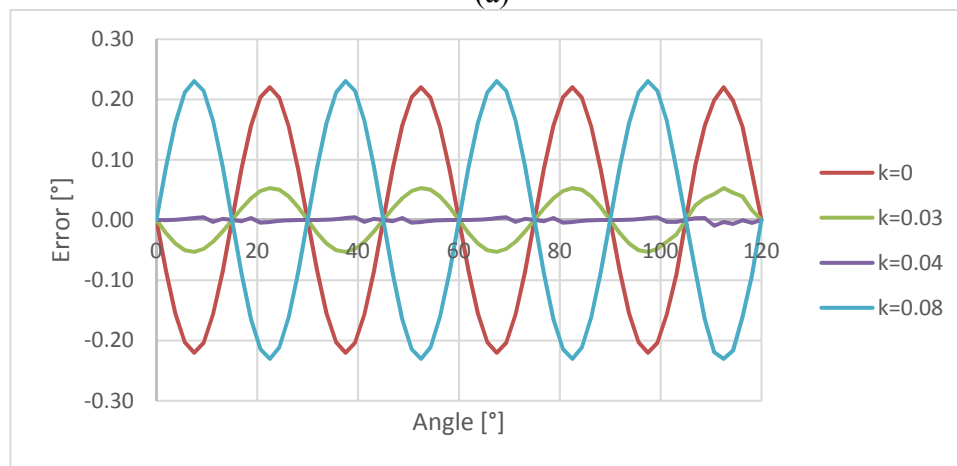
(b)

Figure 3-11 (a) 3rd and 5th harmonics by different rotor shape harmonics. (b) corresponding sensor output error.

3.3.3   Air gap

Air gap not only affects the signal strength, but also influences the harmonics. Therefore, air gap will eventually affect the accuracy. Fig. 3-12 shows that the sensor error reduces when the air gap increases from 1 mm to 3 mm, due to the reduction of higher order harmonics. Meanwhile, the three-phase sensor has significantly less error than the two-phase sensor within the whole range of air gaps considered.
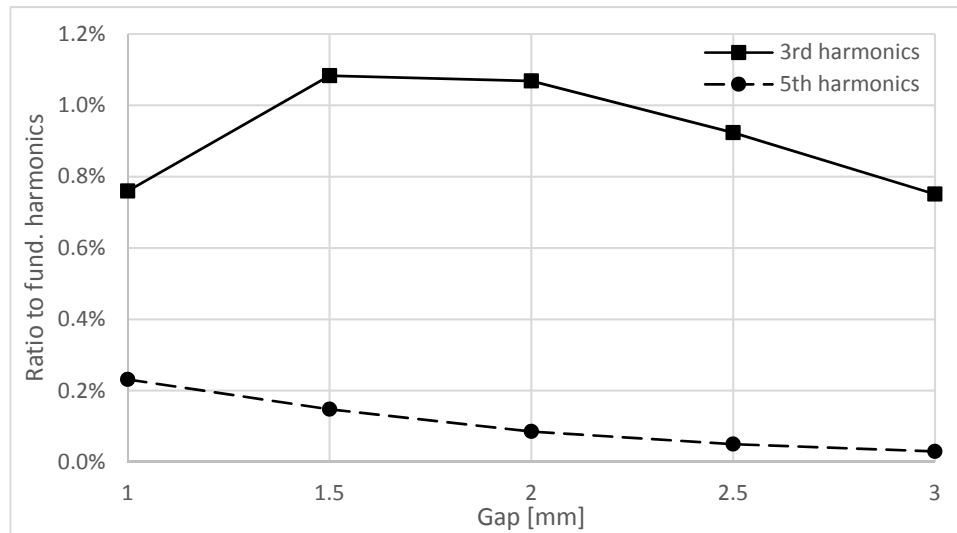
(a)
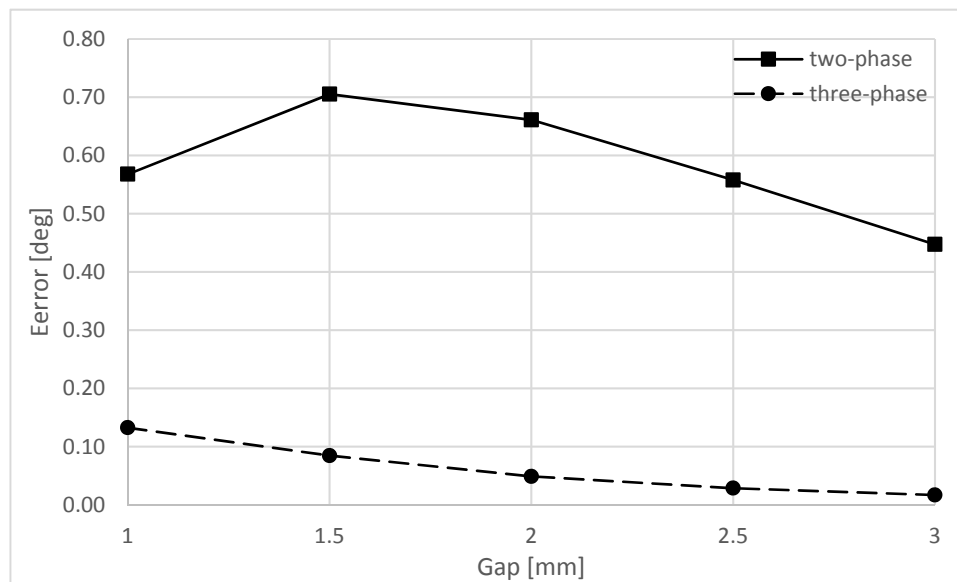
Figure 3-12 (a) Input signal harmonics (b) Sensor error at different air gap

3.3.4   Concentricity

In the IAPS assembly, the rotor could be misaligned with the sensor coil due to the mechanical tolerance, as shown in Figure 13. Such misalignment can introduce more high order harmonics, as shown in Figure 14 (a) and (b), and therefore induce more error to the sensor output. Ideally, sensor output should be immune to the mechanical assembly error.
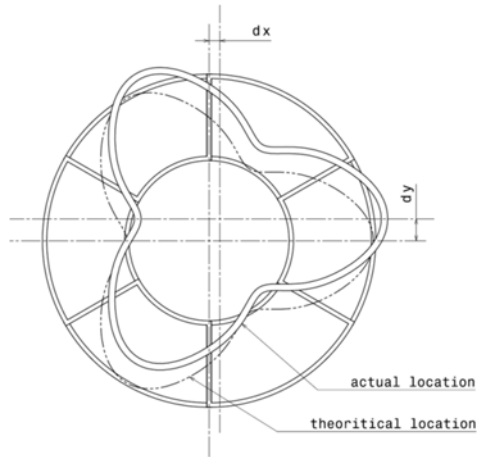
Figure 3-13 Rotor misaligned with IAPS coil

The IAPS output is insensitive to the mechanical misalignment, as demonstrated in Figure 3-14 (c) and (d). In the two-phase configuration, ±1mm misalignment in both X and Y directions only causes 0.06% F.S. error. In the three-phase configuration, such misalignment causes virtually no extra error because the effect of the 3rd harmonics is eliminated. The superior performance of the IAPS is due to the symmetric geometry design.

(a)

(b)

(c)   (d)
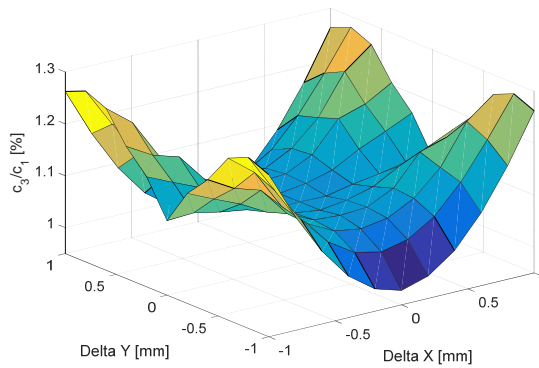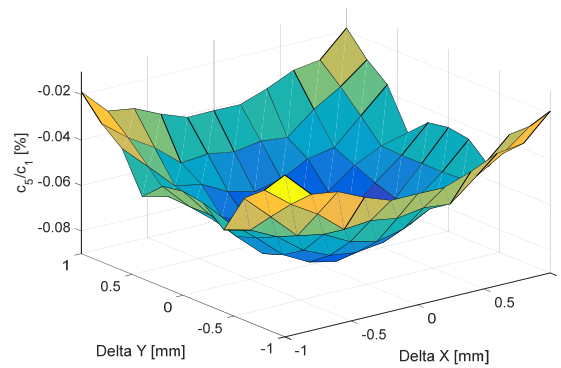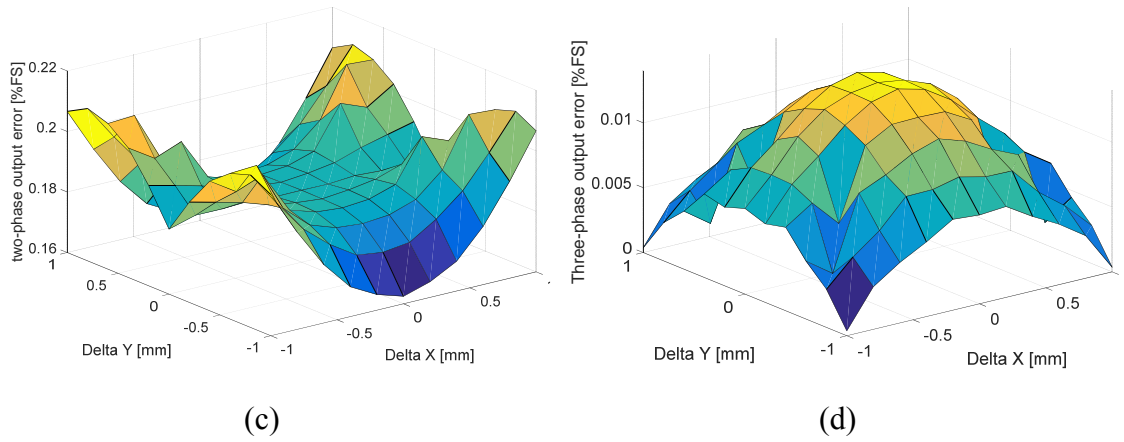
Figure 3-14 (a) & (b) normalized 3rd and 5th harmonics vs. rotor offset of two-phase configuration respectively. (c) & (d) sensor output error vs. rotor offset of three-phase configuration respectively.

Chapter 4

4   IAPS Optimization

4.1   Introduction

To meet the sensing performance and cost requirement, the inductive angular position sensor (IAPS) needs to be optimized globally due to the nature of the objective functions in electromagnetic field. In past literature, global optimizers such as the genetic algorithm [42], simulated annealing algorithm [43], tabu search [44], evolutionary and social interactions [45], are commonly incorporated into the computer simulation package to conduct optimization, which generally requires intensive simulation with multiple iterations. Nevertheless, the direct functional relationship between the performance and the design parameters is still not clear even with those procedures.

Alternatively, response surface methodology (RSM) has been widely used for global optimizations of electromagnetic devices [13–17]. Compared with the aforementioned optimizers, RSM is constructed to determine the functional relationship between the design parameters and the performance. The response surface model can be used to predict the responses of a series of vectors, which makes the optimization procedure very efficient. In addition, RSM can reveal the functional relationship between the performance and the design parameters.

4.2   Response surface methodology

RSM is an optimization method first introduced by Box and Wilson in the early 1950s [46]. It uses a group of mathematical and statistical models to develop the empirical relationship between a response of interest denoted by y and a number of control variables denoted by $x_1, x_2, \ldots, x_k$. In general, such a functional relationship can be approximated by a polynomial model [47] expressed as

$$y = f(\vec{x})\beta + \varepsilon \tag{4-1}$$

where $\vec{x} = (x_1, x_2, \ldots, x_k)^T$. In general, $f(\vec{x})$ is a vector function of p elements consisting of the powers and cross-products of powers of $x_1, x_2, \ldots, x_k$, β is a coefficient vector of p components, and ε is a random error having a zero mean.

In particular, a second order model is commonly adopted for the RSM, i.e., [48]

$$y = \beta_0 + \sum_{i=1}^{k} \beta_i x_i + \sum_{i=1}^{k} \sum_{j=1}^{i} \beta_{ij} x_i x_j + \varepsilon \tag{4-2}$$

This model can be used to establish an approximate relationship between y and $x_1, x_2, \ldots, x_k$ to predict the response according to the given control variables. Thus, the optimum settings of $x_1, x_2, \ldots, x_k$ for the maximum (or minimum) response over a certain region can be determined.

In order to determine the coefficients β_i, n series of experiments are conducted first, in which the response y is measured for given control variables. In the optimization algorithm, a $n \times k$ design matrix denoted by D is first constructed for the experiments

$$D = \begin{bmatrix} x_{11} & x_{12} & \cdots & x_{1k} \\ x_{21} & x_{22} & \cdots & x_{2k} \\ \vdots & \vdots & \ddots & \vdots \\ x_{n1} & x_{n2} & \cdots & x_{nk} \end{bmatrix} \tag{4-3}$$

where x_{ij} is the ith setting of the control variable x_j. Accordingly, the multi-variable response according to this optimization model can be expressed in the matrix form as

$$\vec{y} = X\vec{\beta} + \varepsilon \tag{4-4}$$

where $\vec{y} = (y_1, y_2, \ldots, y_n)'$, representing the measured responses as targeted for optimization. X is a $n \times p$ matrix whose ith row is $f(\vec{x}_i)$, with $\vec{x}_i$ being ith row of the matrix D. The first column of X is unity.

The so-called ordinary least-squares estimator of β [49] can be determined as

$$\hat{\beta} = (X'X)^{-1} X'y \qquad\qquad (4\text{-}5)$$

The predicted response $\hat{y}(x)$ is

$$\hat{y}(x) = f(x)\hat{\beta} \qquad\qquad (4\text{-}6)$$

It is very important to choose a proper design in RSM study because the prediction quality depends on the design matrix D. The design matrix D is preferred to be orthogonal, i.e. the matrix $X'X$ is diagonal, so that the elements of $\hat{\beta}$ will be uncorrelated. The most common designs are the central composite [46] and Box–Behnken design [50]. The central composite design (CCD), also known as Box-Wilson design, is widely used for calibrating a full quadratic model. There are three types of CCDs—circumscribed, inscribed, and faced, as demonstrated by Figure 4-1. Both circumscribed and inscribed CCD designs have a circular, spherical, or hyperspherical symmetry and require 5 levels for each factor. In other words, an inscribed CCD is a scaled down circumscribed CCD; the difference between them is that the circumscribed CCD explores the largest process space while the inscribed CCD explores the smallest process space. Faced CCD only requires 3 levels of each factor.
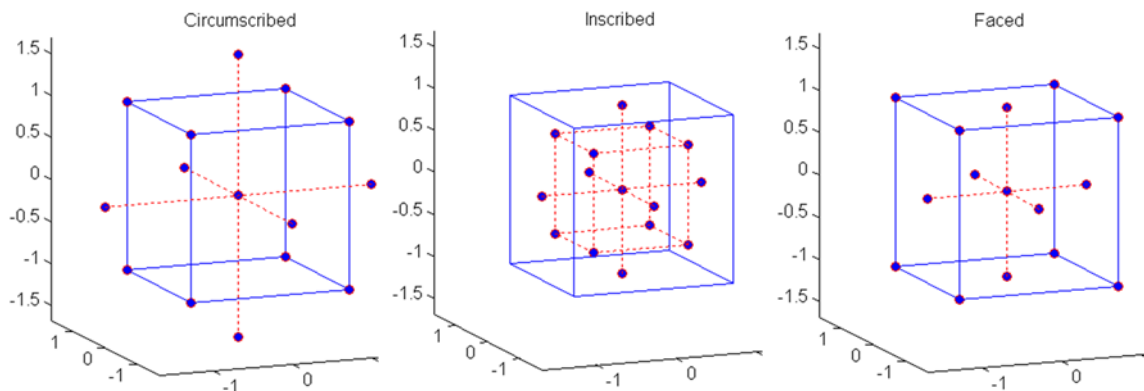
Figure 4-1 central composite design

Another popular design used in industry was developed by Box and Behnken [50]. It consists of a particular subset of the 3k factorial design. Box-Behnken design is shown in Figure 4-2. It is economical as it requires only 3 levels (-1 0 1) for each factor. However,

this design is poor in predicting the extreme condition since the corner points are not included.
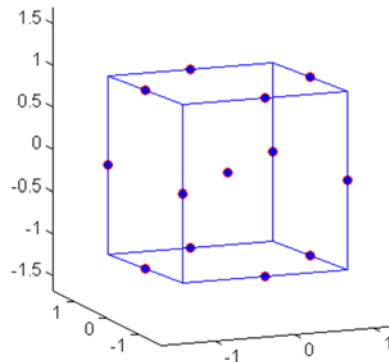
Figure 4-2 Box-Behnken design

4.3   RSM for IAPS optimization

The key performance requirements of the IAPS include an optimal linearity, minimal power requirement and minimal TX voltage swing. Good linearity of the sensor can assure good accuracy and simplifies the signal processing procedure. Low TX voltage swing can drop the supply voltage requirement. IAPS is a complex and multivariate system, and the relation between the design variables and the sensor performance is highly nonlinear. Accordingly, it is impractical to model the effects of every combination of IAPS design factors. Therefore, statistical design of experiments (DoE) methodology is explored to efficiently create accurate models for predicting the performance of IAPS, i.e., only a specific subset of the full combinations of experiment is adopted to predict the contribution of all parameters. To produce accurate parametric models for this complex system, the following steps of RSM procedure is conducted:

1. Identifying the design constraints and the most influential variables to the response, including the prescribed and design variables. The experimental cost is expensive when the number of variables is large, therefore, DoE is applied to minimize the number of experiments.

2. Designing and conducting a series of experiments to get sufficient measurements of the response to a given setting of control variables.

3. Developing mathematical models of the response surface with the least square surface fittings.

4. Finding the optimal design parameters that produce a maximum or minimum value of the response.

4.3.1 Design Variables

Table 4-1 IAPS design parameters

Parameter	Description	Value
R_{tx}	Outer radius of transmitting coil	9mm
w_{tx}	Width of transmitting coil	TBD
N_{tx}	Turns of transmitting coil	TBD
s_{tx}	Spacing between transmitting coil loops	0.2mm
R_{rx1}	Inner radius of receiving coil	TBD
R_{rx2}	Outer radius of receiving coil	9mm
z_{13}	Gap between transmitting coil and receiving coil	0.88mm
z_{23}	Gap between rotor and receiving coil	2mm
t	Coil thickness	35µm
R_{rt1}	Rotor inner radius	TBD
R_{rt2}	Rotor outer radius	9mm
w_{rt}	Rotor coil width	TBD

Above are a set of constrained parameters that are imposed by factors associated with the IAPS. These parameters usually define the size constraints as limited by packaging space. Other factors are related to the fabrication technology, such as the minimum size features according to economical mass production. The definition of these parameters is shown in Fig. 4-3. Among those parameters, the coil thickness is determined by the PWB manufacturing, and the outer diameters of TX, RX coil and Rotor are limited by the mechanical packaging space. The air gap between the rotor and RX coil is also constrained by the mechanical design. Some parameters and their prescribed values of the sensor are listed in table 4-1, while five design parameters are identified to be used for optimization of sensor performance, i.e.,

- width of the transmitting coil w_{tx},

- number of turns of the transmitting coil N_{tx},

- inner radius of the receiving coil R_{rx1},

- inner radius of the rotor R_{rt1},

- the rotor coil width w_{rt}.

(a)   **(b)**
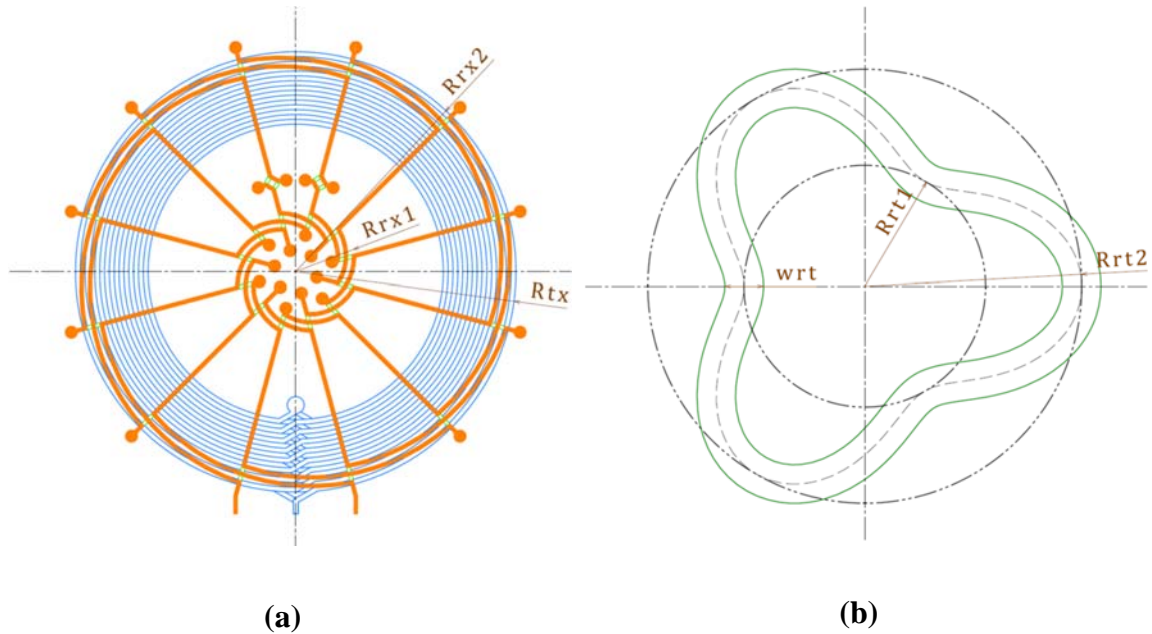
Figure 4-3 Design parameters of (a) sensor coil, (b) rotor

4.3.2   Experiment setup

Since a three level full factor design of 5 variables requires 243 parameters, to minimize the number of experiments, the faced central composite design (CCD) is used to screen the most influential parameters. The experiment configuration is shown in Fig. 4-4. A total of 28 design variations are first generated at the design variation block, and the complete list of all parameters is provided in table 4-2. The corresponding impedance parameters are then calculated based on the method introduced in chapter 2, and the linearity of the sensor can be calculated at the same time. The receiving signal strength and the voltage swing of the transmitting coil are simulated in the circuit simulation and demodulation block. In this configuration, a PI controller is used to make the receiving signal strength target 100mV by adjusting the bias current.
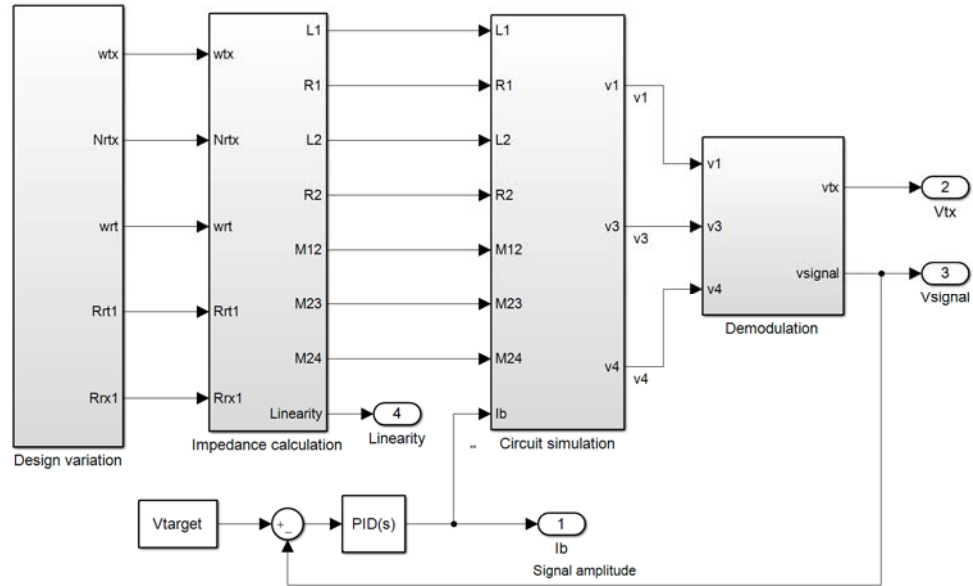
Figure 4-4 Experiment configuration

Table 4-2 Design variation and simulation result

No.	w_{tx} (mm)	N_{tx}	R_{rx1} (mm)	R_{rt1} (mm)	w_{rt} (mm)	v_1 (V)	I_b (mA)	L (degree)
1	0.2	4	4	0.8	2.8	17.94	1.696	0.061
2	0.2	4	5	0.8	1.8	17.42	1.868	0.101
3	0.2	4	4	1.6	1.8	13.96	1.356	0.059
4	0.2	4	5	1.6	2.8	13.06	1.512	0.101
5	0.2	8	4	0.8	1.8	22.54	1.354	0.059
6	0.2	8	5	0.8	2.8	22.16	1.49	0.101
7	0.2	8	4	1.6	2.8	17.74	1.09	0.061
8	0.2	8	5	1.6	1.8	16.7	1.2	0.101
9	0.4	4	4	0.8	1.8	14.18	1.876	0.059
10	0.4	4	5	0.8	2.8	14.74	2.124	0.101
11	0.4	4	4	1.6	2.8	11.1	1.516	0.061
12	0.4	4	5	1.6	1.8	11.06	1.722	0.101
13	0.4	8	4	0.8	2.8	16.62	1.688	0.061
14	0.4	8	5	0.8	1.8	17.4	1.902	0.101
15	0.4	8	4	1.6	1.8	12.92	1.354	0.059
16	0.4	8	5	1.6	2.8	13.06	1.536	0.101
17	0.2	6	4.5	1.2	2.3	17.2	1.366	0.084
18	0.4	6	4.5	1.2	2.3	13.52	1.646	0.084
19	0.3	4	4.5	1.2	2.3	13.48	1.584	0.084

20	0.3	8	4.5	1.2	2.3	16.46	1.408	0.084
21	0.3	6	4.5	0.8	2.3	18	1.658	0.084
22	0.3	6	4.5	1.6	2.3	13.42	1.322	0.084
23	0.3	6	4	1.2	2.3	16	1.408	0.059
24	0.3	6	5	1.2	2.3	15.7	1.56	0.101
25	0.3	6	4.5	1.2	1.8	15.14	1.458	0.084
26	0.3	6	4.5	1.2	2.8	15.14	1.46	0.085
27	0.3	6	4.5	1.2	2.3	15.14	1.458	0.084
28	0.3	6	4.5	1.2	2.3	15.14	1.458	0.084

4.3.3   Second-order response surface model

Based on the simulation result, a second-order response surface model with three tasks regarding to the bias current I_b, TX coil voltage swing v_1 and linearity L can be developed using equation (4-5). This model is graphically demonstrated in Fig. 4-5. It shows that the bias current I_b is positively correlated to the transmitting coil width w_{tx}, and the rotor inner radius R_{rt1}, and I_b is negatively correlated to the TX coil turn number N_{tx} and rotor width w_{rt}. The TX coil voltage swing v_1 is positively correlated to N_{tx} and negatively correlated to w_{tx} and w_{rt}, respectively. The linearity L is positively correlated to R_{rt1}. All these three targeting responses are not correlated to R_{rx1}; therefore, in the next iteration of optimization, R_{rx1} does not need be included.
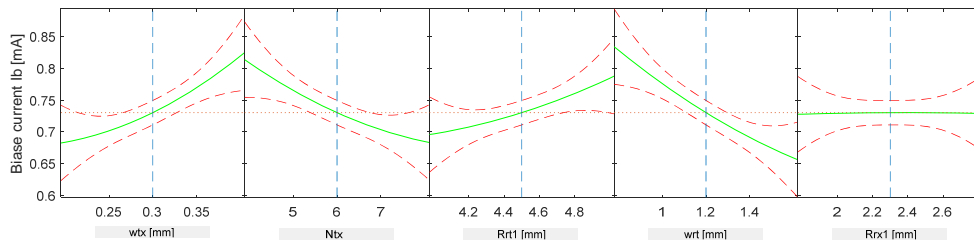
(a)
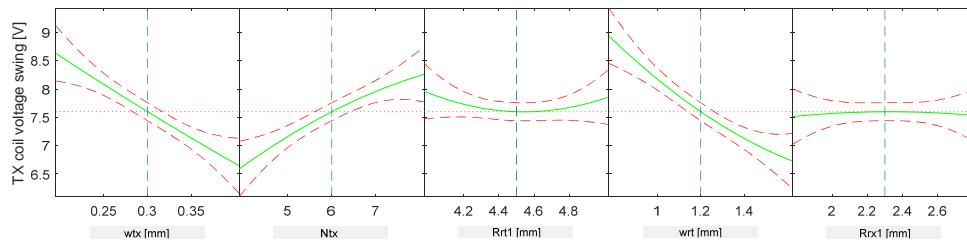
(b)
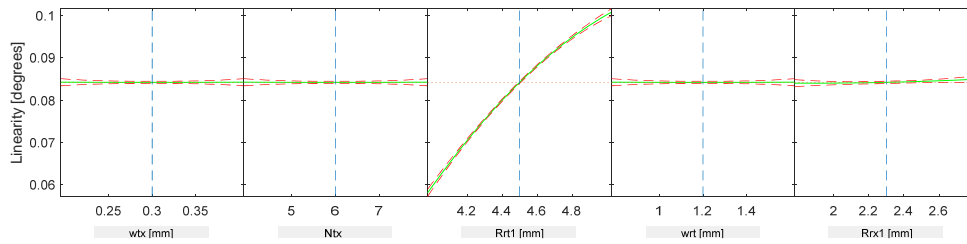
(c)

Figure 4-5 Response surface model of (a) Bias current, (b) TX voltage swing, (c) Linearity.

Based on the previous study, a three-level full factor experiment with regards to w_{tx}, N_{tx}, w_{rt} and R_{rt1} is designed. The experiment consists of total 81 variations. Table 4-3 presents the chosen factor levels. The coded factors represent a normalization of the factor levels such that the actual units and levels are not included in the analysis.

Table 4-3 Factors range

factor	Coded factor	Level		
		$z_i = -1$	$z_i = 0$	$z_i = 1$
w_{tx}	z_1	0.2mm	0.3mm	0.4mm
N_{tx}	z_2	7	8	9

w_{rt}	z_3	0.8mm	1.2mm	1.6mm
R_{rt1}	z_4	4mm	4.5mm	5mm

After quadratic regression analysis with data fitting, the resulting parametric models are presented in (7) and (8). The model shows a nonlinear relation between the factors and the performance since both the quadratic terms and interaction terms are significant.

$$v_1 = 19.0520 + \begin{pmatrix} z_1 & z_2 & z_3 & z_4 \end{pmatrix} \begin{pmatrix} -2.2712 \\ -1.9005 \\ -0.2496 \\ 0.7033 \end{pmatrix}$$
$$+ \begin{pmatrix} z_1 & z_2 & z_3 & z_4 \end{pmatrix} \begin{pmatrix} 0.2848 & -0.5897 & 0.0264 & 0.2131 \\ & -0.1916 & -0.0231 & 0.1008 \\ & & -0.0151 & -0.0119 \\ & & & 0.3846 \end{pmatrix} \begin{pmatrix} z_1 \\ z_2 \\ z_3 \\ z_4 \end{pmatrix}$$

(4-7)

$$I_b = 1.2925 + \begin{pmatrix} z_1 & z_2 & z_3 & z_4 \end{pmatrix} \begin{pmatrix} 0.1042 \\ -0.0875 \\ -0.0324 \\ 0.0699 \end{pmatrix}$$
$$+ \begin{pmatrix} z_1 & z_2 & z_3 & z_4 \end{pmatrix} \begin{pmatrix} 0.0412 & 0.0331 & -0.0031 & 0.0213 \\ & 0.0220 & 0.0025 & -0.003 \\ & & 0.0044 & -0.0019 \\ & & & 0.0244 \end{pmatrix} \begin{pmatrix} z_1 \\ z_2 \\ z_3 \\ z_4 \end{pmatrix}$$

(4-8)

From the simulation results, it is indicated that the linearity is insensitive to the design variables and it generally meets the requirement of the application. Therefore, the linearity is neglected in further optimizations. The optimization thus has two objectives, i.e. the bias current should be as small as possible and the transmitting coil swing voltage should be below a certain level, which is 20V for 5V power supply. The Pareto front of the two-objective optimization is presented in Fig. 4-6. The chosen optimum design is denoted by the red circle with the corresponding design parameters being:

$w_{tx} = 0.2mm,\ N_{tx} = 9, w_{rt} = 1.6mm, R_{rt1} = 4.5mm$.
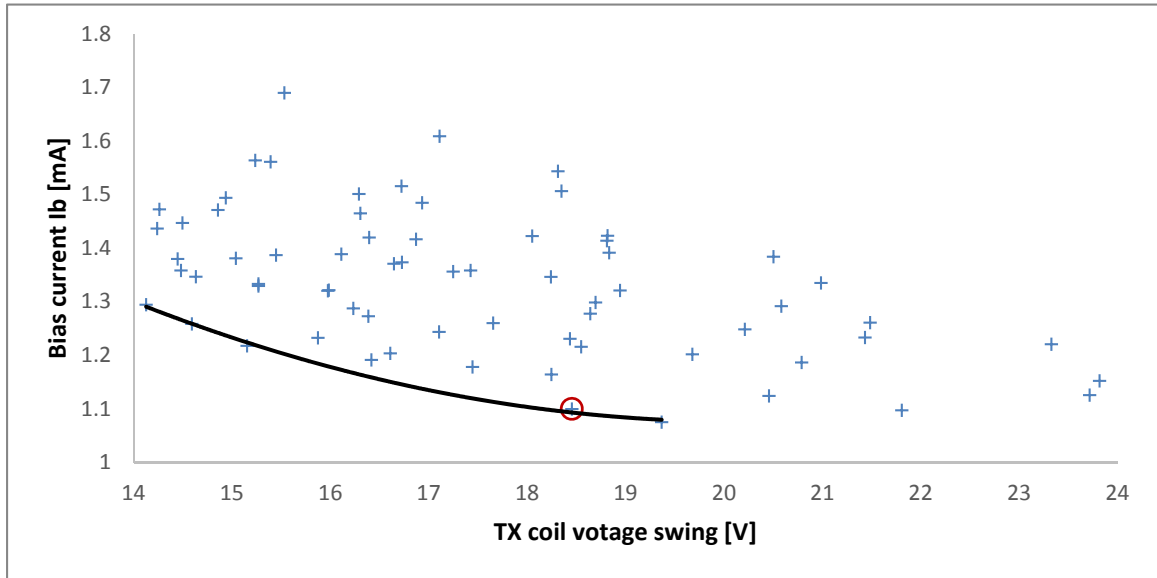
Figure 4-6 Pareto front of IAPS design

4.4   Design verification

To verify the optimization procedure, the design is also checked by FEM and circuit simulation in SPICE. The FEM is run in ANSYS HFSS, as shown in Fig 4-7(a). To save computation time, all coils are modeled as copper sheet with 35 μm thickness. A 60 mm x 60 mm x 60 mm air box with radiation boundary is modeled as the computation domain. The solution use first order basis function, its converge criteria is maximum delta energy being less than 0.01%.

In the circuit simulation, the capacitance of the capacitor takes the value of 252pF and the bias current takes the value of 1.1mA, which are the same as that adopted in the simulation model. The step of simulation is   The simulation results are shown in Table 4-4 for comparison. The excitation current and voltage agree very well with the prediction from our optimization model. The receiving signal is slightly lower than the prediction due to the simplification in the model, in which the major error source is the neglected parasitic capacitance of the transmitting coil.

(a)   (b)
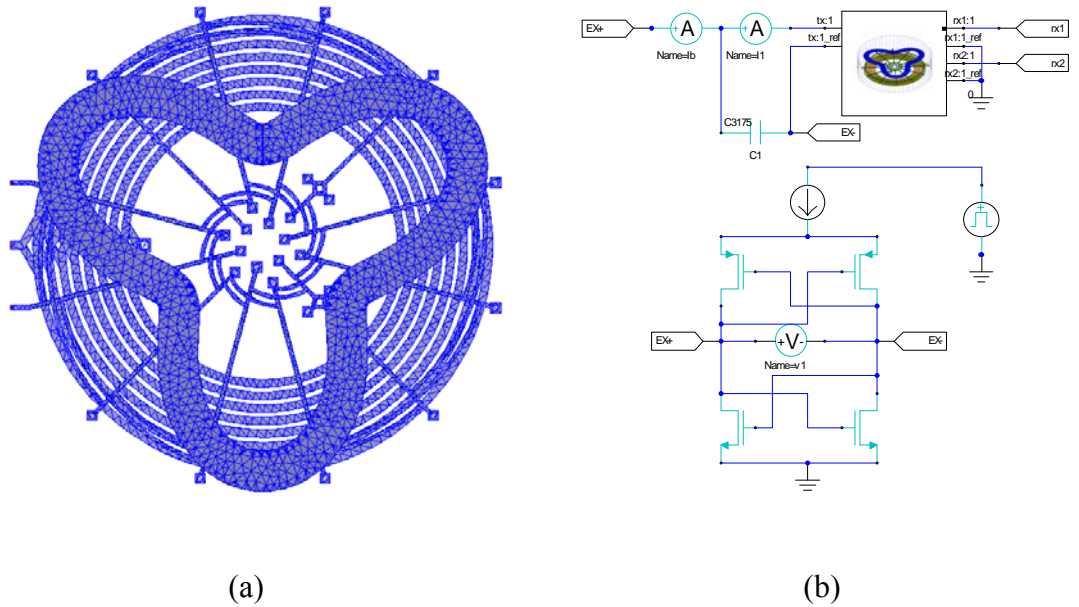
Figure 4-7 (A) ANSYS HFSS FEM model (b) ANSYS Designer SPICE model

Table 4-4 Simulation result comparison

	Model	SPICE
Operating frequency	4 MHz	4.025 MHz
Excitation current	116.9 mA	115.1 mA
Excitation voltage	18.45 V	18.09 V
Receiving signal	100.7 mV	95.5 mV

4.5   Conclusion

An optimization procedure of the IAPS is developed in this chapter. As an example, an outer diameter of 18 mm IAPS is optimized in this chapter by RSM. The transmitting coil voltage swing and bias current are the two objectives of the optimization. Design variables are first simulated using the model developed in chapter 2 and the Pareto front is derived from the simulation result. The optimal design is extracted from the Pareto front, which is

further verified by FEM and SPICE simulations. The optimization results agree very well with the FEM and circuit simulations, which validates the proposed optimization method.

Chapter 5

5 Micro-inductive Sensor

5.1 Introduction

Compared to other non-contact angular position sensor technology, such as magnetic sensors and optical sensors, IAPS has the advantage of low manufacturing cost and immunity to the DC stray magnetic field. The disadvantage of IAPS is its large size, which limits its application when the package space is tight. In this chapter, a miniaturized inductive angle position sensor is developed to solve this problem. It will reduce the size of the inductive position sensor down to the same level as magnetic sensor by using a micro-fabrication process.

This chapter is organized as follows. Section II describes the challenge of scaling down and a rotor design optimization to overcome this difficulty. Section III presents a model of the sensor electromagnetic structure. Section IV shows the microfabrication procedure. Finally, the experiment results are discussed in the last section.

5.2 Rotor design optimization

It is demonstrated in chapter 2 that an inductive position sensor determines the rotor position by detecting the magnetic field induced by the eddy current on the coupler. The signal strength of the inductive sensor follows Faraday's law:

$$V = - \int_{\Sigma} \frac{\partial B}{\partial t} \cdot dA \tag{5-1}$$

where Σ is the surface bounded by the sensing loop, and B is the magnetic flux density.

Equation 5-1 shows that when the sensor dimension is scaled down, the integration surface area is reduced, leading to a reduction in signal strength accordingly. The sensor needs to meet a certain signal/noise ratio to provide a sufficient resolution, however, the signal strength limits the minimal dimension of the sensor.

The signal can be enhanced by increasing the operating frequency, the integration area or the magnetic field strength. Among those methods, the operating frequency is limited by regulation and EMC requirement. The effective integration area can be multiplied by using multiple coil loops, which is feasible when higher resolution fabrication technology is adopted. However, too many loops of coil can introduce high parasitic capacitance, which not only limits the operating frequency but also introduces large output error. Therefore, the most promising method to increase the signal strength is to increase the magnetic field strength generated by the eddy current. Magnetic resonance coupling is widely used to improve the power transfer efficiency in various applications such as implantable electronics, which is a promising approach to increase the magnetic field strength.

(a)   (b)
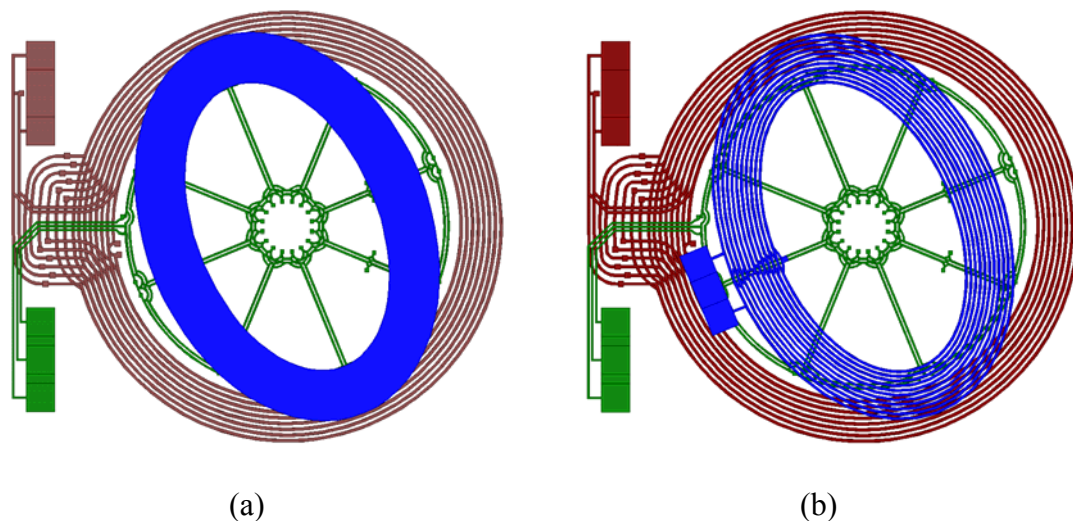
Figure 5-1(a) solid rotor FEA model; (b) coil rotor FEA model.

To find out the most efficient rotor design, 4 diffident rotor configurations are compared by numerical simulations. The electromagnetic field simulation is conducted in ANSYS/HFSS. The solution use first order basis function, its converge criteria is maximum delta energy being less than 0.01%. In all these 4 designs, the transmitting coil and the receiving coil designs are the same. The transmitting coil comprises 16 loops in two layers. In case (a) (solid rotor design), the rotor is a 20 μm thick copper sheet. Its shape is an 8.5 mm x 6 mm ellipse with a 6.5 mm x 4mm elliptic hole as shown in Fig. 5-1(a). In cases (b) – (d) coil rotor design the rotor consists of a 22 loops of copper coils in 2 layers, and the dimension of the ellipse is the same as case (a), with the cross section of the trace

being 50 μm x 20 μm, as shown in Fig. 5-1(b). In cases (a) and (b), the rotor coils are shorted. In cases (c) and (d), the rotors are connected with a capacitor C_2 in series. The tank capacitor C_1 and the rotor capacitor C_2 are tuned so that the oscillator can operate at 4 MHz frequency.

(a)

(b)

(c)

(d)
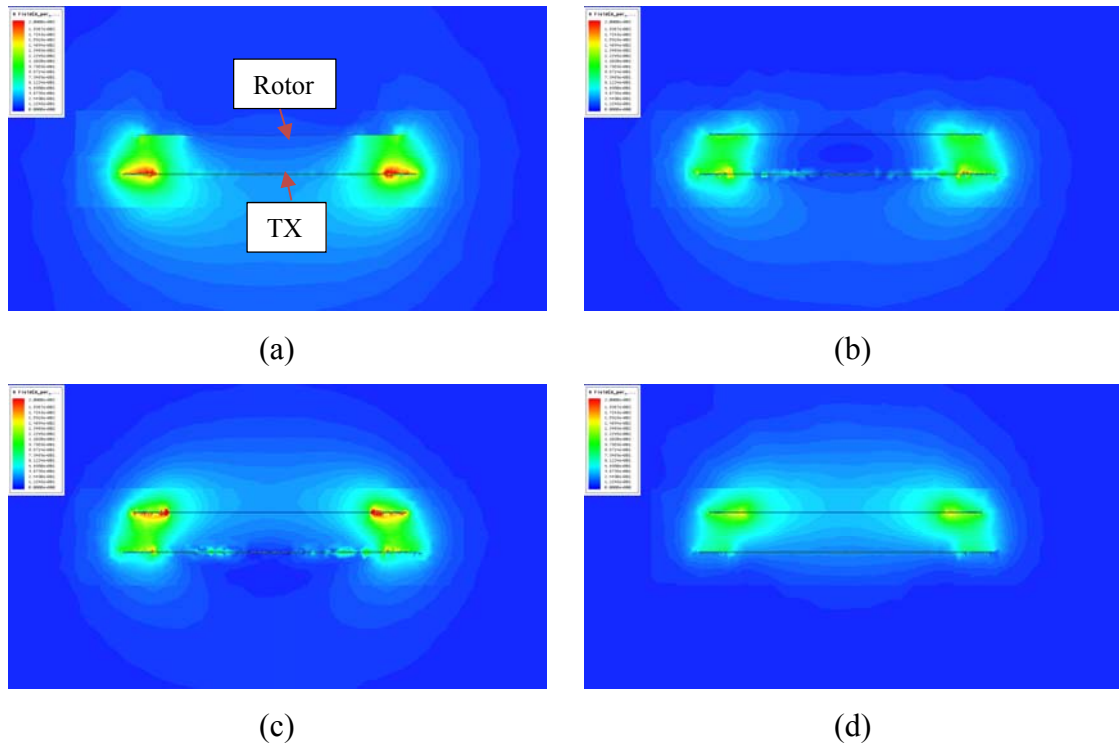
Figure 5-2 Magnetic field strength when TX coil is driven by 50mW 4Mhz AC power. (a) solid rotor, (b) shorted rotor coil, (c) resonance rotor coil in-phase mode, (d) resonance rotor coil out-of-phase mode.

In the electro-magnetic field simulation, all the transmitting coils are driven by a 50 mW 4 MHz AC power supply. The magnetic field distribution is shown in Fig. 5-2. In design (c) the eddy current is in the same phase as the excitation current; therefore, design (c) has the highest magnetic field strength at the rotor position. In the other 3 designs, the eddy current is in the opposite phase of the excitation current. Among those designs, design (d) has the lowest overall magnetic field strength.

(a)   (b)
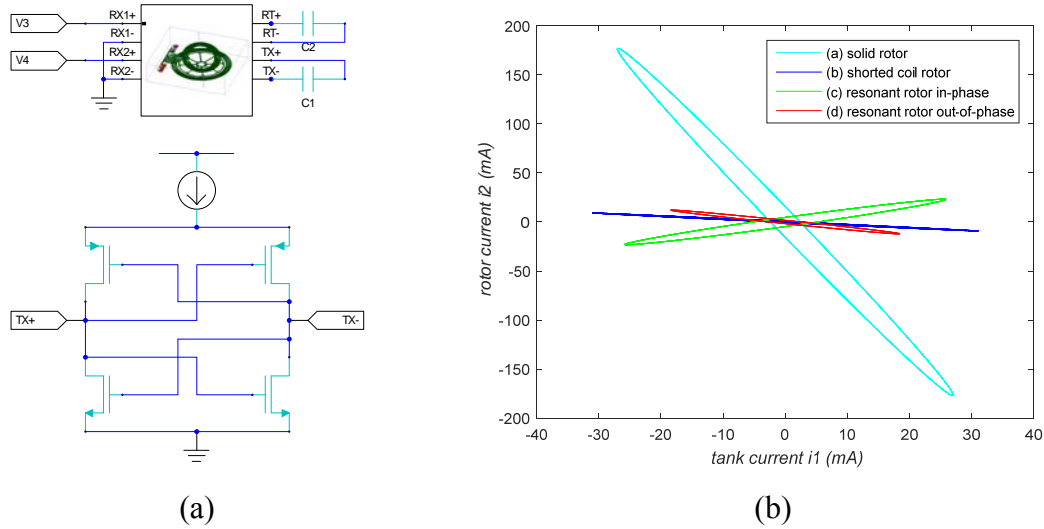
Figure 5-3 (a) simulation circuit; (b) tank current vs. rotor current.

Table 5-1 circuit simulation result of different rotor design

design	C_1 (pF)	C_2 (pF)	Freq (MHz)	i_1 (mA)	i_2 (mA)	$i_1 - i_2$ phase	v_1 (mV)	v_2 (mV)	$\sqrt{v_3{}^2 + v_4{}^2}$ (mV)
(a)	450	shorted	4.00	54.0	353.6	opposite	4.8	n/a	98.9
(b)	440	shorted	3.98	62.0	18.4	opposite	5.6	n/a	125.5
(c)	296.4	247	3.98	51.6	46.5	same	6.9	7.5	165.7
(d)	507	591	3.98	36.8	24.3	opposite	2.9	1.6	61.7

To further understand the signal strength difference of those 4 rotor designs, the FEA model is coupled into the circuit simulation in ANSYS/Designer. The simulation circuit model is demonstrated in Fig. 5-3(a), with the simulation result being listed in table 5-1. Circuit simulation shows that in design (c), the eddy current i_2 is in the same phase as the excitation current i_1, which is in agreement with the magnetic field simulation. Consequently, design (c) has the highest signal strength, and its tank voltage swing is also the highest because the induced voltage from the eddy current is added up. Design (d) has the lowest signal strength, and its tank voltage swing is also the lowest because the induced voltage from the eddy current is canceled out. The simulation results show that the coil rotor design (b) has 27% higher signal strength than the solid rotor, while the resonant coil

rotor design (c) has 67% higher signal strength than the solid rotor. Therefore, design (c) is chosen for the miniaturized position sensor.

5.3   Sensor design and modeling
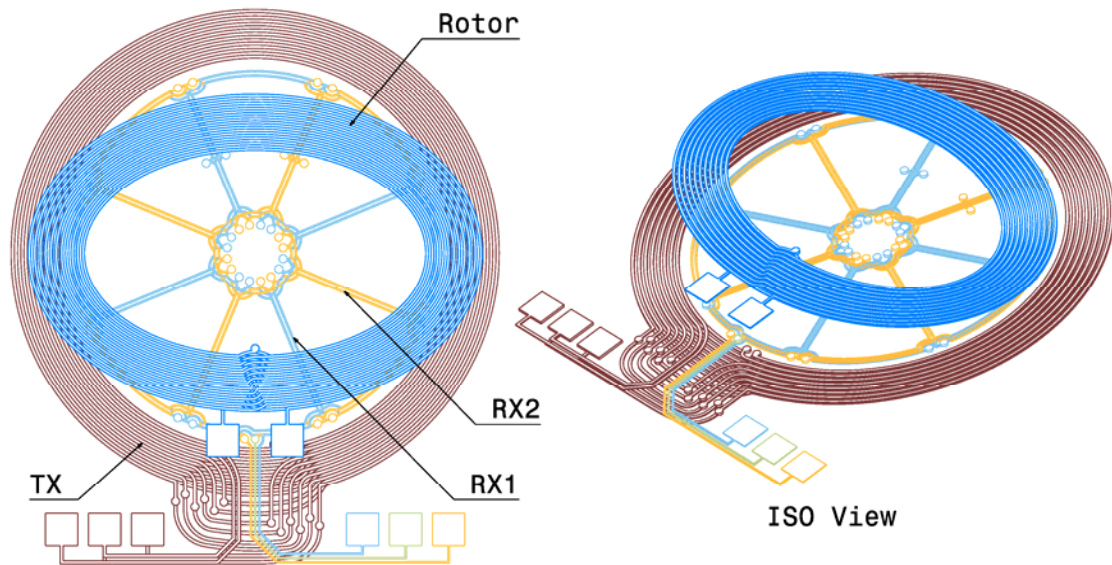
Figure 5-4 Sensor configurations

The micro-inductive position sensor was designed to be compatible with the circuitry of the PCB version. The stator comprises a transmitting coil TX and two receiving coils RX1 and RX2, while the rotor consists of multi-turns elliptic coils. The two receiving coils have the same shape but are offset from each other by 45 degrees. Each receiving coil consists of two clockwise wounded segments and two counter-clockwise segments. The operating frequency is set to 4 MHz. The skin depth of the copper at this frequency is 32.6 μm, in order to ensure the efficiency and quality of the fabrication. The transmitting coils are designed to be 50 μm wide and 20 μm thick, insulated by a 10 μm polyimide layer. The transmitting receiving coil is 40 μm wide and 20 μm thick to guarantee the fabrication quality. To enhance the signal strength, the coupler consists of 2 layers of 22 loops of oval-shaped micro-coil structure in total, and its cross section is the same as the transmitting coil.

The position sensor can be modeled as a LCR network coupled through mutual inductance, as shown in Figure 5-5. L_1, R_1, L_2 and R_2 are inductance and resistance of the transmitting and rotor coils, respectively. L_3 and L_4 are inductance of the receiving coils. Transmitting coil induces eddy current on the coupler through the mutual inductance M_{12}, and the eddy current further induces sensing signals v_3 and v_4 through the mutual inductance M_{23} and M_{24}. The transmitting coil Tx is driven by a differential oscillator, which can be modeled as a nonlinear resistor. The receiving coils Tx$_1$ and Tx$_2$ are designed in such way that the mutual inductance between the transmitting coil and the receiving coil, i.e., M_{13} and M_{14} is negligible, and thus the receiving signal all comes from the eddy current of the rotor coil. For complex geometry, there is no close form analytical solution for self-inductance and mutual inductance. The self-inductance L_1, L_2 and the mutual inductance M_{12}, M_{23} and M_{24} can be evaluated by the method developed in chapter 2 or the FEA method. These electrical properties are determined for an air gap of 1.2 mm and listed in Table 5.2.
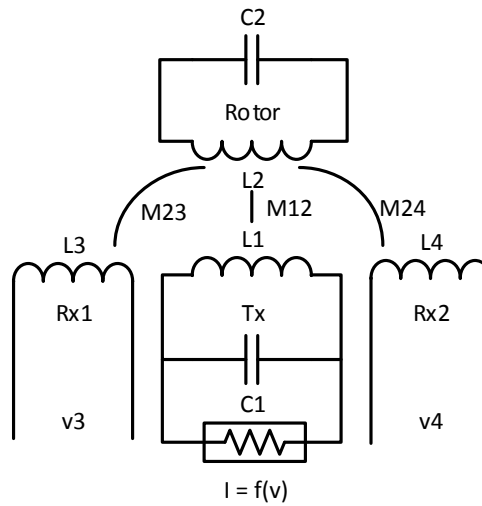
Figure 5-5 Micro-inductive sensor equivalent circuit

Table 5-2 Electrical properties of the coils for numerical simulation

Description	Name	Value	Unit
TX coil resistance	R_1	6.65	Ω
Rotor resistance	R_2	7.79	Ω
TX coil inductance	L_1	4.04	μH
Rotor inductance	L_2	4.88	μH
Mutual inductance at 0.8mm gap	M_{12}	1.72	μH
Mutual inductance at 1.2mm gap	M_{12}	1.45	μH

Since the sensing coil has high input impedance, the current passing through it is negligible. The relation between the current through each coil loop and the voltage across the coil loop can be expressed in the following differential equation system from Kirchhoff's Current Law (KCL) and Voltage law (KVL),

$$\begin{cases} L_1 \dfrac{di_1}{dt} + M_{12} \dfrac{di_2}{dt} = v_1 - i_1 R_1 \\ L_2 \dfrac{di_2}{dt} + M_{12} \dfrac{di_1}{dt} = v_2 - i_2 R_2 \\ C_1 \dfrac{dv_1}{dt} = S \tanh\left(\dfrac{G_n}{S} v_1\right) - i_1 \\ \quad C_2 \dfrac{dv_2}{dt} = -i_2 \end{cases} \qquad (5\text{-}2)$$

The corresponding SIMULINK model is demonstrated in Figure 5-6. The inputs of the model are electrical properties including the inductance, the mutual inductance, the resistance, the capacitance and the characteristics of the nonlinear resistor. The outputs of the model are the current and the voltage of the electromagnetic structure. Equation 5-2 looks similar to the equation 2-7. However, since the equation 2-7 has 3 DoF and the system always oscillates at one resonance frequency, while the equation 5-2 has 4 DoF, and the system could oscillate at any one of two resonance frequency. Thus, the behavior of the system is much more complicated than the simple rotor discussed in chapter 2.

To ensure that the sensor functions properly, sufficient eddy current needs to be induced in the rotor so that the signals on the receiving coils can detect are high enough. Figure 5-7(a) shows that when the transmitting coil is driven by the circuit with a 5 V power supply and a 5mA current sink, the eddy current remains at 110 mA with the air gap ranging from

0.8mm to 1.6 mm. Without the resonance capacitor C2, the eddy current is proportional to the coupling coefficient, which will drop from 19.2 mA to 15.5 mA. Figure 5-7(b) shows the receiving signal strength with regard to the air gap changes; for example, when the air gap increases from 0.8 mm to 1.6 mm, the signal of the resonance rotor drops by 27%, while the shorted rotor drops by 45%. The simulation results conclude that the resonance rotor can make eddy current less sensitive to the air gap variation, and enhance the sensing of signal strength. Therefore, this sensor can function over a wider air gap range.
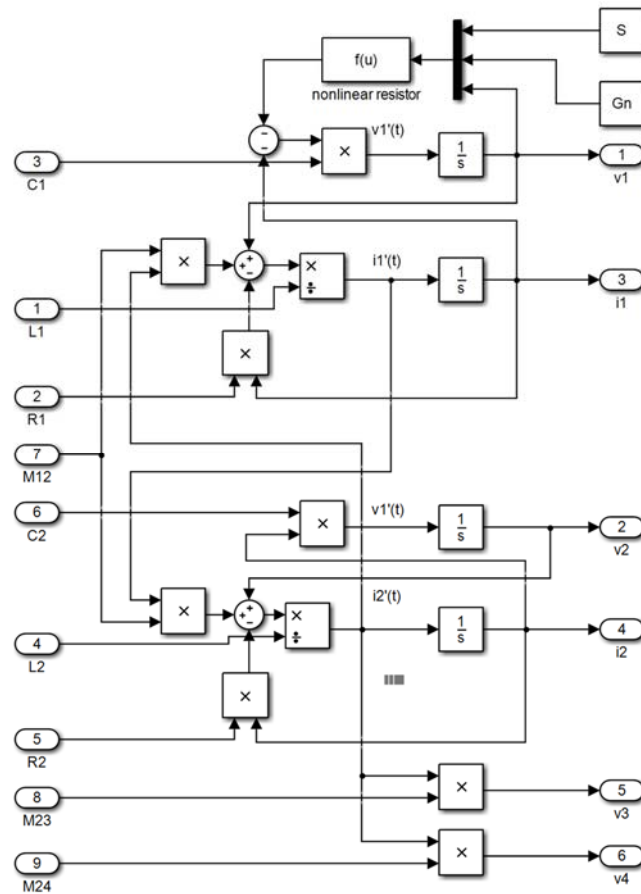
Figure 5-6 Simulink model of MIAPS
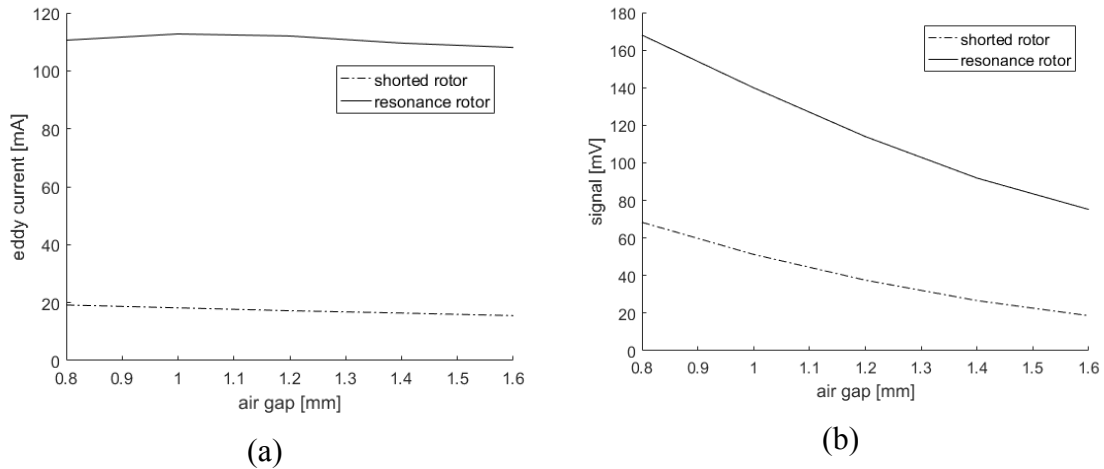
Figure 5-7 (a) eddy current; (b) receiving signal

5.4   Resonance mode of rotor

It should be noted that designs (c) and (d) in section 5.2 have exactly the same coil design, with the only difference between them being the capacitor value. A mismatched pair of capacitors can cause the eddy current to be the opposite phase of the excitation current, which cancels out the magnetic field strength and reduces the receiving signal strength. The simulation shows that the deviations in coil separation and alignment greatly affect the gain of the coupling, resulting in significant variations in the sensor receiving signal. In particular, frequency splitting occurs when the coils are driven in the over-coupled regime [51]. Under these conditions, the link gain shows two peaks at different frequencies, which deviate from the tuned resonant frequency.

To ensure that the sensor always operates optimally, the condition of the resonance mode needs to be understood. A small signal linear analysis is conducted to investigate at which mode the sensor will operate. By using the same approximation as equation (2-27), Equation (5-2) can be linearized in the matrix form as:
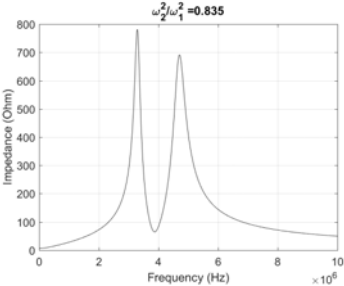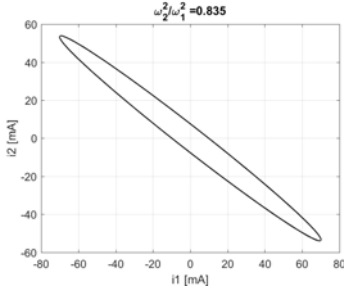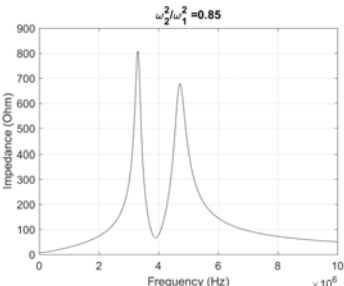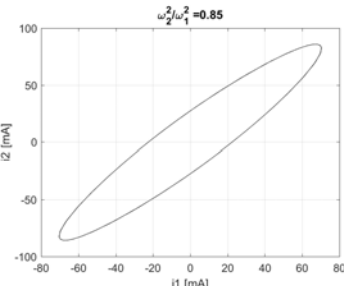
$$\begin{pmatrix} \dfrac{di_1}{dt} \\ \dfrac{di_2}{dt} \\ \dfrac{dv_1}{dt} \\ \dfrac{dv_2}{dt} \end{pmatrix} = \begin{pmatrix} L_1 & M_{12} & 0 & 0 \\ M_{12} & L_2 & 0 & 0 \\ 0 & 0 & C_1 & 0 \\ 0 & 0 & 0 & C_2 \end{pmatrix}^{-1} \begin{pmatrix} -R_1 & 0 & 1 & 0 \\ 0 & -R_2 & 0 & 1 \\ -1 & 0 & G_n & 0 \\ 0 & -1 & 0 & 0 \end{pmatrix} \begin{pmatrix} i_1 \\ i_2 \\ v_1 \\ v_2 \end{pmatrix} \tag{5-3}$$

Equation (5-3) is a 1st order linear differential equation system, its solution depends on the eigenvalues of the coefficient matrix:

$$A = \begin{pmatrix} L_1 & M_{12} & 0 & 0 \\ M_{12} & L_2 & 0 & 0 \\ 0 & 0 & C_1 & 0 \\ 0 & 0 & 0 & C_2 \end{pmatrix}^{-1} \begin{pmatrix} -R_1 & 0 & 1 & 0 \\ 0 & -R_2 & 0 & 1 \\ -1 & 0 & G_n & 0 \\ 0 & -1 & 0 & 0 \end{pmatrix} \tag{5-4}$$

Table 5-3 Impedance and phase portrait of different configuration

Configuration	Impedance	Phase portrait
$gap = 1.2mm$ $\dfrac{L_1 C_1}{L_2 C_2} = 0.835$ $\lambda_{1,2} = (0.0389 \pm 2.9097i) \times 10^7$ $\lambda_{3,4} = (0.0348 \pm 2.0843i) \times 10^7$ Oscillate at 2.9097e7 rad/s opposite phase		
$gap = 1.2mm$ $\dfrac{L_1 C_1}{L_2 C_2} = 0.85$ $\lambda_{1,2} = (0.0354 \pm 2.9197i) \times 10^7$ $\lambda_{3,4} = (0.0383 \pm 2.0957i) \times 10^7$ Oscillate at 2.0957e7 rad/s in phase		

$gap = 1.2mm$

$$\frac{L_1 C_1}{L_2 C_2} = 1$$

$\lambda_{1,2} = (0.0710 \pm 2.1888i) \times 10^7$

$\lambda_{3,4} = (0.0027 \pm 3.0313i) \times 10^7$

Oscillate at 2.1888e7 rad/s in phase
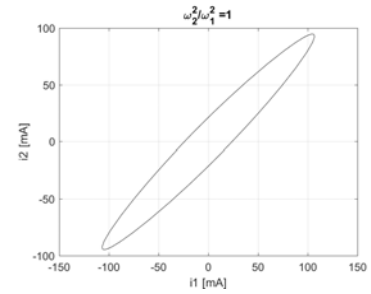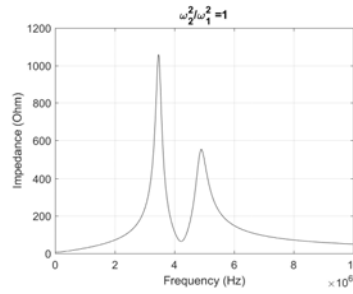
$gap = 0.8mm$

$$\frac{L_1 C_1}{L_2 C_2} = 0.77$$

$\lambda_{1,2} = (0.0351 \pm 3.0067i) \times 10^7$

$\lambda_{3,4} = (0.0294 \pm 1.9859i) \times 10^7$

Oscillate at 3.0067e7 rad/s opposite phase
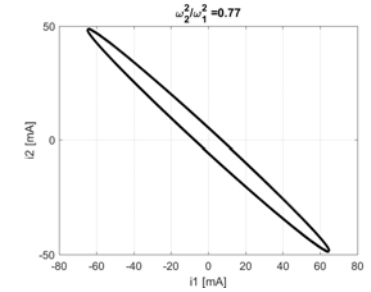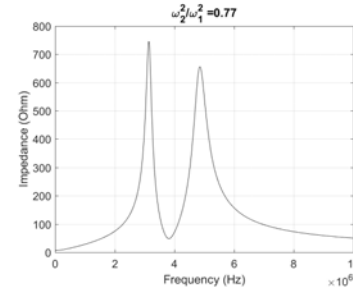
$gap = 0.8mm$

$$\frac{L_1 C_1}{L_2 C_2} = 0.78$$

$\lambda_{1,2} = (0.0330 \pm 3.0136i) \times 10^7$

$\lambda_{3,4} = (0.0314 \pm 1.9942i) \times 10^7$

Oscillate at 1.9942e7 rad/s in phase
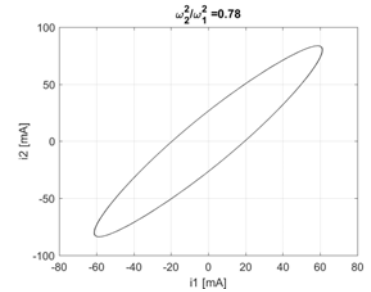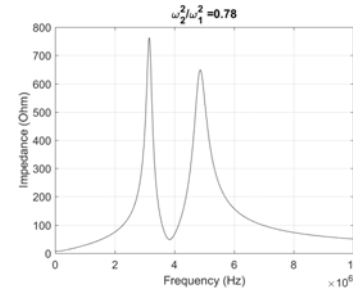
$gap = 0.8mm$

$$\frac{L_1 C_1}{L_2 C_2} = 1$$

$\lambda_{1,2} = (0.0729 \pm 2.1371i) \times 10^7$

$\lambda_{3,4} = (-0.0084 \pm 3.1827i) \times 10^7$

Oscillate at 2.1371 rad/s in phase
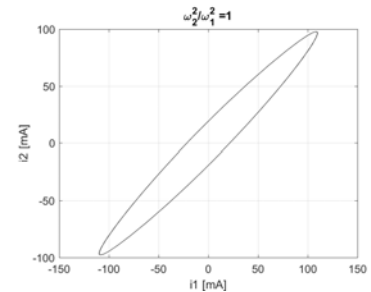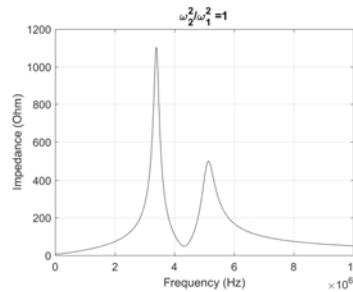
The operation mode is analyzed numerically for 0.8mm and 1.2mm air gap, as illusrated in Table 5-3. It can be seen that the system tends to oscillate at the mode where the real part of the eigenvalue is larger. The system always oscillates in the same phase when $\frac{L_1 C_1}{L_2 C_2} = 1$, and there is no correlation between the impedance and the oscillation mode. At 1.2mm air gap, the system oscillates in the opposite phase when $\frac{L_1 C_1}{L_2 C_2} \leq 0.835$, while at 0.8mm air gap,

the system oscillates in the opposite phase when $\frac{L_1 C_1}{L_2 C_2} \leq 0.77$. It should be noted that the coupling coefficient is greater at a smaller air gap, and the system can oscillate in phase with more tolerance of the tank frequency mismatch. Based on this finding, the system operation region is illustrated in Figure 5-7. For sensor applications, a high coupling coefficient can ensure a more robust operation and allow larger component variations.
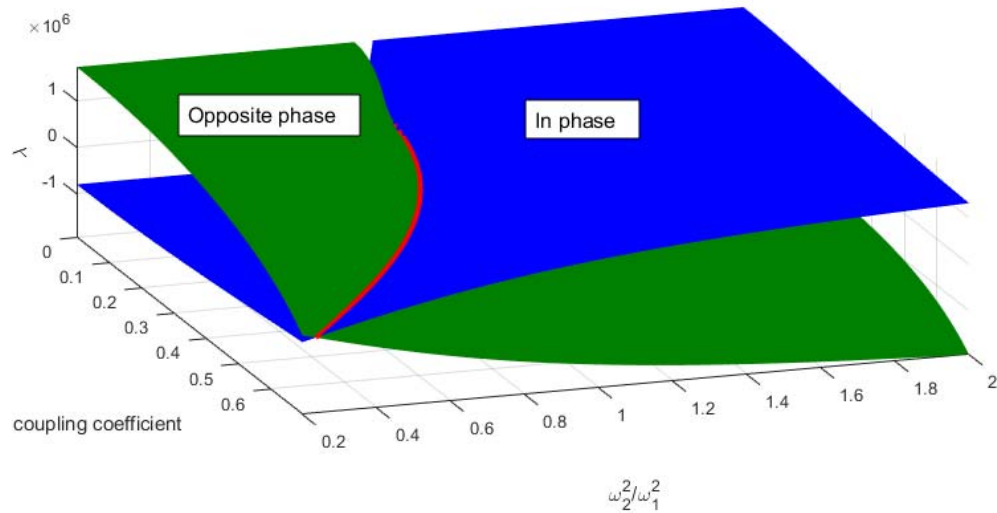
Figure 5-8 operation region

5.5   Fabrication

The cross-section view of the device is shown in Figure 5-9. There are three layers from the bottom to the top: the first layer of copper coil, an insulating layer with via holes that insulates the first and second layer copper, and the second copper layer.
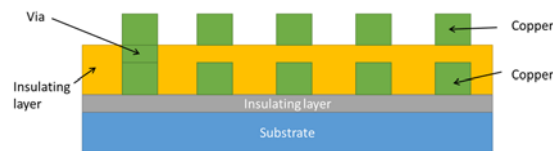
Figure 5-9 Device cross section

The 20μm thick copper coil is fabricated by electroplating, while polyimide is used to make the insulation layer. The following steps explain the micro fabrication process.

5.5.1   Preparation of substrate

Sensor is built on a 500 μm silicon substrate with a 2 μm-thick silicon dioxide layer. The wafer is immersed in Nanostrip® solution for 3 minutes to remove the organic contaminations, and then is rinsed with de-ionized water.

5.5.2   Seeding layer sputtering

The seeding layer for electroplating is prepared by sputtering. A 50 nm-thick Titanium adhesion layer was RF sputtered in Edwards Auto500 Sputter Deposition System with a power of 100W for 15 minutes. Then a 300 nm-thick copper was sputtered using DC sputtering with a power of 150W for 15 minutes. The deposition is under the vacuum condition of the base pressure of about 5×10^{-5} bar.

5.5.3   Micro-mold photolithography

A 15μm thick of positive photoresist AZ9260 is spin-coated at 1000 rpm. The coating is soft-baked on a hotplate. To avoid bubble and delamination of the thick coating, the temperature of the hotplate is ramped from the room temperature to 110°C in 10 minutes and then is held at 110°C for 3 minutes. The photoresist polymer is cross-linked by exposing to UV light with Karl SussMA6 mask aligner. After exposure, a micro-mold is developed in AZ400K, followed by a cleaning process using Oxygen plasma RIE.

5.5.4   First micro-coil layer fabrication

The micro-coil is fabricated by electroplating in a commercial equipment IKO Classic electroplating system. The recipe of the plating bath is: 225 g/L $CuSO_4$, 50 g/L H_2SO_4, 50 ppm HCl, 8 ml/L Brightener, and 8 ml/L Carrier. At 53 mA/cm^2 current density, a 25μm thick copper layer is plated in two hours. Although the copper layer is higher than the micro-mold, the excessive part formed a mushroom shape over the micro-mold and no short circuit was found. After electroplating the micro-mold is stripped off in Acetone, the copper seeding layer is etched off by the Transene APS-100 copper etchant, and then the Ti layer is etched by the Transene TFTN Titanium etchant.

5.5.5   Insulating layer fabrication

A 30μm thick negative tone Polyimide HD4100 is deposited between the first and the second copper coils as an insulating layer. To avoid the block of the first layer copper coil, Polyimide is initially spread over all patterned copper coil, and then is ramped to spin speed of 1500 rpm at an acceleration of 500 rpm/s and held for 50 seconds. The sample is soft-baked on a hotplate at 90°C for 90 seconds and then ramped to 110°C and held for another 90 seconds. The via holes which connect the two copper layers are patterned on the Polyimide layer by UV exposure of 300 mJ/cm2 dose using a mask aligner. 3 minutes post exposure bake at 100 ºC is performed to increase the adhesion and selectively crosslink the exposed parts of Polyimide. The sample is developed in PA-401D for 10 minutes and then is rinsed in PA-400R. Afterwards, the sample is cleaned by Oxygen plasma RIE, followed by a curing at 250 ºC for 20 minutes to complete the imidization process and remove the residual solvents and photoresist.

5.5.6   Second micro-coil layer fabrication

Right before the fabrication of the second micro-coil layer, the sample is etched by 10% Sulfuric acid to clean the CuO layer built up during the process. The same Ti/Cu bi-layer structure is used for the second seeding layer. Ti layer is increased from 50 nm to120 nm to compensate for the roughness of the RIE surface. The copper layer remained 300 nm thick. The second micro-coil layer is fabricated by the same procedure as the first one. Lastly, AZ9260 photoresist is spun on the wafer as a protecting layer.

The whole process could be summarized below:

Step 1. The Silicon substrate with SiO2 layer is thoroughly clear

Step 2. Cu/Ti seed layer is deposited by sputtering.

Step 3. Spin coat AZ9260 photoresist.

Step 4. Expose and develop.

Step 5. Electroplate copper

Step 6. Strip photoresist.

Step 7. Remove seed layer by wet etch.

Step 8. Spin coat HD4100 negative tone polyimide.
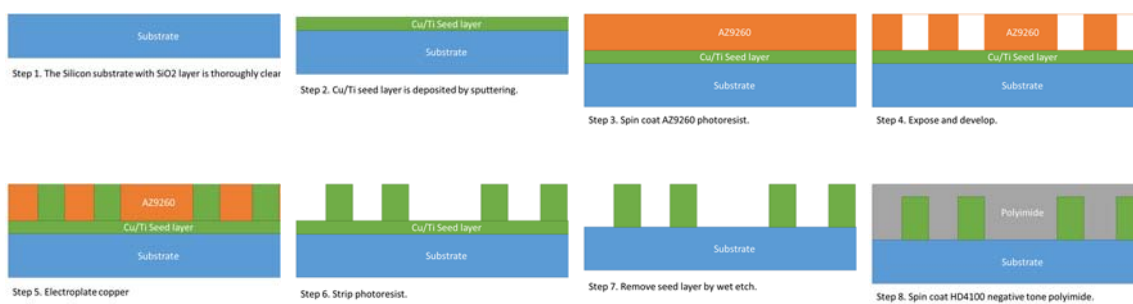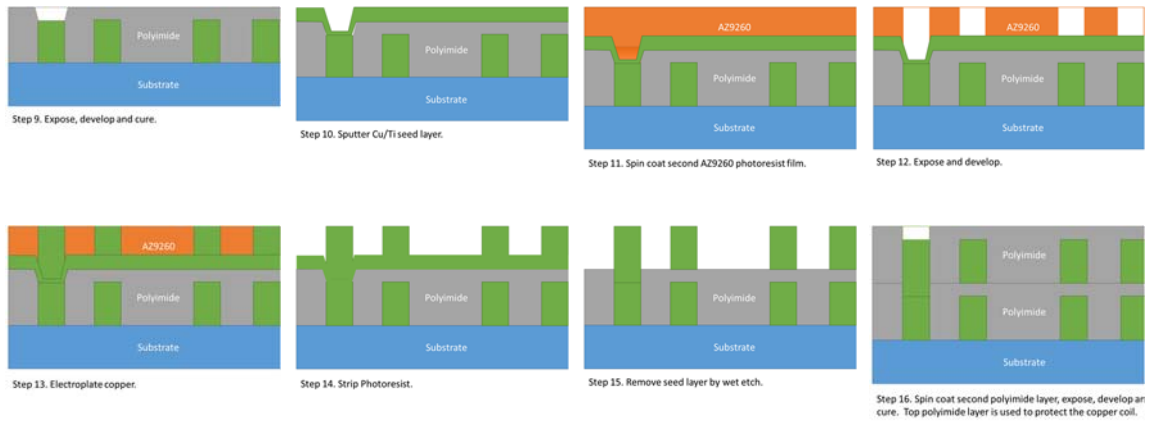
Figure 5-10 micro coil fabrication process

5.6   Experiment and discussion
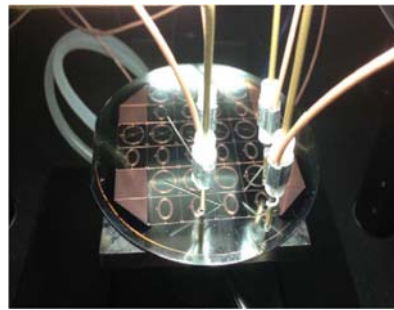
Figure 5-11 probe station for device characterization

The DC resistance and the inductance of the sample on the wafer are measured to pick up the good components through screening on probe station (Figure 5-11) with an LCR meter (Gwinstek LCR-821) at 200 KHz. The screened good diced sample is further measured by an Agilent 4294A impedance analyzer to check its AC resistance and inductance. It is found that the measured inductance matches well with the theoretical prediction, as shown in Table 5-4 and Figure 5-12. The measured resistance is higher than the theoretical one, which is due to the fact that the resistivity of the electroplated copper is higher than that of the bulk copper.

Table 5-4 DC impedance

	Average of measurement		FEA	
	Inductance	Resistance	Inductance	Resistance

| Tx coil | 3.21uH | 6.42 Ohm | 3.93uH | 6.27Ohm |
| Rotor coil | 4.92uH | 8.09 Ohm | 4.74uH | 7.38Ohm |
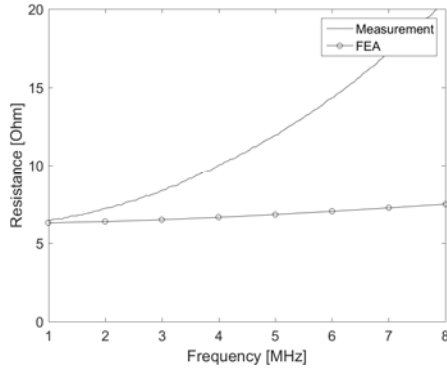
<center>(a)</center>
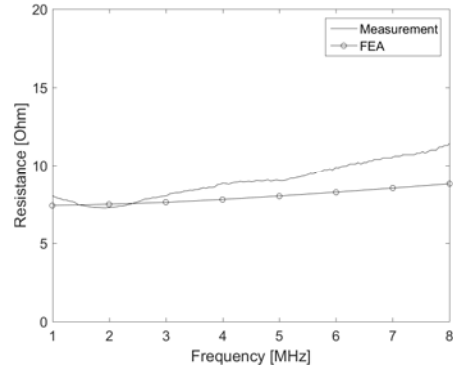
<center>(b)</center>
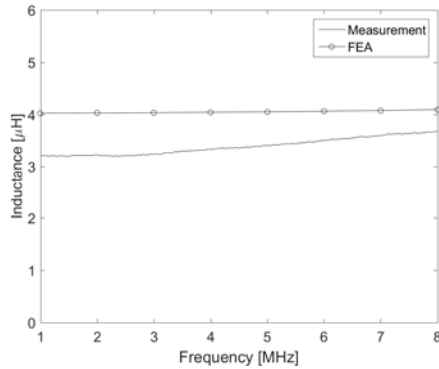
<center>(c)</center>
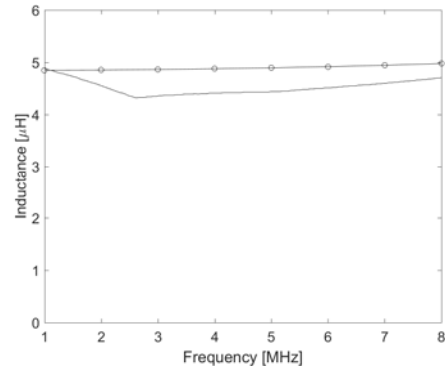
<center>(d)</center>

Figure 5-12 (a) Tx coil AC resistance; (b) Rotor coil AC resistance; (c) Tx coil AC inductance; (d) Rotor coil AC inductance.

5.7   Sensor assembly test

The micro-coil device is wire-bonded to a test printed circuit board (PCB) with 35µm gold wires for further testing, as shown in Figure 5-13. In the test board an ASIC designed for a regular PCB is used to drive the micro-coil.

(a)

(b)

(c)
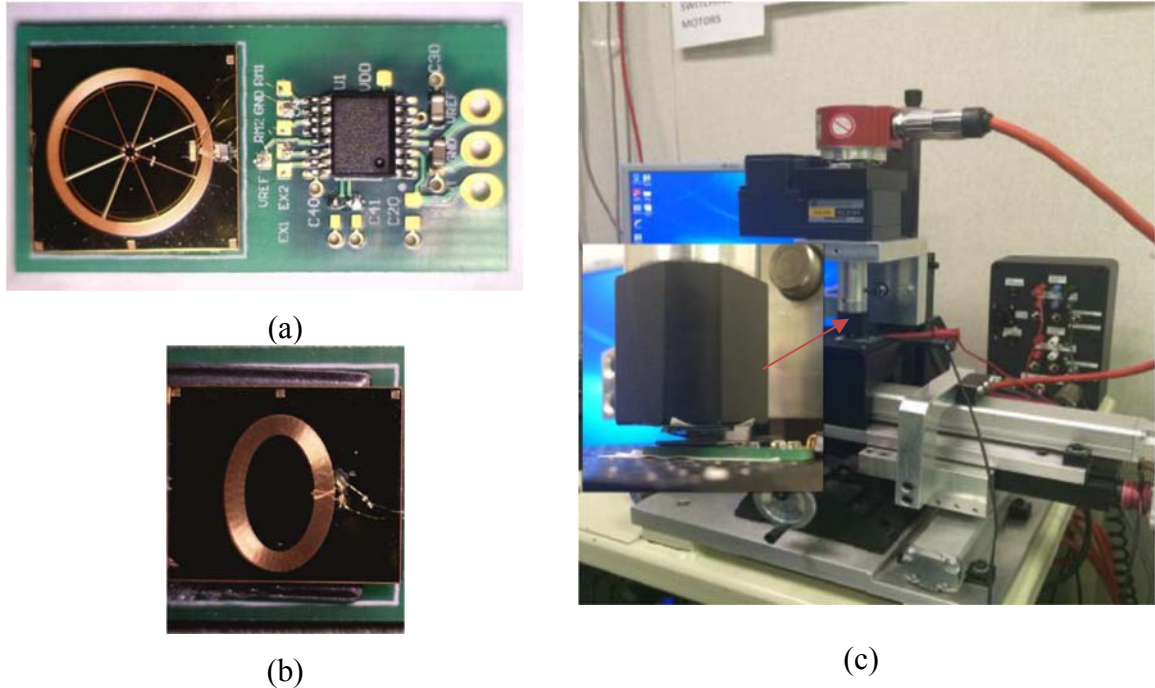
Figure 5-13 (a) Sensor assembly; (b) Rotor; (c) Test set up

(a)

(b)
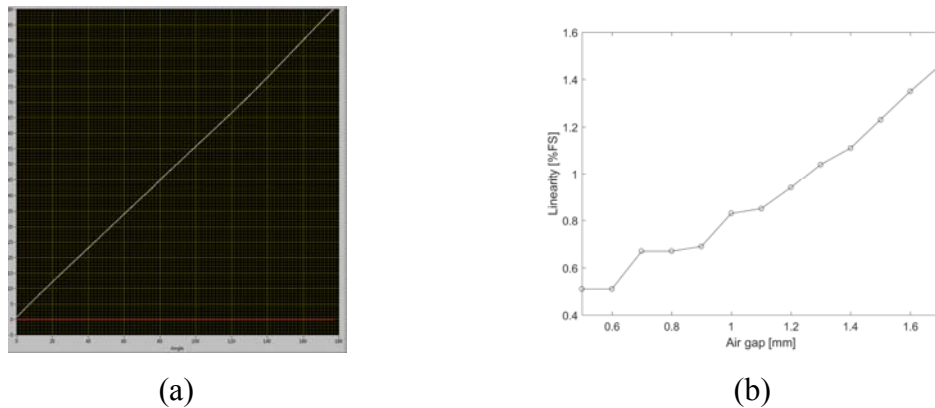
Figure 5-14 (a) Sensor output transfer function; (b) Sensor linearity at different air gap.

Despite the much smaller dimensions, the sensor functions very well when the air gap ranges from 0.5mm to 1.7mm. The sensor linearity error is less than 1.5% of the full scale, as demonstrated in Figure 5-13(b). It is thus concluded that this sensor can meet the requirements of most automotive applications in terms of accuracy.

5.8   Conclusion and future work

In this chapter we first investigate the scale-down effect of inductive position sensor. A scaled-down sensor has low signal strength due to the low Q factor and small area. To compensate for the weak signal, a resonant rotor is proposed. The design is first proved by numerical simulation using the model developed in chapter 2. To verify the micro-inductive position sensor concept, a prototype by microfabrication is then developed. The inductive position sensor can be scaled down to 8 mm diameter using the micro mold and electroplating technique, which is the same size as a magnetic one. The sensor can still have the same signal strength level as an inductive sensor based on the PCB technology and it functions normally up to 1.6 mm air gap. The sensor prototype can maintain reasonable accuracy over a wide air gap range.

To commercialize this design, the system in package design is suggested, as demonstrated in Figure 5-15. In this design, the micro coil is fabricated on a ferrite substrate, which not only reduces cost compared to silicon, but also enhances signal strength and provides a magnetic shield for the ASIC and circuitry.

(a)   (b)
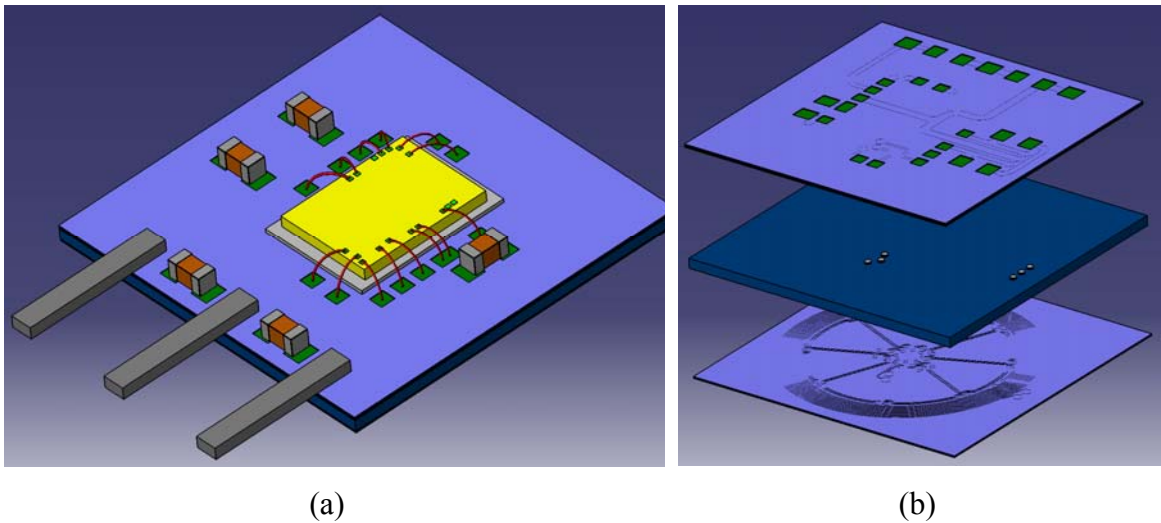
Figure 5-15 (a) System in package design; (b) explosive view of substrate.

Chapter 6

6 Steering Torque Sensor

6.1 Introduction

6.1.1 Steering torque sensor for electric power steering

The electric power steering (EPS) system is gradually replacing the traditional hydraulic power steering (HPS) system in passenger vehicles to improve fuel efficiency and safety and reduce environment impact[52]. In EPS, the amount of steering effort can be significantly relieved when an electric motor applies an appropriate assistant torque in the same direction. The main merit of EPS over HPS is its improved fuel efficiency. HPS accounts for 3-5% in the energy consumption of a car [52], compensating the flow loss and mechanical loss of the hydraulic system, while the EPS system only consumes electrical energy when mechanical steering is demanded. Meanwhile, EPS also has a more compact package and is more environmentally friendly than HPS since it does not require the hydraulic components such as pump, hose and hydraulic fluid like HPS. Consequently, EPS saves space and causes no environmental hazard by simplifying the system to an electric motor, a torque sensor and an Electronic Control Unit (ECU).
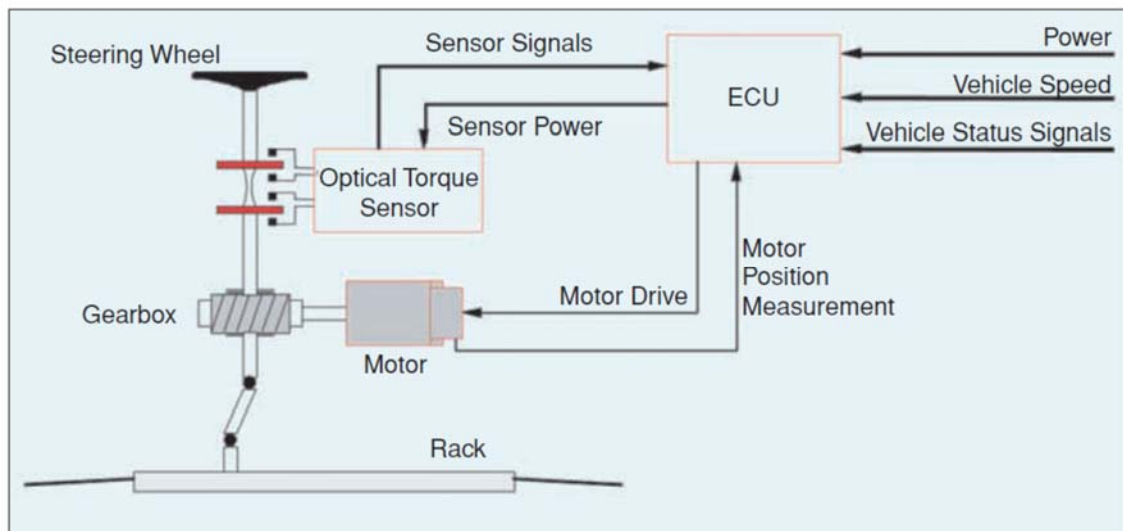
Figure 6-1 EPAS schematic arrangement.

A typical EPS system consists of four parts: steering mechanism, torque sensor, assist motor and controller, as illustrated in Fig. 6-1[53]. When the driver turns the steering wheel, the torque sensor detects the column torque. The ECU computes the motor current demand by using an assist torque map table, and then regulates the motor current accordingly.

EPS system is a safety critical system [54], which requires a reliable and accurate torque sensor as its input. The main function of the steering torque sensor is to precisely measure the driver steering torque demand with high resolution and high speed. To meet such requirement, various torque sensing technologies have been developed by exploiting the structure response to the applied torque. When a torque is applied to a shaft, it results in the development of stress and torsion of the shaft, and the stress modifies some of the device characteristics. For example, the strain affects the resistance of conductive and semiconductor materials, and the magnetization of ferromagnetic materials. In general, torque sensors can be classified into two families based on what response parameter is being measured [55]. The devices of the first family measure the device characteristic change induced by the applied torque, while the devices of the second family measure small angles or small displacements resulting from the torsional motion.

6.1.2   Devices based on material properties changes

The first family of torque sensor measures the property change due to the deformation of the material. Traditionally, strain gauge is an important commercialized device under this category. The applied torque is measured through the resistance change in the securely attached gauge material. A specially designed gauge is positioned on the part to measure the strain components [56], and the strain measurement is then processed by the electronic unit to get the final torque signal. In the rotating shaft applications, the sensor performance is sensitive to the technique of gluing gauges directly on the shaft. Solutions like press-fitting/welding show good results [57] but are heavy in their implementation. In addition, wireless communication between the strain gauges and the receiver has other technical difficulties such as the reliability and channel interference issue. Therefore, strain gauges are not used for automotive torque sensor application because of these difficulties.

Another family of torque sensor is based on the change in magnetic properties of the shaft itself. The main component of such torque sensor is the magnetic circuit, consisting of a rotating shaft and a set of stationary coils. The stress induced by the applied torque will change the magnetic permeability of a steel shaft, which means the inductance of the coil will change whenever the applied torque varies [58]. Those sensors are noncontact and can have a high sensitivity with the appropriate arrangement of the cores [59]. However, such sensors are usually heavy because of the cores and coils surrounding the rotating shaft, and therefore are not easily implemented for automotive application. Miniaturization of cores and flat coil designs for torque sensors with sufficient sensitivity have been reported in the literature [60, 61]. One problem with this family of sensors is the hysteresis of the sensor's output signal, which is caused by the hysteresis of the shaft material. Eddy currents in the metal shaft also limit their dynamic performance.

Magnetostrictive amorphous materials have been attracting great interest in the torque sensor application in recent years. One design in the literature is to use Chevron shaped ribbons of (Fe–Si–B) amorphous material glued directly on the shaft [62], where a solenoidal coil enclosing the shaft, energized by an AC current, provides magnetic excitation. In order to avoid adhesion problems, a low pressure plasma spray deposition technique is used to deposit the magnetostrictive material (Fe–Ni–Cr) layer on the shaft [61]. In some other designs, the magnetostrictive material is permanently magnetized to eliminate the coil, in which the magnetic field is measured by Hall probes over the ring ends.

6.1.3   Devices based on torsion angle changes

This type of device measures the relative angle between the two ends of a compliant torsion bar linking the input and output shafts. The torsion bar size must be designed properly to ensure both safety and sensitivity at the same time. One method is to measure the angular position of the two ends of the torsion bar separately, which gives the torsion angle by the subtraction of the two positon angles. Thus, the angular position sensors have to be very precise in order to accurately measure the torque, as the error is the summation of two angular position signals. Another disadvantage of the use of two high precision position sensors is that the bandwidth of the sensors must be very high when the device rotates at

high speed. On the other hand, the benefit of such design is that it can be easily integrated in the existing mechanical structures of the HPS.

Based on the relative angle measurement method, this family of torque sensors can be further classified as optical, capacitive, magnetic and inductive [63]. Numerous optical methods have been developed to measure torsion angle. Hazelden [64] proposed a method to measure the relative angular movement between the ends of a torsional shaft. Two rotating discs are fitted to the shaft, and each disc has a pattern of slots forming two concentric tracks of alternating transparent and opaque zones. One track of the slots of the two disks is in phase, while the other track of the slots is 180º out of phase. The torque is determined by measuring the amount of light transmitted by the varying overlap of the two discs. The degree of overlap between the slots on the two discs varies according to the amount of twist applied to the torsional bar. Ebi et al. [55] proposed an integrated optical non-contact torque measurement microsystem consisting of a glass integrated optical interferometer chip. In this system, ball lenses are used for collimation of measurement beams onto reflectors embedded in the shaft. A moire fringe method [65] has been validated under laboratory setting and shows high resolution. This method develops a series of concentric circular fringes using two superimposed circular gratings. These fringes move radially by the relative angular displacement of gratings. Modifications of speckle patterns [66, 67] also show good results. In general, the optical torque sensors provide good quality and high accuracy, but they are costly and difficult to package and integrate due to their fragile optical components and the requirement of clean environment, which makes it difficult to be adopted in automotive applications.

The capacitive torque sensor is composed of two capacitive displacement sensors in order to measure the twist angle [68]. Differential capacitive sensor for measuring the relative angle [69] is noncontact, robust and compact. It has two rotatable electrodes placed between two sensor plates. The relative angle between the two rotors and the absolute positions of the rotor blades are calculated from the measurement of the capacitive coupling between different transmitting stator segments and a single receiving electrode. The drawback of this type of torque sensor lies in its high sensitivity to radial and axial displacements and high cost.

The torsional angle can also be measured magnetically [70, 71]. With this working principle, the twist angle between two rotating shafts, which are linked by a torsional bar [72], modulates the magnetic circuit. The shafts are subjected to a magnetic field. The applied torque introduces a change to the magnetic field, which can be measured by magnetic sensors such as the Hall sensor or AMR sensor. The magnetic torque sensors developed by Moving Magnet Technologies (MMT) are widely used in the current automotive market.

Inductive measurement of the torsional angle is gaining popularity [12]. This type of sensor consists of two electrically isolated sensors that can function independently, which separately measures both input shaft and output shaft angles. The ECU then calculates the difference between the angles and multiplies it by the torsional stiffness to get the actual torque value. Besides the common benefits of inductive sensor such as low cost and robustness, the hysteresis of this method is low compared to direct torsion angle measurement sensors because the principle itself structurally does not include mechanical hysteresis. Secondly, common mode noises such as temperature or vibration effects are automatically canceled during difference calculation.

In spite of these benefits, since inductive torque sensor comprises two inductive sensors in a compact space, the two angle sensor could interfere with each other. The receiving signal of two angle sensor can cross-talk to each other, i.e. sensor A not only receives the signal from its own rotor, but also receives the signal from the rotor of sensor B. Such cross-talk can introduce significant error if the sensor is not carefully design. Furthermore, since the two oscillators are inductively coupled together, if the resonance frequency is close but not identical, they can produce beating and disrupt sensor function. In this chapter we first understand this problem via modeling and numerical simulation, and then validate our existing design through the experiments.

6.2   Design and parameters

The inductive steering torque sensor can be modeled as two-stage transformer networks, as shown in Figure 6-3. The first stage is from the TX coils to the rotor. Eddy current is induced in the rotor through the inductive coupling. The filamentary rotor can be modeled

as a lumped resistor and an inductor in series. The inductance and resistance can be calculated with the Finite Element Analysis (FEA) method or using the modeling developed in Chapter 2. The electrical properties of the coils as determined by both methods are listed in Table 6-2, which show good agreement with each other.

6.2.1   Design

(a)

(b)   (c)
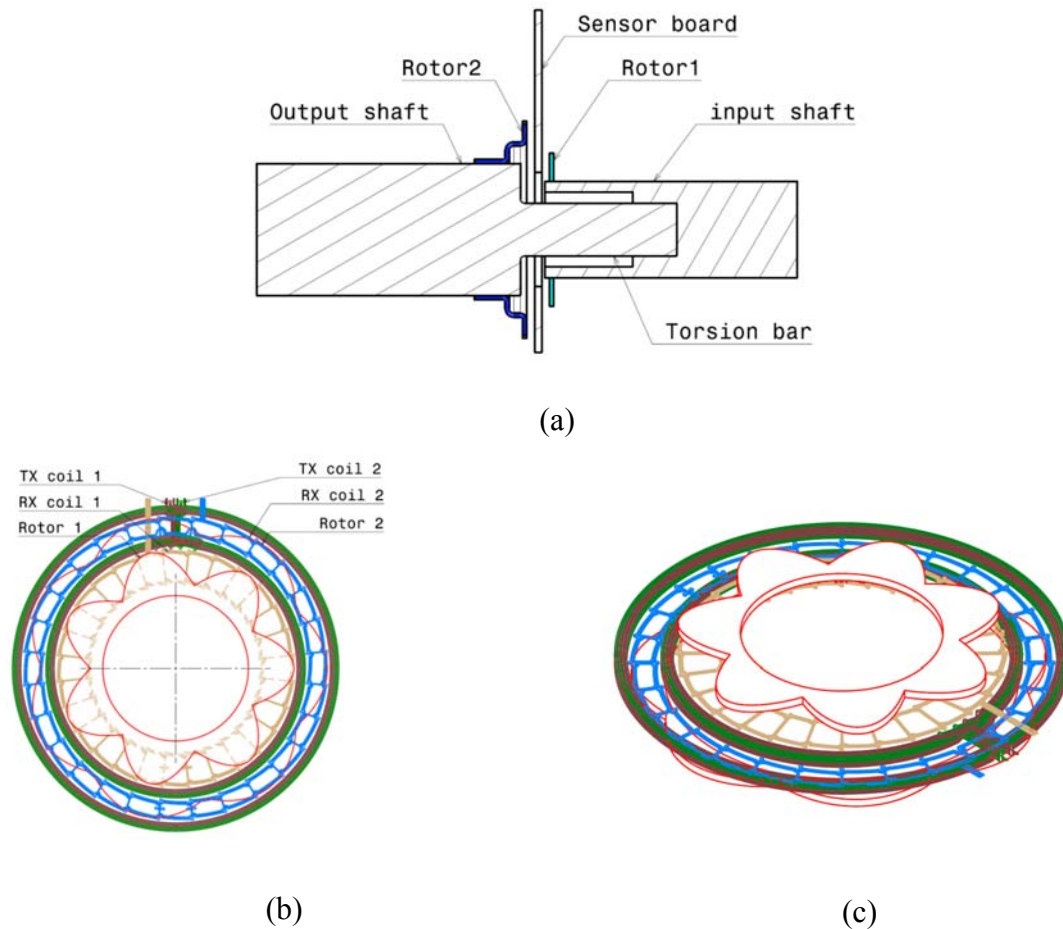
Figure 6-2 (a) Steering torque sensor assembly. (a) sensor top view; (b) sensor iso view.

The torque sensor consists of a stationary sensor PCB and two metallic rotors. These two rotors are mounted on two shafts, which are connected by a compliant torsional bar as demonstrated in Figure 6-2(a). Design parameters, listed in Table 6-1, were chosen to accommodate for the sensor in the given space while maintaining a good signal noise ratio.

Table 6-1 Design parameters

Description	Name	Value	Unit
Rotor1			
Thickness	Trt_1	0.1	mm
Major radius	$Rrta_1$	19.5	mm
Minor radius	$Rrtb_1$	7.97	mm
Rotor2			
Thickness	Trt_2	0.1	mm
Major radius	$Rrta_2$	25.0	mm
Minor radius	$Rrtb_2$	15.66	mm
TX coil			
Inner radius	Rtx_1	21.3	mm
Outer radius	Rtx_2	26.8	mm
Turns	Ntx	4	n/a
Trace width	Wtx	0.2	mm
Trace pitch	Ptx	0.4	mm
RX1 coil			
Inner spiral staring radius	Rrx_1s_1	14	mm
Inner spiral ending radius	Rrx_1e_1	14.6	mm
Outer spiral staring radius	Rrx_1s_2	18.9	mm
Outer spiral ending radius	Rrx_1e_2	19.5	mm
Trace width	Wrx_1	0.15	mm
RX2 coil			
Inner spiral staring radius	Rrx_2s_1	21.9	mm
Inner spiral ending radius	Rrx_2e_1	22.5	mm
Outer spiral staring radius	Rrx_2s_2	24.4	mm
Outer spiral ending radius	Rrx_2e_2	25	mm
Trace width	Wrx_2	0.15	mm

6.2.2   ISTS oscillator equivalent circuit

The equivalent circuit of the oscillator of ISTS can be modeled as a LCR network coupled through mutual inductance, as illustrated in Figure 6-3. The corresponding electrical properties can be calculated using the method developed in chapter 2 or by FEA. The

corresponding values for those properties as determined by both methods are listed in table 6-2, which shows good agreement.
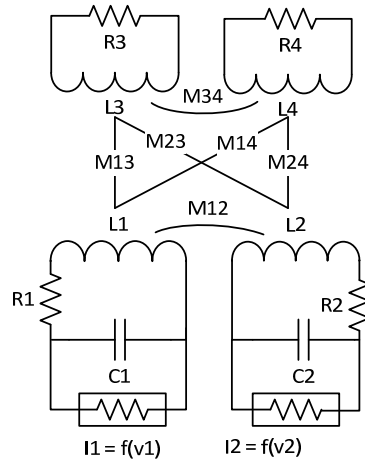
Figure 6-3 ISTS oscillator equivalent circuit

Table 6-2 Electrical propertied of the coils

Description	Name	Model	FEA	Unit
TX coil resistance	$R_{1,2}$	2.957	2.949	Ω
Rotor1 resistance	R_3	88.72	87.77	mΩ
Rotor2 resistance	R_4	101.90	102.78	mΩ
TX coil inductance	$L_{1,2}$	5244.6	5250.2	μH
Rotor1 inductance	L_3	122.31	123.34	μH
Rotor2 inductance	L_4	164.08	165.82	μH
Mutual inductance of TX	M_{12}	4684.0	4557.3	μH

The corresponding mutual inductance between the TX coils and the rotors at different air gaps is presented in Figure 6-4. The mutual inductance between the RX coils and the rotors at different air gaps and angles is presented in Figure 6-5, which shows that the signal is two orders stronger than the cross-talk.

(a)

(b)

(c)
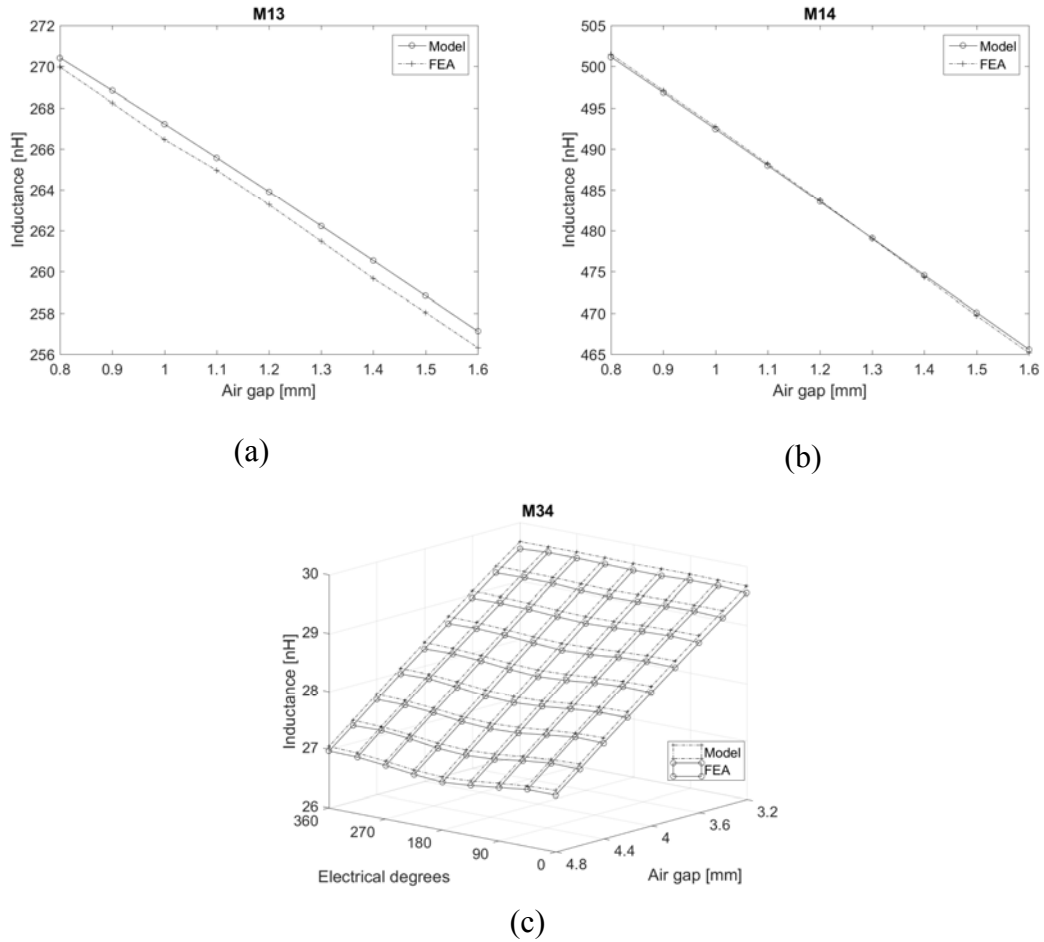
Figure 6-4 Mutual inductance (a) TX coil and rotor 1, (b) TX coil and rotor 2, (c) Rotor1 and Rotor 2

(a)

(b)

(c)

(d)

(e)

(f)

(g)

(h)
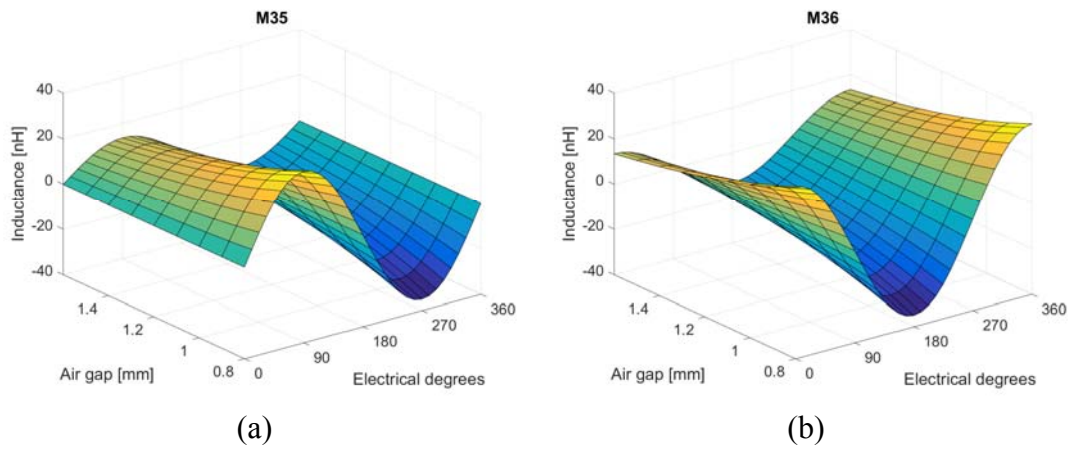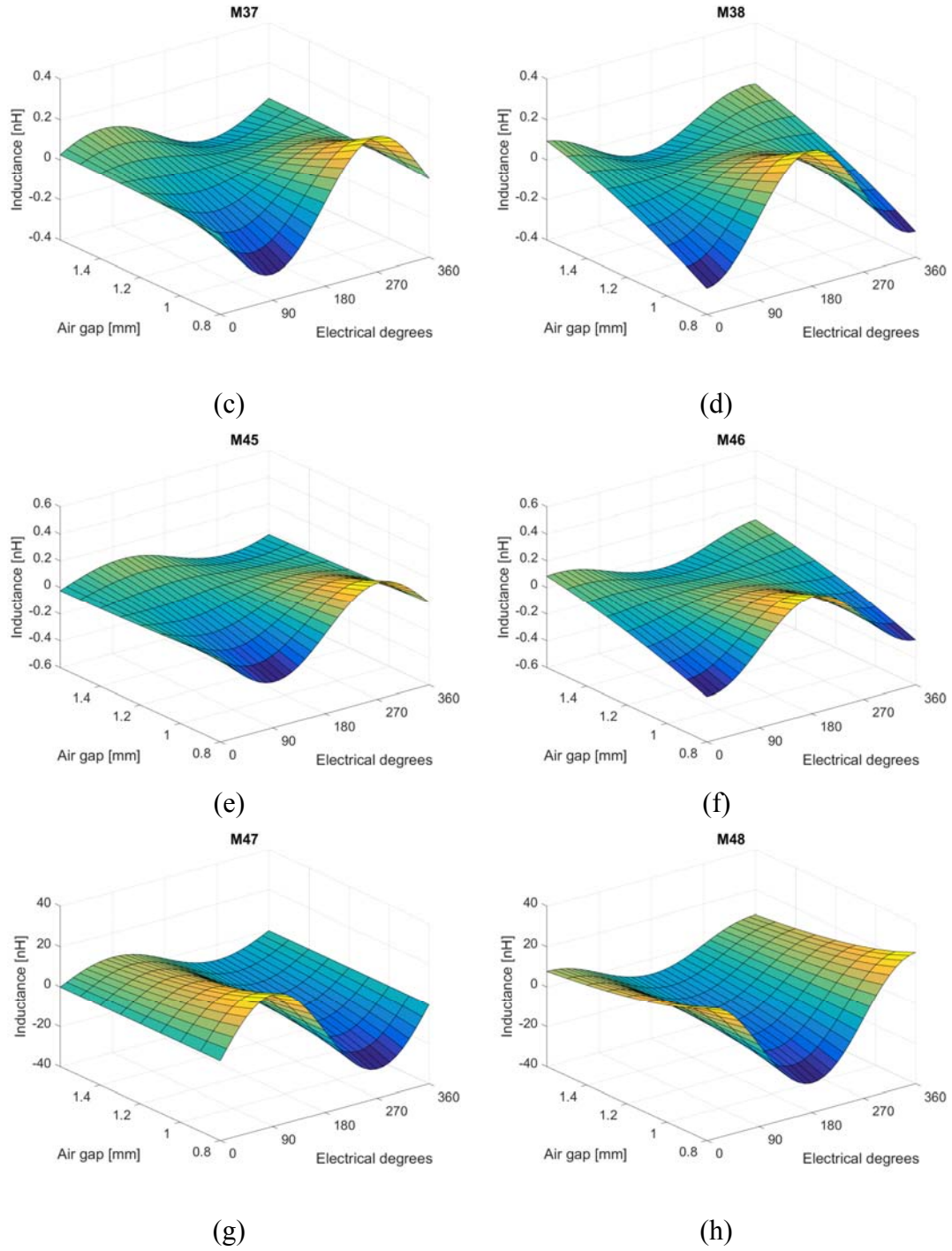
Figure 6-5 Mutual inductance between the RX coils and rotors at different angle and air gap.

6.3   Modeling

When the equivalent circuit and its electrical parameters are determined, the sensor output can be simulated in the Simulation Program with Integrated Circuit Emphasis (SPICE). However, SPICE is very slow to simulate the transient behavior of the circuit. Moreover, SPICE is not capable of simulating sensor dynamics when the sensor electrical parameters change with time. To address this issue, a lumped model is selected for the torque sensor, with its performance governed by nonlinear differential equations. These equations can be solved by using MATLAB. A SPICE simulation with fixed angle serves as a benchmark to validate the modeling. After the modeling is validated, the system dynamic behavior is further studied using this model.

The model can be established from the current and voltage relation of the ISTS derived from *KCL and KVL,* as explained in chapter 2, i.e.,

$$
\begin{pmatrix}
L_1 & M_{12} & M_{13} & M_{14} & 0 & 0 \\
M_{12} & L_2 & M_{23} & M_{24} & 0 & 0 \\
M_{13} & M_{23} & L_3 & M_{34} & 0 & 0 \\
M_{14} & M_{24} & M_{34} & L_4 & 0 & 0 \\
0 & 0 & 0 & 0 & C_1 & 0 \\
0 & 0 & 0 & 0 & 0 & C_2
\end{pmatrix}
\begin{pmatrix}
\dfrac{d}{dt}i_1(t) \\
\dfrac{d}{dt}i_2(t) \\
\dfrac{d}{dt}i_3(t) \\
\dfrac{d}{dt}i_4(t) \\
\dfrac{d}{dt}v_1(t) \\
\dfrac{d}{dt}v_2(t)
\end{pmatrix}
=
\begin{pmatrix}
v_1(t)-i_1(t)R_1 \\
v_2(t)-i_2(t)R_2 \\
-i_3(t)R_3 \\
-i_4(t)R_4 \\
-i_1(t)-S_1\tanh\left(\dfrac{G_{n1}}{S_1}v_1(t)\right) \\
-i_2(t)-S_2\tanh\left(\dfrac{G_{n2}}{S_2}v_2(t)\right)
\end{pmatrix}
\tag{6-1}
$$

where the mutual inductance is expressed as $M_{ij}=k_{ij}\sqrt{L_iL_j}$, with k_{ij} being the inductive coupling coefficient between the inductors L_i and L_j . Compared with the governing equation of micro-inductive position sensor, equation (6-1) has one more nonlinear resistor, which makes beating between two oscillators possible. Equation (6-1) is a system of stiff differential equations, which can be numerically solved with MATLAB ODE23S solver. Its corresponding SIMULINK model and SPICE model are demonstated in Figure 6-2 (a) and (b), respectively.
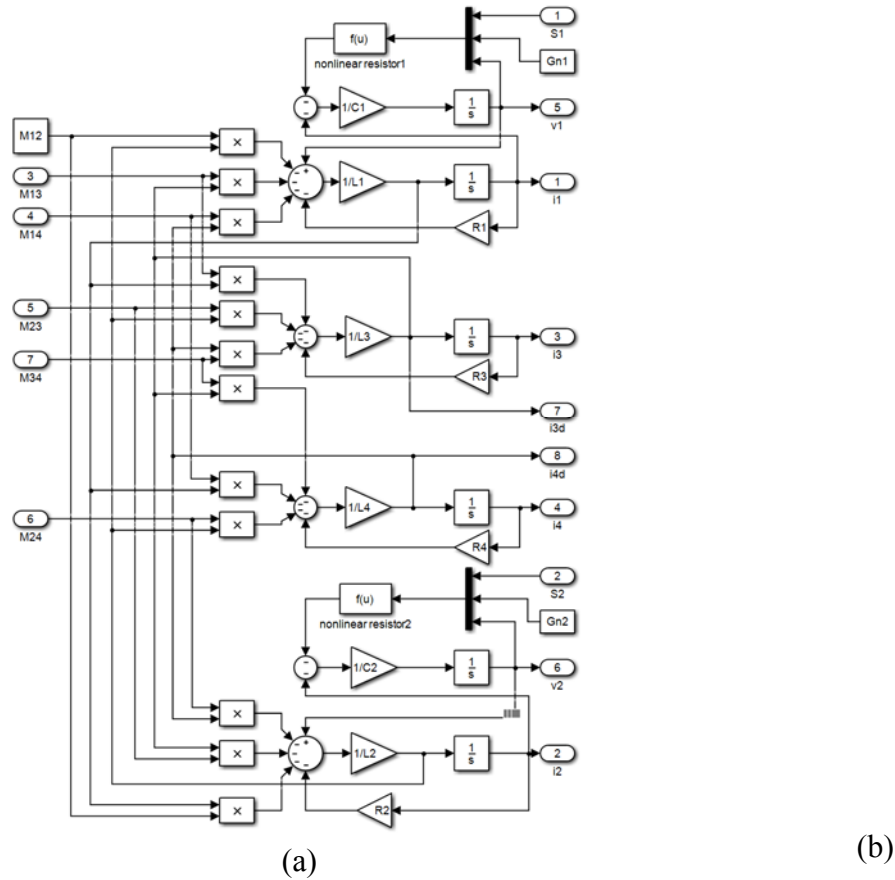
Figure 6-6 inductively coupled oscillator (a) Simulink model (b)SPICE model.

Two coupled oscillators have 4 degree of freedom (DoF). Depending on the configuration of the capacitor and the coupling coefficient, the two oscillators can oscillate in 4 different modes: two oscillators are in opposite phase, same phase, quadrature phase or independent phase, as demonstrated in Figure 6-7. It should be noted that mode switching can change the operating frequency and the signal strength, which will change the sensor output accordingly. In order to ensure sensor accuracy, two oscillators should always operate in one specific mode. Therefore, the mode switching condition and the safety margin must be identified, which are elaborated in the following section by numerical simulation.

In phase operation is preferred since the system Q factor is high and the signal strength is high. Two oscillators tend to operate at in phase mode when the coupling coefficient is high. Therefore two TX coils should be positioned closely to improve the coupling

coefficient. FEA and circuit simulation shows that the current layout can ensure in phase operation.
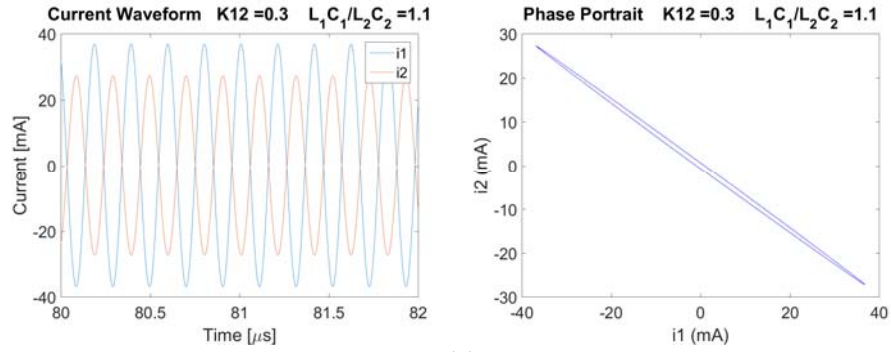
(a)
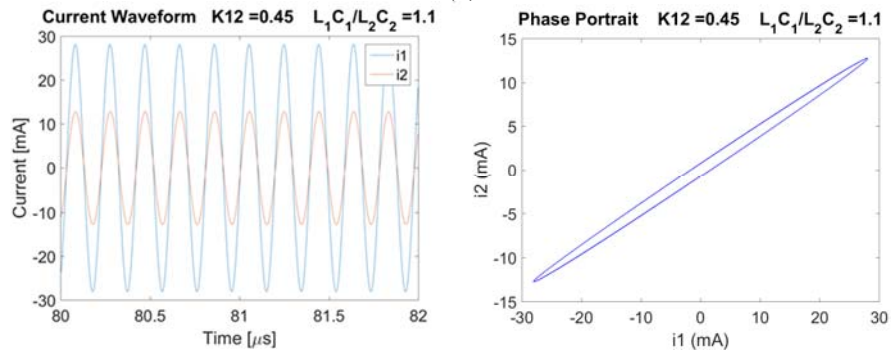
(b)
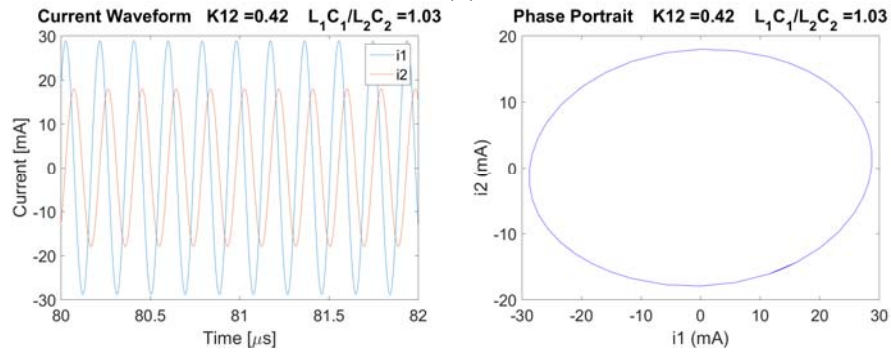
(c)
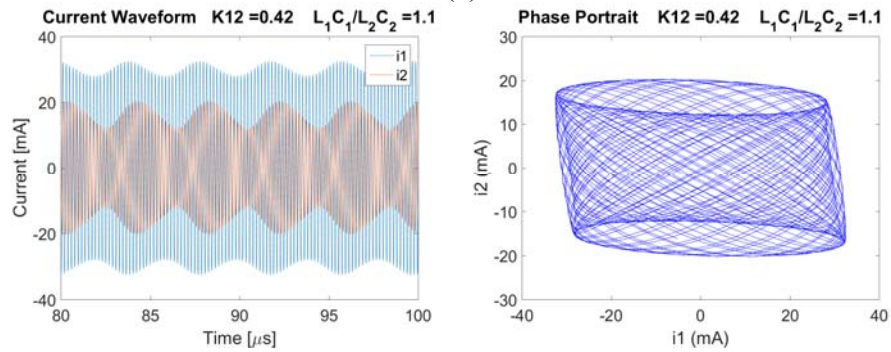
(d)

Figure 6-7 two oscillator (a) in opposite phase (b) same phase (c) quadrature phase (d) independently.

Since the mutual inductance between the RX and TX coils is neglegible, the receiving signals can be expressed as:

$$\begin{pmatrix} v_5(t) \\ v_6(t) \\ v_7(t) \\ v_8(t) \end{pmatrix} = \begin{pmatrix} M_{35} & M_{45} \\ M_{36} & M_{46} \\ M_{37} & M_{47} \\ M_{38} & M_{48} \end{pmatrix} \begin{pmatrix} \dfrac{d}{dt} i_3(t) \\ \dfrac{d}{dt} i_4(t) \end{pmatrix} \tag{6-2}$$
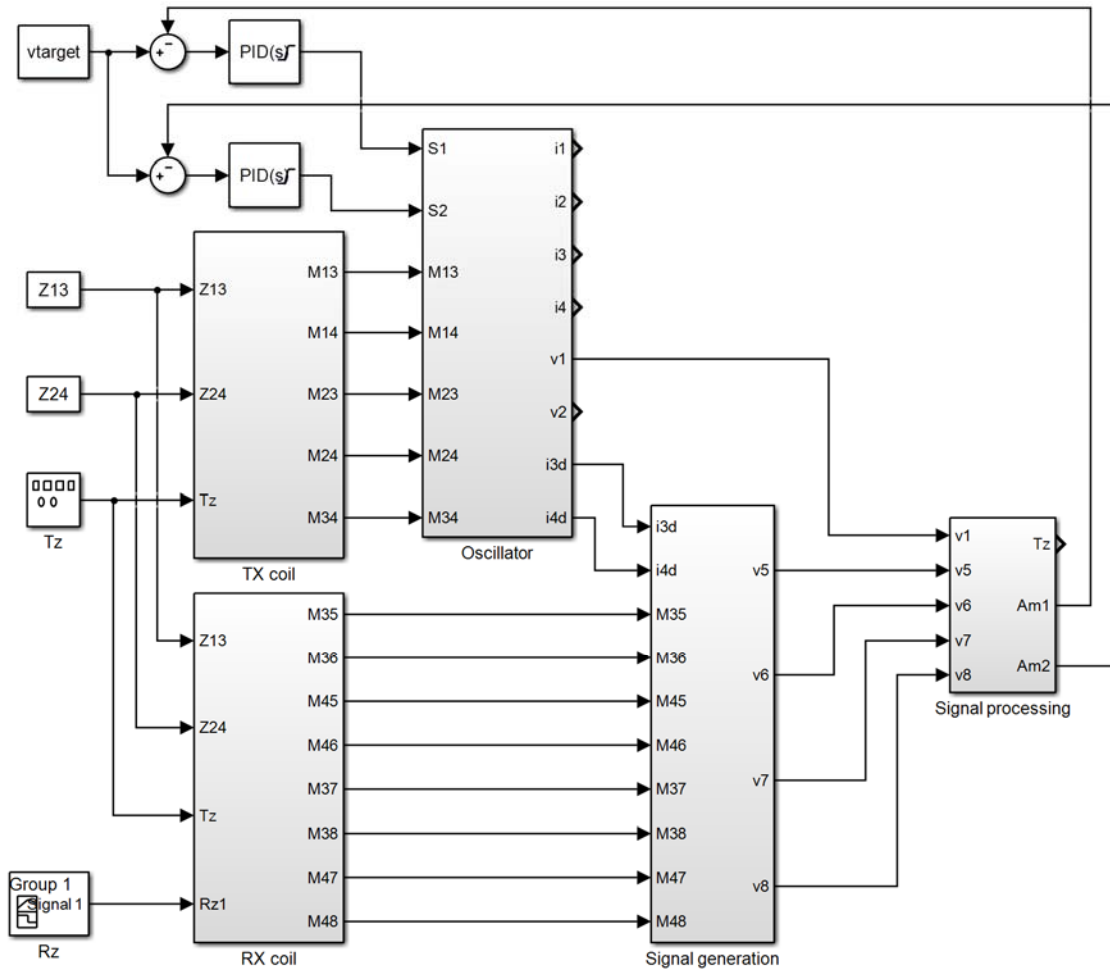
Figure 6-8 Steering torque sensor system model

The overall system model comprises 5 main blocks, as shown in figure 6-8. The TX and RX coil block generate the electrical properties of TX and RX coils according to the model developed in chapter 2. The oscillator block generates an Eddy current on two rotors from the bias current input, which is regulated by the signal strength feedback PI controller. The receiving signal is generated by the signal generation block, and it is further demodulated and computed by the signal processing block.

The bias current and signal strength at different air gap is illustrated in Figure 6-9 (a) and (b). It shows that receiving signal 2 is stable regardless of the air gap, while receiving signal 1 is sensitive to the air gap of both rotors. The Figure 6-9 (c) shows only in very narrow region both bias currents are in feedback mode, in most region the bias current of the closer sensor is zero, where the signal strength is greater than the target value. It should be noted that too high signal strength could saturated the analog/digital converter of the signal processing circuit and introduce sensor error. Therefore, the rotor air gap needs be well controlled to ensure optimal sensor performance.
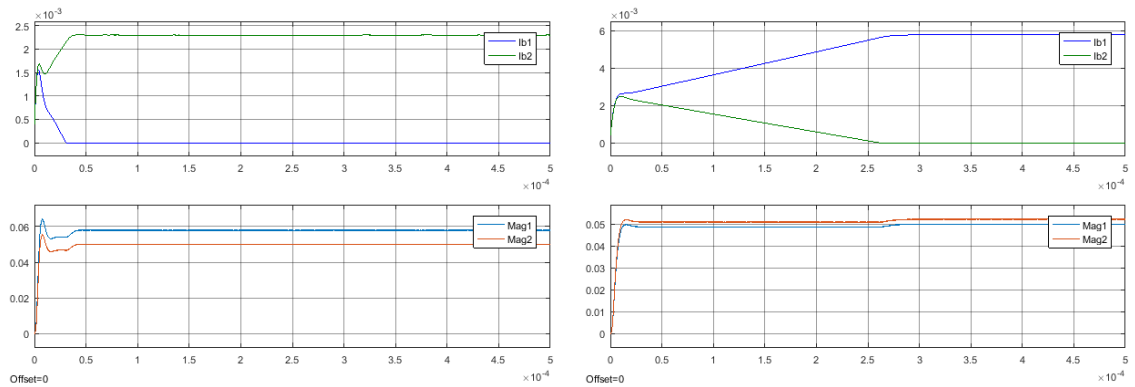
(a)

(b)
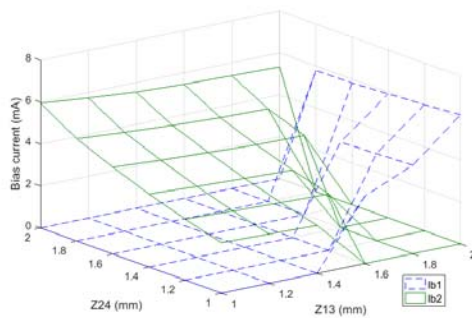
(c)
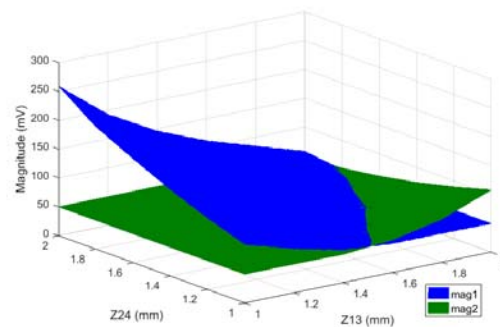
(d)

Figure 6-9 (a) Bias current and signal magnitude waveform when z13 = 1.4mm and Z24 = 1mm; (b) Bias current and signal magnitude waveform when z13 = 2.0mm and Z24 = 1.8mm; (c) Bias current at different rotor air gap combination; (d) signal magnitude at different rotor air gap combination.

6.4   Experiment

6.4.1   Experiment set

The design is to determine the torque by measuring the torsion angle of a compliant bar, which is further measured by the difference of two rotor angles. The purpose of the test is to validate that the torsional angle output has enough accuracy and the fluctuation of the output is within a certain range when both rotors are locked together and rotate 360 degrees. A test bench is developed to assess the performance of the steering torque sensor, which comprises of a mechanical fixture and a data acquisition system, as shown in Figure 6-10. The mechanical fixture can operate in two modes: fixed torsion angle mode and fixed rotor 1 mode. In the fixed torsion angle mode, the relative angle between the two rotors is fixed, and the whole assembly is driven by a step motor. This mode is used to measure the output fluctuation with respect to the steering angle. In fixed rotor 1 mode, the small rotor is fixed, while only big rotor can be freely rotated by the step motor. This mode is used to measure the cross-talk between two sensors. The data acquisition system consists of a 12 bit optical encoder detecting the step motor position, a NI DAQ device monitoring the sensor PWM output, and Labview software controlling the step motor and recording the data.
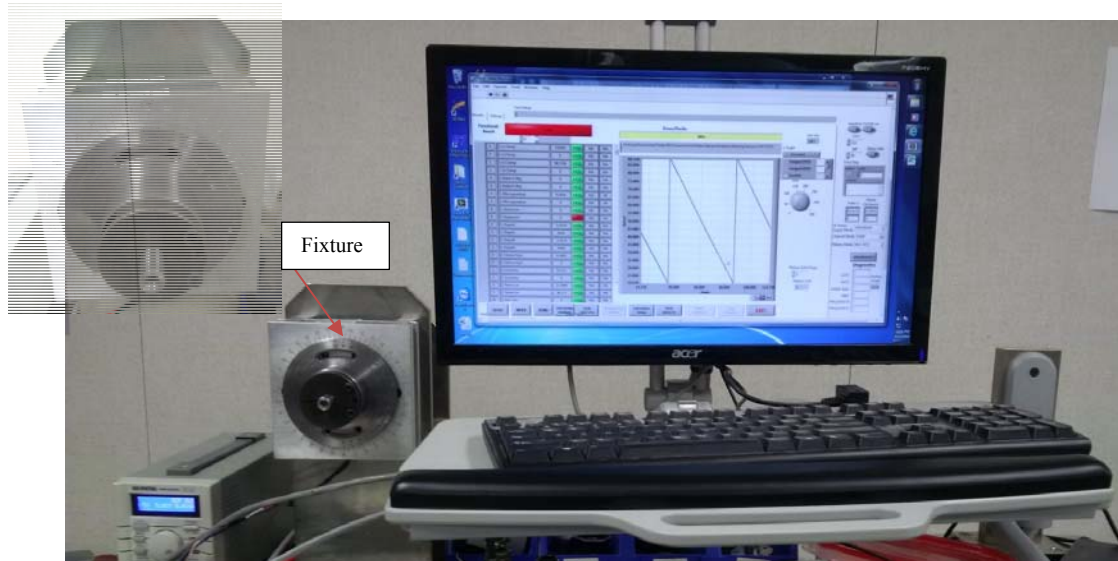
Figure 6-10 Experiment setup

6.4.2   Sensor transfer function

The test is first run in the fixed torsion angle mode. 7 torsion angle positions ranging from -8 degrees to 8 degrees, with increment of 2 degrees, are tested. The test result is shown in Figure 6-9. The torsion angle is calculated by,

$$\phi = \text{mod}(\theta_1 - \theta_2, 360) \tag{6-3}$$

where θ_1 and θ_2 are angles of the two rotors, respectively. ϕ ranges from -180 degrees to 180 degrees.

The linearity of this design is ±1.2 %, and the sensor error has a period of 360/7 degrees.

(a)   (b)

(c)

(d)
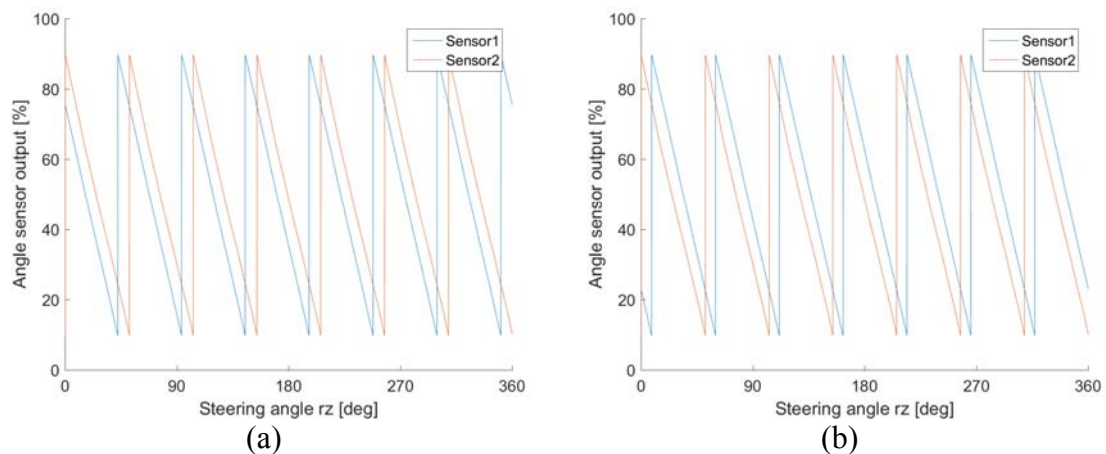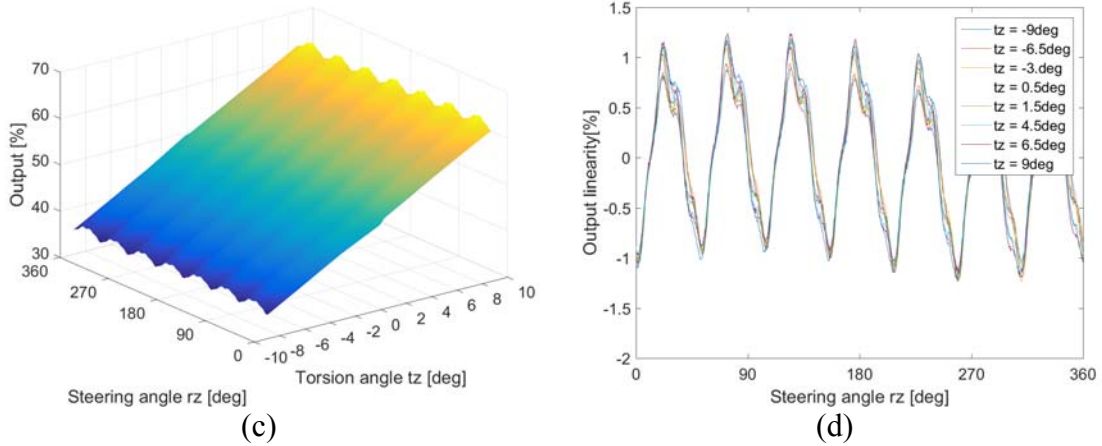
Figure 6-9 (a) & (b) output for torsion angle of -8 and 8 degrees, respectively, (c) torsion angle output vs. steering angle, (d) torsion angle error.

6.4.3   Cross-talk between two sensors

(a)

(b)

(c)

(d)
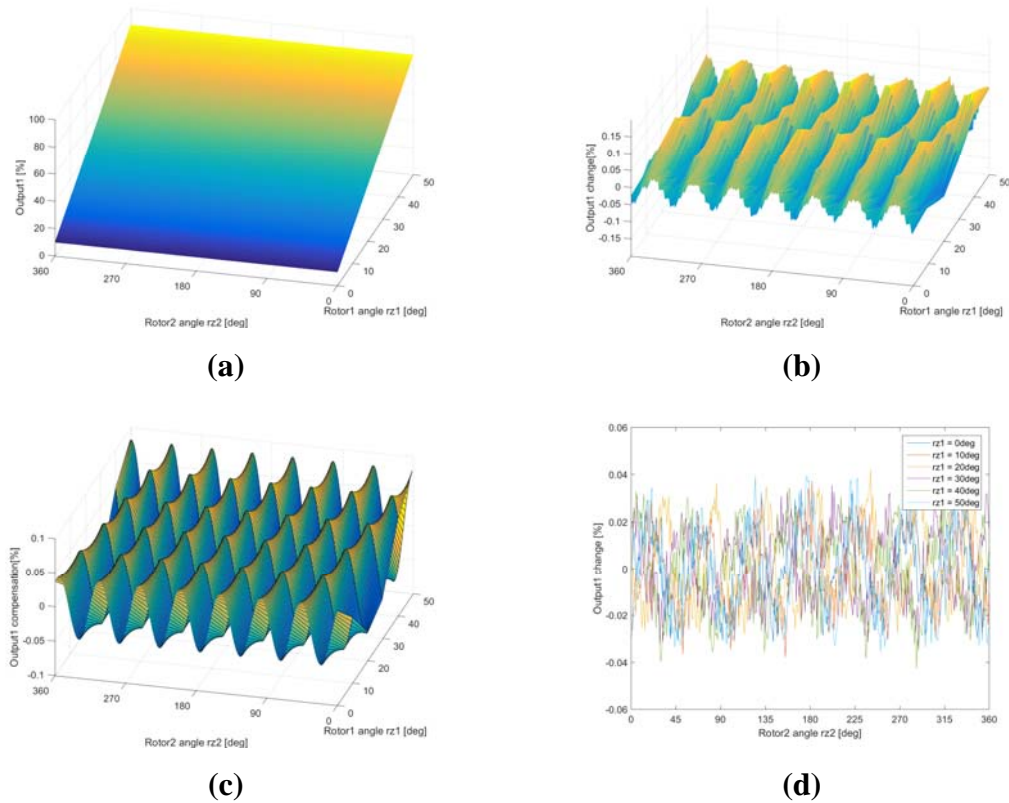
Figure 6-10 (a) sensor output 1 when rotor 1 is fixed at different position and rotor 2 is rotating, (b) output 1 change caused by rotor 2, (c) cross-talk compensation, (d) residue cross-talk after compensation.

Since the torsion angle is calculated by the difference of two angle sensor outputs, the cross-talk between those two angle sensors should be minimized. Otherwise, a sophisticated algorithm needs to be developed to compensate for the error caused by the cross-talk. In order to measure the cross-talk between the two sensors, rotor 1 is fixed to the fixture, and the output 1 from the sensor 1 is monitored while rotor 2 rotates 360 degrees. Since the fluctuation of output 1 is only affected by the position of rotor 2, it represents the cross-talk between two sensors. Figure 6-11(a) and (b) show output 1 and its fluctuation when rotor 1 is fixed and rotor 2 rotates by 360 degrees. The data shows that the rotor 2 causes output 1 to change by ±0.1%, which is within the acceptable range for the ±1% sensor accuracy requirement. The cross-talk presents a regular pattern, which means that it is possible to be compensated by the two sensor outputs. By inspection the compensation function can be in the form:

$$\phi = \mod(\theta_1 - \theta_2, 360) + (a_1\theta_1 + b_1) * \cos(a_2\theta_2 + b_2) \tag{6-4}$$

where θ_1 and θ_2 are angles of the two rotors, and a_1, a_2, b_1 and b_2 are compensation coefficients from curve fitting.

With the compensation shown in Figure 6-10(c), the residual cross-talk is reduced to ±0.04% (Figure 6-10(d)).

6.4.4 Angle sensor linearity improvement

The experiment shows that the cross-talk between two angle sensors is only ±0.15%, which means the cross-talk is not the major contributor of torsion angle error. It is thus concluded that the nonlinearity of two individual angle sensors is the main error source. The linearity of the angle sensor can be improved through rotor shape optimization and a linearizer in the signal processing stage.

(a)

(b)

(c)

(d)
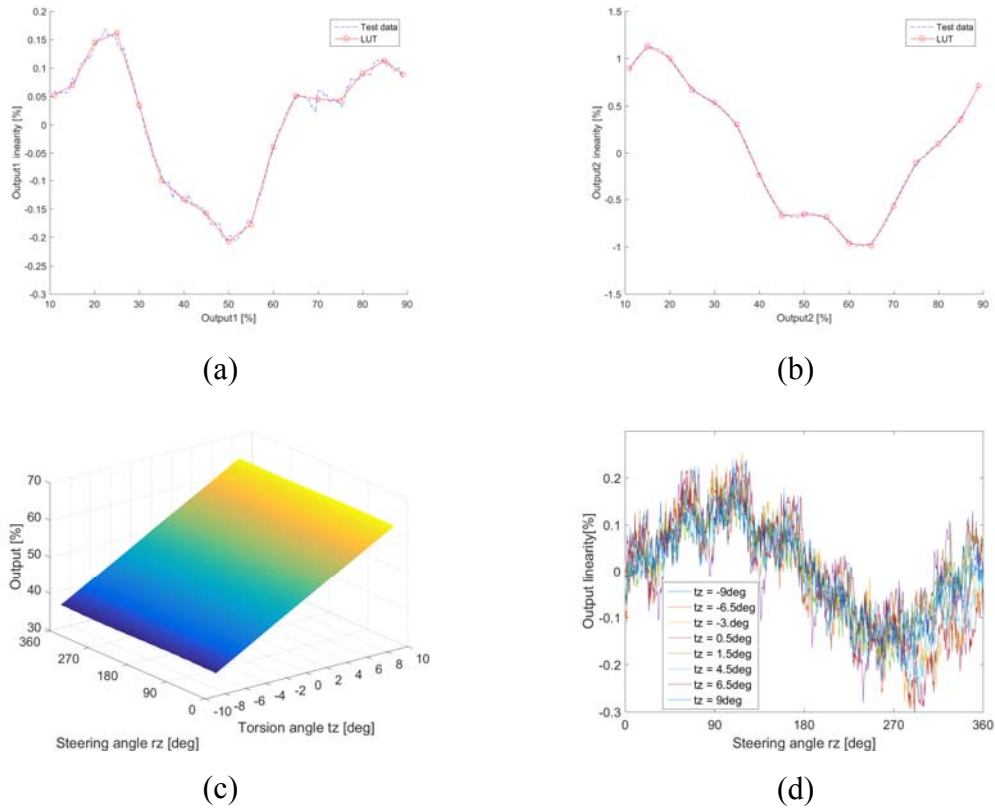
Figure 6-11 (a) & (b) Sensor 1 & 2 linearizer look-up table, (c) sensor output after linearization, (d) sensor linearity.

6.5   Conclusion

An inductive steering torque sensor is developed. A mathematic model of the sensor is developed and validated by FEA and SPICE circuit simulations. The design is then optimized using the developed model. A prototype is built and tested in the test bench, which gives the sensor accuracy of ±1.2% without any compensation. It is found that the cross-talk between two angle sensors is negligible, which suggests that the main error source of the sensor is the linearity of two individual angle sensors. Based on this finding, a piecewise linearizer algorithm is designed to improve the sensor accuracy, resulting in the sensor accuracy improvement to ±0.25% after a 17-points linearizer compensation.

Chapter 7

7 Passive Inductor-capacitor Sensor

7.1 Introduction

Passive inductor-capacitor (LC) sensors are one of the key modules in a number of non-contact measurement applications [73]. Compared to their active counterpart, the major merits of passive sensors include low power consumption and electromagnetic emission. One of the simple types of wireless passive sensors is an inductive coupling based inductor-capacitor resonator. LC passive sensors use a transformer between an external readout coil and an inductor that receives power through the inductive coupling, and the readout coil detects the changes in the sensor wirelessly. Remote query capability is one of the main advantages of LC sensors. Sensor information can be obtained without physical connections, and thus LC sensors can be applied in harsh and sealed environments where physical access to the sensor is difficult or even impossible. Examples of these applications are the sensors on moving parts such as an automobile tire [74], patient health monitoring [75], and sensing under harsh environmental conditions [76]. The other advantage of LC sensors is their battery-free operation, which minimizes their size and maximizes extended continuous usage. The simple structure of LC sensors also achieves low cost. LC sensors date back as early as the 1960s, but has seen rapid growth in the past decade due to improvements to microelectromechanical systems. The development of Internet of Things (IoT) [77] for applications such as implantable sensors and wearable devices [78] further attracts attention to the LC passive wireless sensor research field. LC sensors comprise two magnetically coupled coils [79]: a sensor coil, which is connected to a capacitive sensor and forms an LC tank circuit, and an interrogator coil, which is connected to a measurement circuit. The resonance frequency of the tank circuit is a function of change in capacitance and inductance of the sensing elements. Most of the existing schemes detect the corresponding shift in resonance frequency using appropriate readout electronics and an impedance analyzer [80, 81]. Several techniques have been reported to measure the change in resonance frequency and produce an output [75, 82]. One of these techniques is to detect the resonance frequency and its shift by measuring the Phase-dip [75]. In this method, the phase of the impedance seen by the readout circuit is obtained over a wide range of

frequencies. From this impedance sweep information, the frequency of the minimum phase value is noted as $f_{\min}$, which is taken as the resonance frequency f_r. It has been reported that f_r can deviate from $f_{\min}$ depending on the quality factor Q and the coupling factor k of the system [83]. Similarly, it has been shown that the phase-dip measurement has a strong dependence on k, especially when the coils are in close proximity or when the coupling coefficient k is large [84]. The work presented in [81] reports that the maximum value of the real part of the impedance that occurs at f_r is independent of the value of k. Among the methods listed above, the readout system and measurement procedure require either excitation at multiple frequencies or a frequency sweep, which is realizable but at the cost of increasing measurement time and expensive hardware, e.g. a Voltage Controlled Oscillator. Another disadvantage of the frequency sweep approach lies in the errors associated with the transient behavior of the system [85]. Considering the above facts, a scheme that can obtain an accurate measurement output at a single frequency while minimizing the amount of hardware is desirable.

Passive inductive position sensors without the excitation coil are demonstrated in this chapter. The sensor is made of PCB coil and off-the-shelf integrated circuit components. Since the excitation signal is only applied when the sensor is being measured, the emission and power consumption can be reduced. A signal processing and error compensation algorithm is discussed after analyzing the signal characteristics.

7.2   Design and modeling of passive position sensor
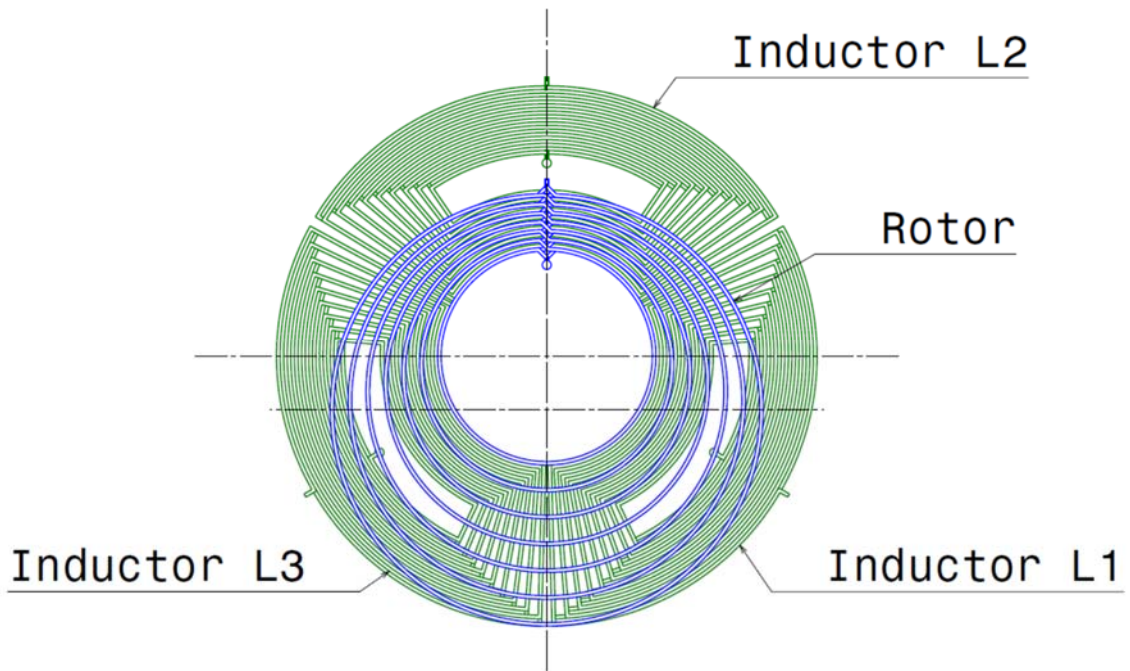
Figure 7-1 Inductive angle position sensor design.

The inductive sensor includes three identical inductors made of wounded copper coils of 35µm thickness on a 1mm thick two-layer PCB board. The coils are offset 120 degrees from each other. The rotor comprises seven eccentric circular-shaped copper loops, as shown in Figure 7-1.
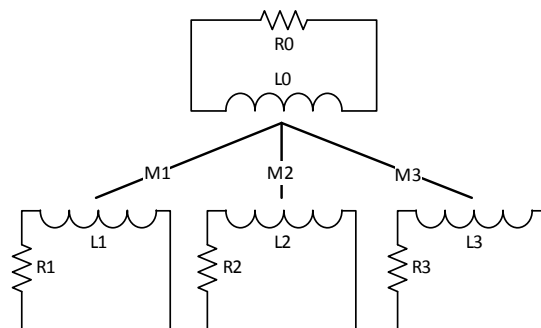
Figure 7-2 Sensor equivalent circuit model

The sensor can be modeled as a transformer (Figure 7-2). For angle sensing applications, the distance between the rotor and the coil is constant, while the coupling between the rotor

and the sensing inductor is a function of the rotor angle. In Figure 7-2, L_i and R_i are the *ith* sensing coil's inductance and series resistance, respectively. M_i is the mutual inductance between the rotor L_0 and the *ith* sensing coil, which is a function of angle θ. These angle dependant parameters can be used to measure rotor angle. For simplicity of analysis, since the mutual inductances between L_1, L_2 and L_3 are significantly lower than M_i, the mutual inductance between the sensing coils is neglected.

The current and voltage relation of the equivalent circuit can be derived from the transformer theory in phasor form:

$$\begin{pmatrix} 0 \\ v_i \end{pmatrix} = \begin{pmatrix} j\varpi L_0 + R_0 & j\varpi M_i(\theta) \\ j\varpi M_i(\theta) & j\varpi L_i + R_i \end{pmatrix} \begin{pmatrix} i_0 \\ i_i \end{pmatrix}, i = 1..3 \tag{7-1}$$

Therefore, the equivalent impedance of the receiving coil is:

$$z_i = \frac{v_i}{i_i} = j\varpi L_i + R_i + \frac{\varpi^2 M_i^2(\theta)}{j\varpi L_0 + R_0} \tag{7-2}$$

Defining the quality factor of the rotor coil Q and the coupling coefficient k_i between the rotor coil and the *ith* sensing coil, i.e.

$$Q = \frac{\varpi L_0}{R_0} \tag{7-3}$$

$$k_i(\theta) = \frac{M_i(\theta)}{\sqrt{L_0 L_i}} \tag{7-4}$$

The equivalent inductance of the sensing coil is expressed as,

$$L_{ei} = \mathrm{Im}(\frac{z_i}{\varpi}) = L_i - \frac{k_i^2(\theta)}{1 + \frac{1}{Q^2}} L_0 \tag{7-5}$$

Under normal circumstance, i.e. $Q \gg 1$, the equivalent inductance of the sensing coil can be approximated as,

$$L_{ei} = L_i - k_i^2(\theta)L_0 \tag{7-6}$$

Due to geometrical symmetry, the following equation is always valid:

$$L_i = L, \, i = 1..3 \tag{7-7}$$

$$k_2(\theta) = k_1(\theta + \frac{2\pi}{3}) \tag{7-8}$$

$$k_3(\theta) = k_1(\theta + \frac{4\pi}{3}) \tag{7-9}$$

To calculate the angle position, cosine and sine signals are derived by α–β transformation [86]:

$$
\begin{pmatrix} L_{\cos}(\theta) \\ L_{\sin}(\theta) \end{pmatrix} = \frac{2}{3}\begin{pmatrix} 1 & -\frac{1}{2} & -\frac{1}{2} \\ 0 & \frac{\sqrt{3}}{2} & -\frac{\sqrt{3}}{2} \end{pmatrix}\begin{pmatrix} L_{e1}(\theta) \\ L_{e2}(\theta) \\ L_{e3}(\theta) \end{pmatrix}
$$

$$
= \frac{2L_0}{3}\begin{pmatrix} -1 & \frac{1}{2} & \frac{1}{2} \\ 0 & -\frac{\sqrt{3}}{2} & \frac{\sqrt{3}}{2} \end{pmatrix}\begin{pmatrix} k_1^2(\theta) \\ k_1^2(\theta + \frac{2\pi}{3}) \\ k_1^2(\theta + \frac{4\pi}{3}) \end{pmatrix} \tag{7-10}
$$

The inductance and the resistance of the sensing coil can be evaluated with the finite element method in ANSYS Q3D. Simulation results show when the rotor angle is 0 degrees, coil L1 is covered by the rotor with the least area, resulting in minimum Eddy current induced on rotor and maximum inductance of L1. Conversely, when the rotor angle is 180 degrees, coil L1 is covered by the rotor with the most area, resulting in maximum Eddy current induced on the rotor and minimum inductance of L1. It also shows that more Eddy current is induced as air gap decreases; therefore, the fluctuation of coil inductance

from 0 degrees to 180 degrees is higher when the air gap between the coil and the rotor is smaller.
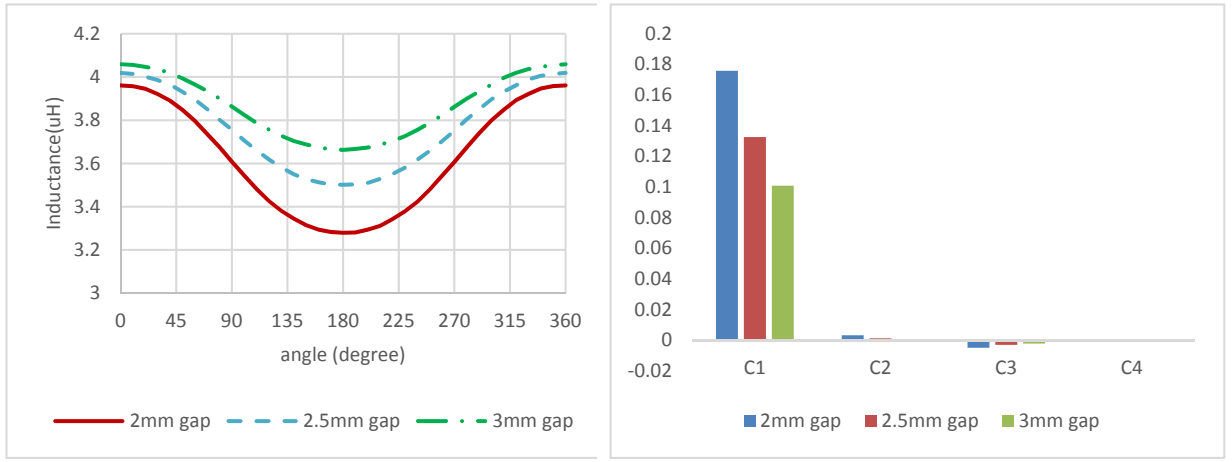
(a)   (b)

Figure 7-3 (a) Equivalent inductance of coil L1 vs. rotor angle; (b) Fourier coefficient of inductance, C_0 is not shown.

Based on the numerical simulation result demonstrated in Figure 7-3, the square of coupling coefficient $k_1^2(\theta)$ can be expanded into the following Fourier series:

$$k_1^2(\theta) = \sum_{i=0}^{\infty} c_i \cos(i\theta) \tag{7-11}$$

Position angle can then be evaluated by:

$$\tilde{\theta} = a \tan 2(L_{\cos}(\theta), L_{\sin}(\theta)) \tag{7-12}$$
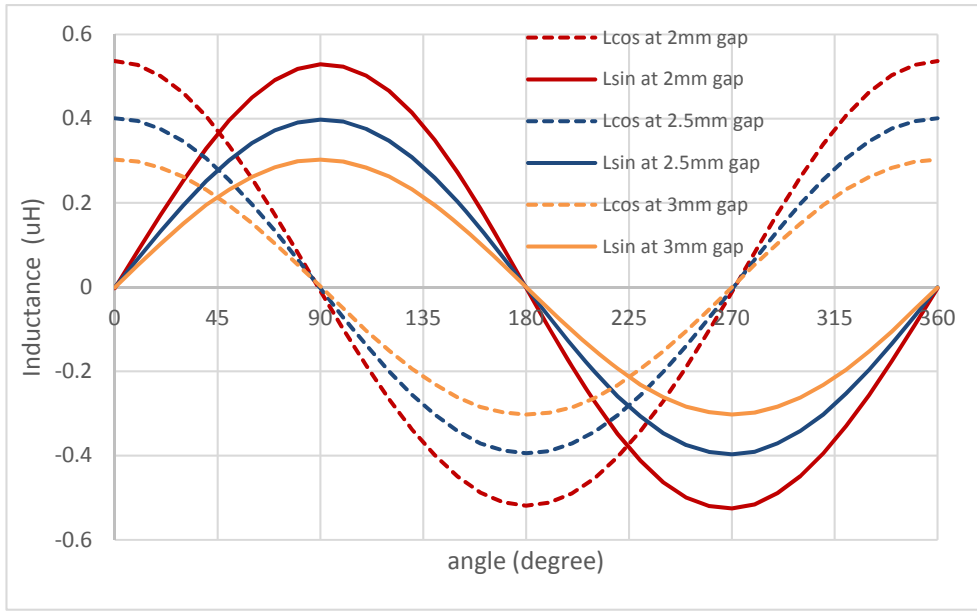
(a)
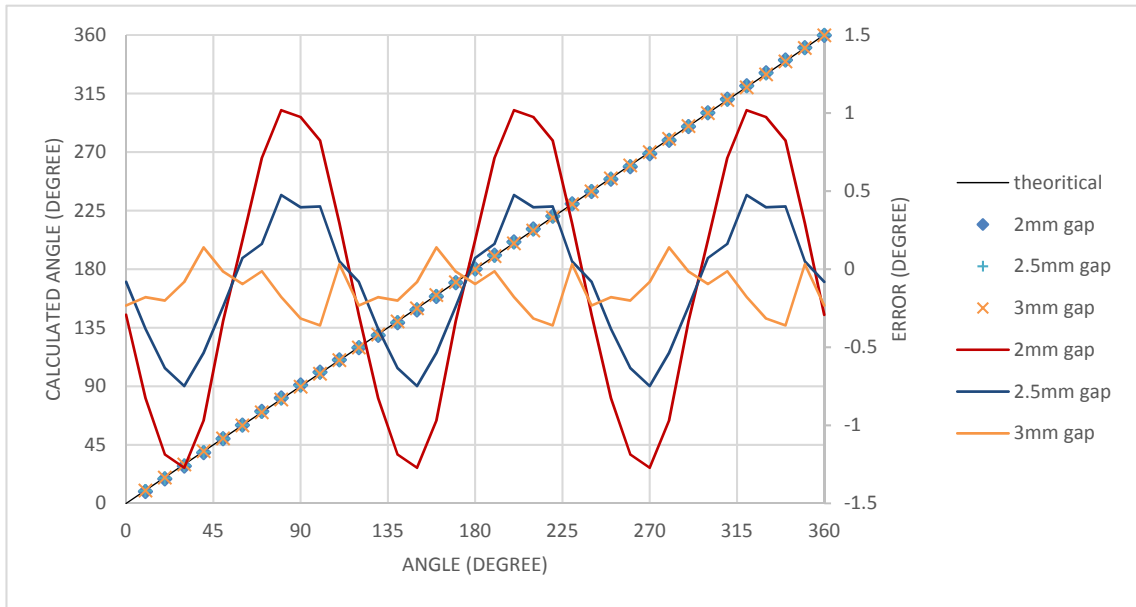
(b)

Figure 7-4 (a) sine and cosine signal; (b) calculated angle and error

Figure 7-4 shows that for smaller air gaps, both sine and cosine signal strength is higher but the error is also larger. To understand the error source, the following error analysis is conducted: Sine and cosine signals can be expressed by:

$$\begin{pmatrix} L_{cos}(\theta) \\ L_{sin}(\theta) \end{pmatrix} = \begin{pmatrix} c_1 \cos(\theta) + c_2 \cos(2\theta) + c_4 \cos(4\theta) + ... \\ c_1 \sin(\theta) + c_2 \sin(2\theta) + c_4 \sin(4\theta) + ... \end{pmatrix} \tag{7-13}$$

Let

$$x = c_1 \cos(\theta), \; y = c_1 \sin(\theta)$$
$$dx = c_2 \cos(2\theta) + c_4 \cos(4\theta) \tag{7-14}$$
$$dy = c_2 \sin(2\theta) + c_4 \sin(4\theta)$$

Substituting equation (7-14) into the equation (3-5), the error of the sensor output is determined as

$$\tilde{\theta} - \theta = \frac{(c_2 + c_4)\sin(3\theta)}{c_1} \tag{7-15}$$

Equation (7-15) shows that the error originates from the 2nd and 4th harmonics of coil inductance, while the 3rd harmonic effect is eliminated by the α–β transformation. The period of the error is 120 degrees. Equation (7-15) agrees with Figure 7-4(b). Since the error shows a regular pattern, it can be further compensated by equation (7-16), where the coefficients k and α can be derived by curve fitting. However, since the harmonics are different at different air gaps, the compensation coefficients should also change accordingly. Thus, the proposed error compensation method only works for a narrow air gap range.

$$\hat{\theta} = \tilde{\theta} + k * \sin(3\tilde{\theta} + \alpha) \tag{7-16}$$

Table 7-1 Error compensation comparison

Gap (mm)	k	α(°)	Error w/o compensation (°)	Error after compensation (°)

2.0	1.15	15	2.29	0.19
2.5	0.56	8	1.22	0.19
3.0	-0.12	0	0.50	0.40

Table 7-1 shows that error compensation works well with a small air gap, and the residual error comes from the high order harmonics and numerical error. However, with a large air gap, the improvement by error compensation is limited since the numerical error dominates.

7.3   Experiment design

The inductance of the sensing coil can be evaluated using a LDC1614 Inductance-to-Digital Converter by Texas Instruments. LDC1614 is composed of 4 front-end resonant circuit drivers, followed by a multiplexer that switches through the active channels, connecting them to the core that measures and digitizes the sensor frequency f_{sensor}. The inductance is evaluated by:

$$L = \frac{1}{(2\pi f_{sensor})^2 C}$$

(7-17)

The sensor system diagram is shown in Figure 7-5. The Inductance of three sensing coils is measured by the LDC1614, and the result is sent to microcontroller through I²C for signal processing.
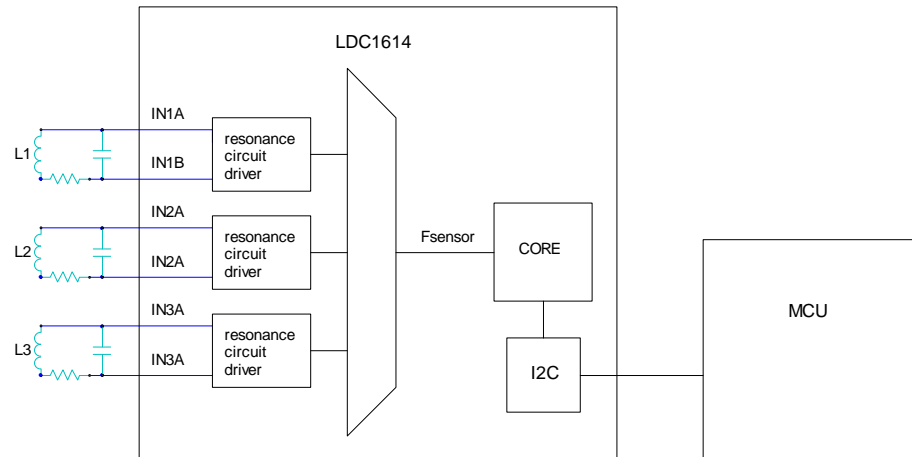
Figure 7-5 System diagram

7.4   Discussion and conclusion

In this chapter, a passive inductive position with a very simple structure is proposed. Such sensor expands the family of inductive position sensor. It can meet the tight power consumption and electromagnetic emission requirement, which is very difficult to meet by its active counterpart. The sensor performance is modeled analytically and then verified numerically. The sensor has good accuracy and is robust to air gap variation. Finally, a validation system with off-the-shelf components is proposed.

Chapter 8

8 Conclusion and future work

The goal of this research is to increase the understanding of inductive angular position sensor (IAPS) performance and apply this knowledge to advance sensor development and function for automotive applications. In pursuit of this goal, the existing base of research knowledge is drawn upon to provide a guide for subsequent modeling, optimization and conceptualization of new applications. The work presented in this thesis has demonstrated and proven the usage of low-cost inductive position sensor for automotive applications. Nevertheless, a significant amount of work remains for the commercialization of these technologies and the integration of these sensors into existing commercial applications.

8.1 Conclusion

Currently, modeling of IAPS is only limited to Finite Element Analysis (FEA), which is very time consuming and does not provide much insight of the sensor performance. A lumped model is crucial to understand the sensor performance and speed up the design optimization procedure. Taking the modeling of inductive angular position sensors as a starting point, extensive work has been dedicated to the characterization of IAPS performance by a lumped model through Neumann integration and the SIMULINK model. This model is further validated by FEA and Simulation Program with Integrated Circuit Emphasis (SPICE) simulation. The simulation results show very good agreement (within 2% of difference). Meanwhile, the proposed model requires significantly less computing time than FEA and SPICE simulations, and thus can be used as an efficient means to simulate the performance of IAPS.

The correlation between receiving signal imperfection and sensor output error is thoroughly investigated. The raw signal imperfection includes DC offset, amplitude mismatch, high order harmonics and quadrature phase shift error. The corresponding errors for both two-phase and three-phase configurations are studied and their specific pattern and period are presented. The analysis shows that three-phase configuration can effectively eliminate the error induced by $3^{\rd}$ order harmonics. However, a three-phase configuration is more expensive due to the extra sensing coil and corresponding signal processing circuit.

As an alternative, a modified rotor including the 3rd order harmonics shape is proposed to cancel out the 3rd order harmonics of the receiving signal. This method is proven to be effective and is widely used in other designs presented in this work. The correlation between sensor error and mechanical misalignment is further studied. Results obtained provide a design guideline of mechanical tolerance to meet a given sensor accuracy requirement.

IAPS optimization using response surface methodology (RSM) in presented. The response surface model can be used to predict the responses of a series of design parameters, which makes the optimization procedure very efficient. In addition, RSM can reveal the functional relationship between performance and design parameters.

A miniaturized inductive position sensor with 9mm diameter is developed. To overcome the weak signal due to the scale-down effect, a resonance rotor is introduced. After the concept is proven by numerical simulation, the copper structure is optimized specifically for the electrodeposition process and a sequence of microfabrication procedures is developed. The electrical properties of the device are characterized and show good agreement with the numerical simulation results. Lastly, the device is integrated into the sensor system to test sensor functionality. The test shows that the miniaturized inductive position sensor has moderate error (1%) over 0.4mm to 1.2mm air gap.

Chapter 6 presents the development of the steering torque sensor, which measures the relative angle of two rotating objects. It demonstrates the fusion of two inductive position sensors. The challenge of such design includes the coupling between two oscillators and the cross talk between two sensors. It has been found that two inductively coupled oscillators can operate at in-phase and out-of-phase mode, and mode switching can introduce error in the sensor output. We determine the condition of the oscillation mode based on the eigenvalue of the governing equation. Two oscillators can be guaranteed to operate in-phase by matching the self-resonance frequency and increasing the inductive coupling coefficient. The cross talk between two sensors is minimized by proper layout of the coils and is further reduced by a compensation algorithm. The concept is first verified

using the model developed in chapter 2, and then validated by a prototype. The experiment results show such a design can be accurate to 0.05 degrees.

Chapter 7 presents the development of a passive angle sensor. Passive inductive position sensors without the excitation coil can greatly reduce the power consumption and electromagnetic emission, which attracts more and more attention nowadays.

8.2   Future work

This thesis is focused on the theoretical modeling and design optimization of IAPS. New concepts of IAPS, including sensor miniaturization, sensor fusion and a passive sensor, have been proposed. However, the commercialization and integration of these concepts still remain a challenge for future work.

For the miniaturized IAPS, the main challenge lies in system integration. In order to make the sensor cost effective, the system-in-package design needs to be adopted. The device should be fabricated on a ferrite substrate to further reduce the cost.

Since the steering torque sensor is a safety critical component, to develop an integrated sensor system that can meet the safety requirement remains a challenge. The sensor needs to have two independent outputs without interfering with each other, and so the ASIC for signal processing should be very carefully designed to meet the strict requirement.

The passive sensor is a promising direction for IAPS due to its low emission and power consumption. However, its signal processing circuit is quite complicated and costly. A cost effective reading circuit needs to be developed in the future.

References

[1]   D. S. Nyce, *Linear position sensors : Theory and application*. Hoboken, N.J.: Wiley-Interscience, 2004.

[2]   C. S. Rangan, G. R. Sarma*, et al.*, *Instrumentation : Devices and systems*. New Delhi: Tata McGraw-Hill, 1983.

[3]   W. P. Eaton and J. H. Smith, "Micromachined pressure sensors: Review and recent developments," *Smart Materials and Structures,* vol. 6, pp. 530-539, Oct 1997.

[4]   J. M. Giachino and T. J. Miree, *The challenge of automotive sensors* vol. 2640. Bellingham: Spie - Int Soc Optical Engineering, 1995.

[5]   W. J. Fleming, "Overview of automotive sensors," *Ieee Sensors Journal,* vol. 1, pp. 296-308, Dec 2001.

[6]   W. J. Fleming, "New automotive sensors-a review," *Ieee Sensors Journal,* vol. 8, pp. 1900-1921, Nov-Dec 2008.

[7]   R. B. GmbH. *Bosch automotive electrics and automotive electronics systems and components, networking and hybrid drive (5th ed.).*

[8]   B. Lequesne, "Automotive electrification: The nonhybrid story," *Transportation Electrification, IEEE Transactions on,* vol. 1, pp. 40-53, 2015.

[9]   M. Bourogaoui, H. B. Sethom*, et al.*, "Speed/position sensor fault tolerant control in adjustable speed drives - a review," *Isa Transactions,* vol. 64, pp. 269-284, Sep 2016.

[10]   K. Yallup. *Technologies for smart sensors and sensor fusion.*

[11]   P. Kamenicky and P. Horsky, "An inductive position sensor asic," *Analog Circuit Design,* pp. 33-53, 2008.

[12]   K. Yoo, J.-w. Seo*, et al.*, "Study on development of torque and angle sensor for eps," *SAE International Journal of Passenger Cars-Electronic and Electrical Systems,* vol. 5, pp. 292-296, 2012.

[13]   M. A. Howard, "Next-generation inductive transducers for position measurement," 2012

[14]   J. Golby, "Advances in inductive position sensor technology," *Sensor Review,* vol. 30, pp. 142-147, 2010.

[15]   L. Shao, J. K. Lee*, et al.*, "Inductive position sensor," United States Patent, 2013.

[16]   H. Irle, N. Kost*, et al.*, "Inductive angle sensor having coupled oscillators with similar inductive response," United States Patent, 2001.

[17]   J. D. Jackson, *Classical electrodynamics*, 3rd ed. New York: Wiley, 1998.

[18]   E. B. Rosa and F. W. Grover, *Formulas and tables for the calculation of mutual and self-inductance*. Washington: Govt. Print. Off., 1916.

[19]   F. W. Grover, *Inductance calculations, working formulas and tables*. New York,: D. Van Nostrand company, inc., 1946.

[20]   H. A. Wheeler, "Formulas for the skin effect," *Proceedings of the IRE,* vol. 30, pp. 412-424, 1942.

[21]   F. Passos, M. H. Fino*, et al.*, "Lumped element model for arbitrarily shaped integrated inductors - a statistical analysis," *2013 Ieee International Conference on Microwaves, Communications, Antennas and Electronics Systems (Ieee Comcas 2013),* p. 5, 2013.

[22]   W. B. Kuhn and N. M. Ibrahim, "Analysis of current crowding effects in multiturn spiral inductors," *Ieee Transactions on Microwave Theory and Techniques,* vol. 49, pp. 31-38, Jan 2001.

[23]   Q. Yu and T. W. Holmes, "A study on stray capacitance modeling of inductors by using the finite element method," *Ieee Transactions on Electromagnetic Compatibility,* vol. 43, pp. 88-93, Feb 2001.

[24]   Z. Yang, W. T. Liu*, et al.*, "Inductor modeling in wireless links for implantable electronics," *Ieee Transactions on Magnetics,* vol. 43, pp. 3851-3860, Oct 2007.

[25]   T. Riad, R. Mansour*, et al.*, *Behavior modelling for lc tank based oscillators*, 2004.

[26]   F. Ellinger. (2008). *Radio frequency integrated circuits and technologies (Second Edition. ed.)*.

[27]   A. Hajimiri and T. H. Lee, "Design issues in cmos differential lc oscillators," *Ieee Journal of Solid-State Circuits,* vol. 34, pp. 717-724, May 1999.

[28]   M. E. Heidari, A. A. Abidi*, et al.*, *Behavioral models of frequency pulling in oscillators*, 2007.

[29]   A. Mirzaei, M. E. Heidari*, et al.*, *Analysis of oscillators locked by large injection signals: Generalized adler's equation and geometrical interpretation*, 2006.

[30]   X. L. Lai, J. Roychowdhury*, et al.*, *Analytical equations for predicting injection locking in lc and ring oscillators*. New York: Ieee, 2005.

[31]   A. Mazzanti and P. Andreani, "Class-c harmonic cmos vcos, with a general result on phase noise," *Ieee Journal of Solid-State Circuits,* vol. 43, pp. 2716-2729, Dec 2008.

[32]   A. Mazzanti and P. Andreani, "A push-pull class-c cmos vco," *Ieee Journal of Solid-State Circuits,* vol. 48, pp. 724-732, Mar 2013.

[33]   M. Daliri and M. Maymandi-Nejad, "Analytical model for cmos cross-coupled lc-tank oscillator," *Iet Circuits Devices & Systems,* vol. 8, pp. 1-9, Jan 2014.

[34]   D. Harutyunyan, J. Rommes*, et al.*, "Simulation of mutually coupled oscillators using nonlinear phase macromodels," *Ieee Transactions on Computer-Aided Design of Integrated Circuits and Systems,* vol. 28, pp. 1456-1466, Oct 2009.

[35]   S. Sarma, V. K. Agrawal*, et al.*, "Software-based resolver-to-digital conversion using a dsp," *IEEE Transactions on Industrial Electronics,* vol. 55, pp. 371-379, 2008.

[36]   C. W. Secrest, J. S. Pointer*, et al.*, "Improving position sensor accuracy through spatial harmonic decoupling, and sensor scaling, offset, and orthogonality correction using self-commissioning mras methods," *Ieee Transactions on Industry Applications,* vol. 51, pp. 4492-4504, Nov-Dec 2015.

[37]   L. Hao, S. Gopalakrishnan*, et al.*, "Impact of position sensor accuracy on the performance of ipm drives," in *2013 ieee energy conversion congress and exposition*, ed New York: Ieee, 2013

[38]   R. Ramakrishnan, A. Gebregergis*, et al.*, *Effect of position sensor error on the performance of pmsm drives for low torque ripple applications*. New York: Ieee, 2013.

[39]   G. Liu, A. Kurnia*, et al.*, *Position sensor error analysis for eps motor drive*. New York: Ieee, 2003.

[40]   J. Lara, J. Xu*, et al.*, "Effects of rotor position error in the performance of field oriented controlled pmsm drives for electric vehicle traction applications," *IEEE Transactions on Industrial Electronics,* vol. PP, pp. 1-1, 2016.

[41]   H. Irle, N. Kost*, et al.*, "Inductive angle sensor," United States Patent, 2001.

[42]   D. S. Weile and E. Michielssen, "Genetic algorithm optimization applied to electromagnetics: A review," *Ieee Transactions on Antennas and Propagation,* vol. 45, pp. 343-353, Mar 1997.

[43]   W. L. Goffe, G. D. Ferrier*, et al.*, "Global optimization of statistical functions with simulated annealing," *Journal of Econometrics,* vol. 60, pp. 65-99, Jan-Feb 1994.

[44]   R. Chelouah and P. Siarry, "Tabu search applied to global optimization," *European Journal of Operational Research,* vol. 123, pp. 256-270, Jun 2000.

[45]   A. M. Zhou, B. Y. Qu*, et al.*, "Multiobjective evolutionary algorithms: A survey of the state of the art," *Swarm and Evolutionary Computation,* vol. 1, pp. 32-49, Mar 2011.

[46]   G. E. P. Box and K. B. Wilson, "On the experimental attainment of optimum conditions," *Journal of the Royal Statistical Society. Series B (Methodological),* vol. 13, pp. 1-45, 1951.

[47]   R. H. Myers and D. C. Montgomery, *Response surface methodology : Process and product optimization using designed experiments*, 2nd ed. New York: J. Wiley, 2002.

[48]   R. H. Myers, D. C. Montgomery*, et al.*, *Response surface methodology : Process and product optimization using designed experiments*, 3rd ed. Hoboken, N.J.: Wiley, 2009.

[49]   A. I. Khuri and S. Mukhopadhyay, "Response surface methodology," *Wiley Interdisciplinary Reviews: Computational Statistics,* vol. 2, pp. 128-149, 2010.

[50]   G. E. P. Box and D. W. Behnken, "Some new three level designs for the study of quantitative variables," *Technometrics,* vol. 2, pp. 455-475, 1960.

[51]   M. Schormans, V. Valente*, et al.*, "Frequency splitting analysis and compensation method for inductive wireless powering of implantable biosensors," *Sensors,* vol. 16, p. 14, Aug 2016.

[52]   H. Miyazaki, "Technical trends in steering systems," *Proceedings of the JFPS International Symposium on Fluid Power,* vol. 2008, pp. 133-136, 2008.

[53]   A. W. Burton, "Innovation drivers for electric power-assisted steering," *Control Systems, IEEE,* vol. 23, pp. 30-39, 2003.

[54]   K. J. Lee, K. H. Lee*, et al.*, "Design and development of a functional safety compliant electric power steering system," *Journal of Electrical Engineering & Technology,* vol. 10, pp. 1915-1920, Jul 2015.

[55]   V. Lemarquand, "Synthesis study of magnetic torque sensors," *Ieee Transactions on Magnetics,* vol. 35, pp. 4503-4510, Nov 1999.

[56]   D. Diddens, D. Reynaerts*, et al.*, "Design of a ring-shaped three-axis micro force/torque sensor," *Sensors and Actuators A: Physical,* vol. 46, pp. 225-232, 1// 1995.

[57] E. Zabler, A. Dukart, *et al.*, "Proceedings of eurosensors viia non-contact strain-gage torque sensor for automotive servo-driven steering systems," *Sensors and Actuators A: Physical,* vol. 41, pp. 39-46, 1994/04/01 1994.

[58] O. Dahle, "The ring torductor—a torque gauge without slip rings, for industrial measurement and control," *Asea Journal,* vol. 33, p. 23, 1960.

[59] W. J. Fleming, "Magnetostrictive torque sensors-comparison of branch, cross, and solenoidal designs," SAE Technical Paper 0148-7191, 1990.

[60] I. Sasada, F. Koga, *et al.*, "A new thin pickup coil for magnetic head type torque sensors," *Ieee Transactions on Magnetics,* vol. 29, pp. 3186-3188, Nov 1993.

[61] K. Ishikawa, K. Mohri, *et al.*, "Torque sensor using perpendicularly magnetizing coils," *Ieee Transactions on Magnetics,* vol. 27, pp. 4849-4851, Nov 1991.

[62] I. Sasada, A. Hiroike, *et al.*, "Torque transducers with stress-sensitive amorphous ribbons of chevron-pattern," *Magnetics, IEEE Transactions on,* vol. 20, pp. 951-953, 1984.

[63] K. Miyashita, T. Takahashi, *et al.*, "Features of a magnetic rotary encoder," *Ieee Transactions on Magnetics,* vol. 23, pp. 2182-2184, Sep 1987.

[64] R. J. Hazelden, "Optical torque sensor for automotive steering systems," *Sensors and Actuators a-Physical,* vol. 37-8, pp. 193-197, Jun-Aug 1993.

[65] R. C. Spooncer, R. Heger, *et al.*, "Non-contacting torque measurement by a modified moiré fringe method," *Sensors and Actuators A: Physical,* vol. 31, pp. 178-181, 1992.

[66] T. H. Wilmshurst, S. J. Rothberg, *et al.*, "Laser torquemeter - a new instrument," *Electronics Letters,* vol. 27, pp. 186-187, Jan 1991.

[67] "Laser torquemeter - immunity to memory quantization noise," *Electronics Letters,* vol. 27, pp. 2037-2038, Oct 1991.

[68] R. F. Wolffenbuttel and J. A. Foerster, "Noncontact capacitive torque sensor for use on a rotating axle," *Ieee Transactions on Instrumentation and Measurement,* vol. 39, pp. 1008-1013, Dec 1990.

[69] P. L. Fulmek, F. Wandling, *et al.*, "Capacitive sensor for relative angle measurement," *Instrumentation and Measurement, IEEE Transactions on,* vol. 51, pp. 1145-1149, 2003.

[70] E. Frohlich and F. Jerems, "Magnetic circuit of a contactless torque sensor for electric power steering," *Journal of Magnetism and Magnetic Materials,* vol. 320, pp. 2517-2520, Oct 2008.

[71]   C. Bechtold, I. Teliban, *et al.*, "Non-contact strain measurements based on inverse magnetostriction," *Sensors and Actuators A: Physical,* vol. 158, pp. 224-230, 2010.

[72]   D. Angleviel, D. Frachon, *et al.*, "Development of a contactless hall effect torque sensor for electric power steering," *2006 SAEWorld Congr,* 2006.

[73]   Q. A. Huang, L. Dong, *et al.*, "Lc passive wireless sensors toward a wireless sensing platform: Status, prospects, and challenges," *Journal of Microelectromechanical Systems,* vol. 25, pp. 822-841, Oct 2016.

[74]   R. Matsuzaki and A. Todoroki, "Wireless monitoring of automobile tires for intelligent tires," *Sensors,* vol. 8, pp. 8123-8138, Dec 2008.

[75]   K. Bao, D. Chen, *et al.*, "A readout circuit for wireless passive lc sensors and its application for gastrointestinal monitoring," *Measurement Science and Technology,* vol. 25, Aug 2014.

[76]   L. Qin, D. D. Shen, *et al.*, "A wireless passive lc resonant sensor based on ltcc under high-temperature/pressure environments," *Sensors,* vol. 15, pp. 16729-16739, Jul 2015.

[77]   A. Zanella, N. Bui, *et al.*, "Internet of things for smart cities," *Ieee Internet of Things Journal,* vol. 1, pp. 22-32, Feb 2014.

[78]   F. Cai, C. R. Yi, *et al.*, "Ultrasensitive, passive and wearable sensors for monitoring human muscle motion and physiological signals," *Biosensors & Bioelectronics,* vol. 77, pp. 907-913, Mar 2016.

[79]   A. Babu and B. George, "A linear and high sensitive interfacing scheme for wireless passive lc sensors," *Ieee Sensors Journal,* vol. 16, pp. 8608-8616, Dec 1 2016.

[80]   J. Coosemans, M. Catrysse, *et al.*, "A readout circuit for an intra-ocular pressure sensor," *Sensors and Actuators a-Physical,* vol. 110, pp. 432-438, Feb 1 2004.

[81]   R. Nopper, R. Niekrawietz, *et al.*, "Wireless readout of passive lc sensors," *Ieee Transactions on Instrumentation and Measurement,* vol. 59, pp. 2450-2457, Sep 10 2010.

[82]   H. Zhang, Y. Hong, *et al.*, "A novel readout system for wireless passive pressure sensors," *Photonic Sensors,* vol. 4, pp. 70-76, 2014.

[83]   H. S. Kim, S. Sivaramakrishnan, *et al.*, "A novel real-time capacitance estimation methodology for battery-less wireless sensor systems," *Ieee Sensors Journal,* vol. 10, pp. 1647-1657, Oct 2010.

[84]   R. Nopper, R. Has, *et al.*, "A wireless sensor readout system-circuit concept, simulation, and accuracy," *Ieee Transactions on Instrumentation and Measurement,* vol. 60, pp. 2976-2983, Aug 2011.

[85]   R. J. F. de Oliveira and P. J. Abatti, "Analysis of telemetric system based on remote resonant sensing circuit," *Electronics Letters,* vol. 42, pp. 750-752, Jun 2006.

[86]   C. Jun and D. Zhiquan, "Switched-reluctance position sensor," *Magnetics, IEEE Transactions on,* vol. 50, pp. 1-4, 2014.

Curriculum Vitae

Name:	Lingmin Shao
Post-secondary Education and Degrees:	Wuhan University of Technology Wuhan, Hubei, China 1989-1993 B.A.
	Tongji University Shanghai, China 1993-1995 M.A.
	Oakland University Rochester, MI 48309, USA 2004-2004 Ph.D.
	The University of Western Ontario London, Ontario, Canada 2010-2017 Ph.D.
Related Work Experience	Teaching Assistant Oakland University 2004-2004
	Product Engineer Shanghai Volkswagen 1996-2002
	Technical Specialist KSR International 2004-present

Publications:

[1]   N. Zhang, Z. Deng, L. Shao, and J. Yang, "Analytical solution for capacitance and characteristic impedance of cpw with defected structures in signal line," *Progress In Electromagnetics Research Letters,* vol. 54, pp. 79-84, 2015.

[2]   N. B. Zhang, M. J. Hu, L. Shao, and J. Yang, "Localization of printed chipless rfid in 3-d space," *Ieee Microwave and Wireless Components Letters,* Article vol. 26, no. 5, pp. 373-375, May 2016.

[3]   L. Shao and J. Hartford, "Linear sensor," United States Patent US2015/0129389 A1, 2015.

[4]   L. Shao and R. W. Elliott, "Steering position and torque sensor," United States Patent 8988066, March 24, 2015.

[5]   J. K. Lee, L. Shao, and R. W. Elliott, "Rotary position sensor," United States Patent 8947077, February 3, 2015.

[6]   R. W. Elliott, D. O'neill, L. Shao, S. M. Fuller, and J. Hartford, "Integrated brake control sensor," United States Patent 20150070003, 2015.

[7]   R. W. Elliott and L. Shao, "Micro inductive sensor," United States Patent 20140327432, 2014.

[8]   R. W. Elliott and L. Shao, "Micro inductive sensor," Patent WO/2014/179803, 2014.

[9]   L. Shao, J. K. Lee, and R. W. Elliott, "Inductive position sensor," Patent 8508242, August 13, 2013.

[10]   L. Shao and R. Elliott, "Steering position and torque sensor," United States Patent 20120223700, 2012.

[11]   L. Shao and R. W. Elliott, "Steering position and torque sensor," Patent WO/2012/117293, 2012.

[12]   J. K. Lee, L. Shao, and R. W. Elliott, "Rotary position sensor," United States Patent 20120293166, 2012.

[13]   J. K. Lee, L. Shao, and R. W. Elliott, "Rotary position sensor," Patent WO/2012/156815, 2012.

[14]   R. W. Elliott, J. K. Lee, and L. Shao, "Linear inductive position sensor," United States Patent 8098061, January 17, 2012.

[15]   L. Shao, J. K. Lee, and R. W. Elliott, "Inductive position sensor," Patent WO/2011/089519, 2011.

[16]   R. W. Elliott, J. K. Lee, and L. Shao, "Linear inductive position sensor," United States Patent 20090256555, 2009.